Vol. 9 No. 1
April 2025

ISSN 2579-5821
e-ISSN 2579-5546

S3
sinta
Science and Technology Index

Jurnal Geocelebes

Published by:
Geophysics Department
Hasanuddin University
Makassar, Indonesia

JURNAL GEOCELEBES
Geophysics Department | Faculty of Mathematics and Natural Sciences | Hasanuddin University

Volume 9 Number 1, April 2025

P-ISSN: 2579-5821
E-ISSN: 2579-5546

Published by:
Geophysics Department, Math and Natural Science Faculty
Hasanuddin University

JURNAL GEOCELEBES
Volume 9 Number 1, April 2025

ISSN: 2579 – 5821 (Print)
ISSN: 2579 – 5546 (Online)
URL address: http://journal.unhas.ac.id/index.php/geocelebes

Diterbitkan berkala dua kali setahun oleh/ **Published periodically two times annually by**
Dept. Geofisika Universitas Hasanuddin/ **Geophysics Dept., Hasanuddin University**

Dewan Redaksi/ Editor Board

Sekretariat/ Secretariat:
Departemen Geofisika, FMIPA Universitas Hasanuddin
Gedung MIPA, Kampus Unhas Tamalanrea - Jalan Perintis Kemerdekaan, Makassar, Sulawesi Selatan, 90245.
E-mail: geocelebes@sci.unhas.ac.id

Jurnal Geocelebes is a scientific journal published by the Department of Geophysics, Hasanuddin University. This journal is intended as a means of scientific publication in the field of geophysics ranging from theoretical topics to geophysical applications in various fields topics. The articles are original research results, reviews of recent advances in a particular topic, case studies of geophysical applications or reviews of software related to geophysics. Papers should be sent to the editorial website in softcopy using the template provided. Each accepted paper will be reviewed for eligibility through a rigorous reviewing process by the Editorial Board.

Contents

JURNAL GEOCELEBES

Volume 9, Number 1, April 2025

ISSN: 2579 – 5821 (Print)
ISSN: 2579 – 5546 (Online)

URL: http://journal.unhas.ac.id/index.php/geocelebes

Cover ---------- i
Editorial boards ---------- iii
Contents ---------- iv
Preface ---------- vi

Mapping of Soil Stability based on Shear Wave Velocity Values (Vs30) Using the Multichannel Analysis Surface Wave (MASW) Method on Kalimantan Highway, Rawa Makmur Village, Bengkulu City ---------- 1
Aisyah Cindy Phylia Putri, Refrizon Refrizon, Arif Ismul Hadi, Andre Rahmat Al Ansory

Analysis of Landslide Hazard Levels on the Palopo – Luwu Road using GIS and Finite Element Method ---------- 15
Anshar Abdullah Jawil, Kadek Nando Setiawan

Microbiological Study of Escherichia Coli Contamination in Dug Wells in Demak District, Central Java ---------- 28
Narulita Santi, Celsy Miftaqul Tiara Fanny, Dina Rahayuning Pangestuti, Thomas Triadi Putranto, Maya Aiko Salsabila Putri

Predicting the Distribution of CO2 Impurities in Hydrocarbons: Seismic Reservoir Characterization in the Northern South Sumatera Basin ---------- 43
Ricky Rahmawati, Wahidah Wahidah, M Noor Alamsyah, Dadan Hamdani, Andi Alamsyah

Impact of El Niño - Southern Oscillation (ENSO) and Indian Ocean Dipole (IOD) on Air Temperature in Bengkulu City ---------- 59
Mardho Tillah Edkayasa, Elfi Yuliza, Lizalidiawati Lizalidiawati

Application of 2D Seismic Modeling in Gas Hydrate Reservoir Characterization ---------- 78
Welayaturromadhona Welayaturromadhona, How-Wei Chen

Source Rock Evaluation in the "Idea" Field, Bintuni Basin, West Papua: A Geochemical Approach ---------- 87
Dea Ananda, Jamaluddin Jamaluddin, Warto Utomo, Joko Wiyono, Baiq Maulinda Ulfah, Amiruddin Amiruddin, Nijusiho Manik, Abdi Suprayitno

Preface

Jurnal Geocelebes managed by the Department of Geophysics, Faculty of Mathematics and Natural Sciences, Hasanuddin University Makassar has entered its ninth year. The Editorial Board expresses gratitude to God Almighty for this achievement and expresses gratitude for the commitment of the Editorial Board, in carrying out this mandate. In particular, the Editorial Board expresses its gratitude and highest appreciation to all authors who have submitted their scientific works and to the Reviewers who have been willing to take the time to provide constructive suggestions and corrections to each article in each issue of the Jurnal Geocelebes.

In the edition of Volume 9 Number 1 April 2025 there are seven articles. The articles published generally discuss the implementation of the role of geosciences, especially geophysics in natural resource exploration and other fields that are in accordance with the focus and scope of the field published by the Jurnal Geocelebes. The language used in this volume is English, which shows that Jurnal Geocelebes deserves to be an international journal in the future. In this month, The Editorial Board have submitted the application of Re-accreditation of SINTA. Jurnal Geocelebes welcomes participation from academics, researchers, industry practitioners, students, and others in the field of geosciences in both theoretical and application perspectives, both related to the subsurface (lithosphere) and above the surface (atmosphere), which of course will go through a series of processes namely submitting, editing, and reviewing.

The Editorial Board of Jurnal Geocelebes is open to suggestions and constructive criticism for future improvements. All suggestions and criticisms can be sent via email geocelebes@sci.unhas.ac.id

Makassar, April 2025

The Editorial Board of Jurnal Geocelebes

ISSN: 2579-5821 (Print)
ISSN: 2579-5546 (Online)
URL address: http://journal.unhas.ac.id/index.php/geocelebes
DOI: 10.70561/geocelebes.v9i1.34956

Jurnal Geocelebes Vol. 9 No. 1, April 2025, 1 – 14

Mapping of Soil Stability based on Shear Wave Velocity Values (Vs30) Using the Multichannel Analysis Surface Wave (MASW) Method on Kalimantan Highway, Rawa Makmur Village, Bengkulu City

Aisyah Cindy Phylia Putri[1], Refrizon[1]*, Arif Ismul Hadi[1]*, Andre Rahmat Al Ansory[2]

[1]Geophysics Study Program, University of Bengkulu, Jl. WR Supratman, Bengkulu, 38371, Indonesia.
[2] Mitigation and Exploration Laboratory, Floor 2, Integrated laboratory, University of Bengkulu, Jl. WR Supratman, Bengkulu, 38371, Indonesia

*Corresponding author. Email: refrizon@unib.ac.id, ismulhadi@unib.ac.id

Manuscript received: 16 May 2024; Received in revised form: 22 July 2024; Accepted: 2 August 2024

Abstract

Kalimantan Highway in Bengkulu is a heavily traveled route and the main gateway to Bengkulu City from northern areas such as Arga Makmur and Ketahun sub-district, or Mukomuko regency also surrounding areas. Geological formations in the form of alluvium terraces (Qat) cause soil instability, often damaging the road surface. These include the formation of potholes and the occurrence of puddles during heavy rains. This research aims to determine the bearing capacity (stability) of the soil layer along Kalimantan Highway section in Rawa Makmur Village, Muara Bangkahulu District, and provide planning information through mapping. It is imperative to assess the condition of the soil layer. This research uses geophysical methods, specifically the Multichannel Analysis of Surface Wave (MASW) technique, using a MASW PASI 16S24-P digital seismograph to image subsurface soil conditions by analyzing shear wave velocity (Vs). A total of 20 data points were collected along the Kalimantan Highway section. The results of the Vs profile analysis were interpreted into soil classifications based on the criteria set out in SNI 1726:2019. The majority of the road sections were classified as SE (soft soil) and SD (medium soil), with some points designated as SC (hard soil/soft rock). This indicates that the geotechnical design for these road sections should consider supporting factors to maintain structural safety and stability.

Keywords: Bengkulu; Multichannel Analysis Surface Wave; Shear Wave Velocity; Subsoil.

Citation: Putri, A. C. P., Refrizon, R., Hadi, A. I., & Al Ansory, A. R. (2025). Mapping of Soil Stability based on Shear Wave Velocity Values (Vs30) Using the Multichannel Analysis Surface Wave (MASW) Method on Kalimantan Highway, Rawa Makmur Village, Bengkulu City. *Jurnal Geocelebes*, 9(1): 1–14, doi: 10.70561/geocelebes.v9i1.34956

Introduction

Kalimantan Highway in Bengkulu City is a road that is classified as a congested road. The road is very important because it serves as the main infrastructure to enter Bengkulu City from northern areas such as Arga Makmur or Ketahun sub-districts and Mukomuko regency and surrounding areas. Since 2016 the government has planned to increase the capacity of this road (Kementerian Pekerjaan Umum dan Perumahan Rakyat, 2016). This road section is highly supportive of vehicular transport as it facilitates trade, economic growth and access to a range of services (Suparno et al., 2023).

The highway extends for 3.9 kilometers and is between 6 to 8 meters wide. It connects Kalimantan Highway with Sungai Hitam Highway, which is situated in close proximity to numerous commercial establishments and residential neighborhoods. The geological formation

of the alluvium terrace (Qat), which consists of gravel, sand, and clay-silt (Sugianto et al., 2017), also contributes to the instability of the soil due to its expansive nature, high shrinkage-expansion value, and high sensitivity to water. Clay soil can be identified as a potential cause of road construction instability (Vikki et al., 2022) as shown in Figure 1 by the blue areas. In addition, these roads are often flooded, with high water levels covering the road surface causing community mobility to be disrupted (Budianto et al., 2023).

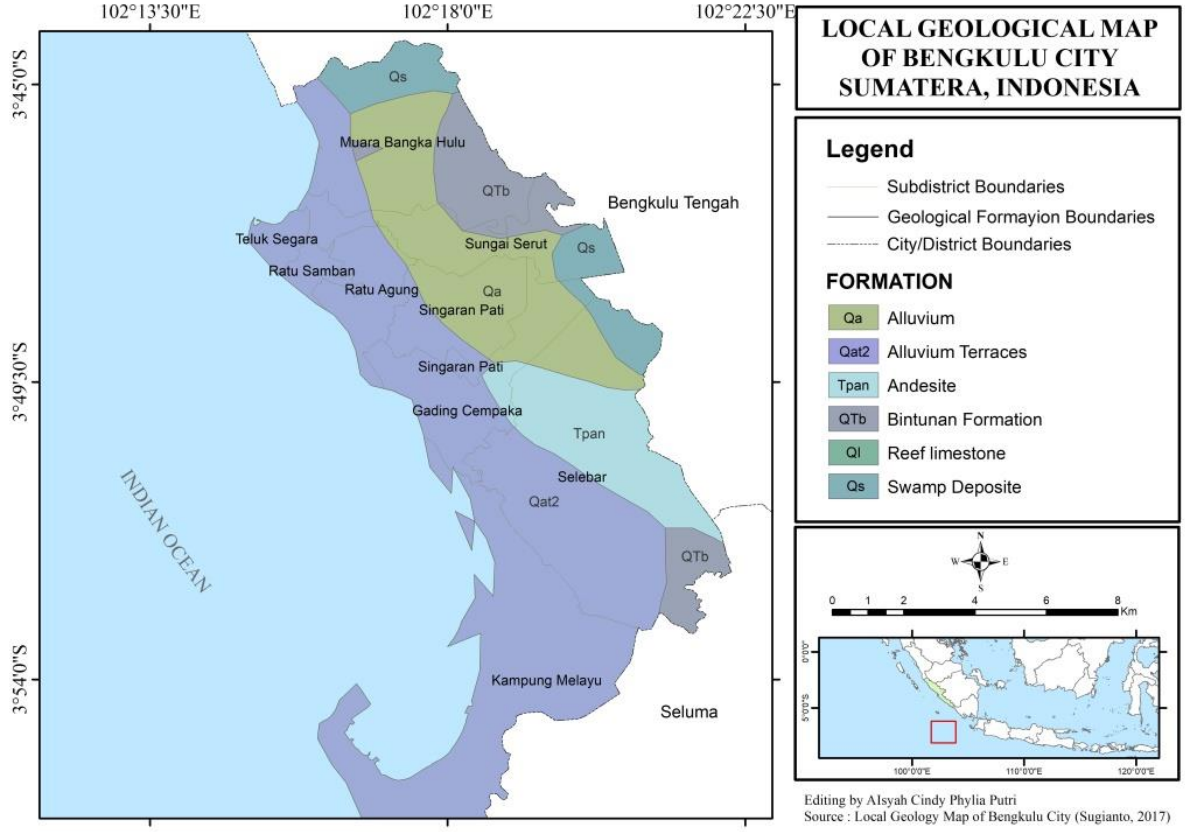

Figure 1. Local Geological Map of Bengkulu City (Modified from Sugianto et al. (2017)).

The terrace alluvium formation (Qat) is a layer of soil composed of sand, silt, clay and gravel collected from deposits in rivers, beaches and swamps. This geological unit does not reach the eastern part of Bengkulu, but is spread throughout the city from north to south (Nofirman, 2016). The soils tend to be different and may not be consistent. The term "alluvium terrace" or Qat refers to the process of deposition of alluvial deposits by river or water flow and is often found around or along roadways (Oldknow & Hooke, 2017). The changing ground movements make building on alluvium terrace (Qat) formations not recommended because alluvium terrace (Qat) formations have several risks that can threaten the stability of homes and infrastructure, these risks include flooding, earthquakes, liquefaction, and disaster. Infrastructure designed with adequate bearing capacity, or "sustain," is important in sustainable development. This approach allows for considering local geological conditions, enhancing buildings' resilience against potential damage (Al Ansory et al., 2024).

Therefore, to identify stable soil layers, it is necessary to measure the condition of the subsoil. The acquisition was carried out with the Multichannel Analysis Surface Wave (MASW) geophysical method, the

result of MASW data interpretation is the Vs30 value (Shear wave velocity in 30m depth) which produces a profile of subsurface conditions and is considered a good indicator by Park et al. (1999) so it can be used to determine the classification of rocks based on the strength of earthquake vibrations. The Vs30 value can be used to determine earthquake-resistant building standards and estimate an area vulnerable to earthquakes (Prasisila et al., 2021).

The MASW method can record Rayleigh wave propagation to investigate the mechanical properties of subsurface layers and the level of rock density. It is effectively used because it can save costs and time. The steps of applying the MASW method start from data collection, surface wave analysis, velocity modeling, inversion, and finally, interpretation and modelling (Hasya et al., 2021). The MASW method is a non-invasive geophysical technique because it provides detailed information about soil structure without the need for direct drilling or excavation (Susilanto et al., 2019), which is used to collect data about the condition of subsurface soil structure. This technique works by analyzing Rayleigh waves triggered by a vibration source at the ground surface. These waves travel through the soil layers, and their propagation velocity is measured to identify soil properties. One of the critical aspects of an MASW survey is the arrangement of geophones. These geophones are placed in a straight line at specific intervals to detect and record ground vibrations to gather data. Each geophone is responsible for recording vibration signals originating from the sources like hammers or heavy machinery, which cause the propagation of Rayleigh waves through the ground (Mufardis et al., 2023). For quality control of MASW data acquisition results, it is important to check the quality of the Rayleigh wave signal recorded by each geophone. The signal must be clear and free from high noise in order for the main signal to be well-defined, allowing accurate dispersion analysis. In addition to clarity, the signal should also have sufficient amplitude for preliminary spectral analysis. This analysis is conducted by examining the frequency and amplitude of the signal, which is expected to be sufficient to distinguish between different soil layers (Lin et al., 2004).

Research on sediment layer analysis using shear wave velocity has been conducted by Lubis et al. (2021), using the MASW analysis method in the Liwa area. The results showed that the first layer structure has a shear wave velocity (Vs) value of around 250 – 300 m/s, a density of 1.7 – 2.2 gr/cm^3, and is 15 – 20 m thick. The second layer has a Vs value of 600 – 800 m/s with an average thickness of 5m. The third layer has Vs between 800 – 1000 m/s and is 25 – 50 m thick. Based on this research, it can be concluded that the MASW method is effective for mapping and understanding the condition of the soil sediment layer located on Kalimantan Highway to Sungai Hitam Highway in Muara Bangkahulu. By using seismic waves, this study aims to identify the 1D layer profile characteristics, which is Vs, of the soil layer. Vs is a crucial parameter in modelling soil dynamics, especially in the context of cyclic or repetitive loads (Rosyidi, 2015). Seismic methods can be used to measure the Vs of materials to obtain information about the subsurface structure of the soil. In this study, the MASW method is applied to measure the seismic wave velocity and describe the condition of the soil sediment layer in the road section of Muara Bangkahulu area.

Materials and Methods

Regional Geology and Research Area

In general, soils in Bengkulu City consist of alluvium terrace sediments (Qat), especially in the coastal areas and the central part of the city, consisting of various types of sediments, such as sand, silt, clay, and gravel, according to the geological map

of Bengkulu City. When earthquakes occur in the Bengkulu-Mentawai region, liquefaction is often found in places dominated by alluvium (Qa) and alluvium terrace (Qat) (Mase et al., 2021), especially along the coast as shown in Figure 1. Whereas around the measurement location, the geological formation is an Alluvium terrace (Qat), which is formed in a cycle of river terrace formation, which means that the soil type is related to the terrace field and is formed through the process of river erosion, deposition, or a mixture of both. Each alluvium terrace has diverse geomorphological characteristics compared to other soil types (El Oshebi et al., 2020). Alluvium terraces are plains or landforms formed by sediment deposition by rivers or streams. They are often found along river courses and form when river flow slows down, resulting in the gradual deposition of sediment. The size and elevation of alluvium terrace vary widely (Butzer et al., 1973).

A study by Hadi et al. (2021), indicates that the Alluvium Rock Formation Unit (Qa) in Bengkulu City has a Holocene age and is included in Quaternary Sediments. Furthermore, the Alluvium Terrace (Qat), Reef Limestone (Ql), and Swamp Deposits (Qs) are also Holocene-aged Quaternary Sediments (Table 1). It is important to note that these areas are susceptible to more significant rock deformation during an earthquake due to the hardness of the less compact rocks. However, the foundation must reach hard rock or bedrock to construct facilities and infrastructure in this area.

In the research, primary data of 20 points along Kalimantan Highway to Sungai Hitam Highway were acquired by MASW tool and secondary data from USGS of 8 points. Primary data is data obtained directly from research subjects or is original data that has never been processed before. This data is not available in file format because primary data collection usually involves the use of appropriate research tools or instruments to collect information directly from the source (Suhono & Al Fatta, 2021).

The observations were made by observing the structures visible on the soil surface of the road section with the assumption that it may be a factor in surface rupture of the road at Kalimantan Highway, Kelurahan Rawa Makmur, Bengkulu City, Bengkulu Province. The location of the research measurement point is shown in Figure 2.

Multichannel Analysis of Surface Wave (MASW)

The Multi-channel Analysis of Surface Wave (MASW) method is a geophysical technique that gathers data from the earth's surface through the analysis of Rayleigh waves, which are a type of surface seismic wave that travels along the top of the ground. The MASW method uses the dispersion characteristics of ground roll, a phenomenon where different seismic wave frequencies travel at different velocities, to measure the shear wave velocity (Vs) of subsurface material (Dewi et al., 2020).

Table 1. Rock Formations in Bengkulu City (Modified from Hadi et al. (2021))

Geological Formations	Litology	Collapse	Age
Andesite (Tpan)	The following geological formations were identified:	Tertiary	Late Miocene
Reef Limestone (Ql)	Sand and gravel	Quaternary	Holocene
Bintunan Formation (Qtb)	Reef limestone	Tertiary	Pliocene-Pleistocene
Alluvium (Qa)	Conglomerate, breccia, and tuffaceous limestone	Quaternary	Holocene
Alluvium Terrace (Qat)	Boulders, chert, sand, silt, and clay	Quaternary	Holocene
Alluvium (Qa) - Swamp Deposits (Qs)	Gravel, sand, and clay-silt	Quaternary	Holocene

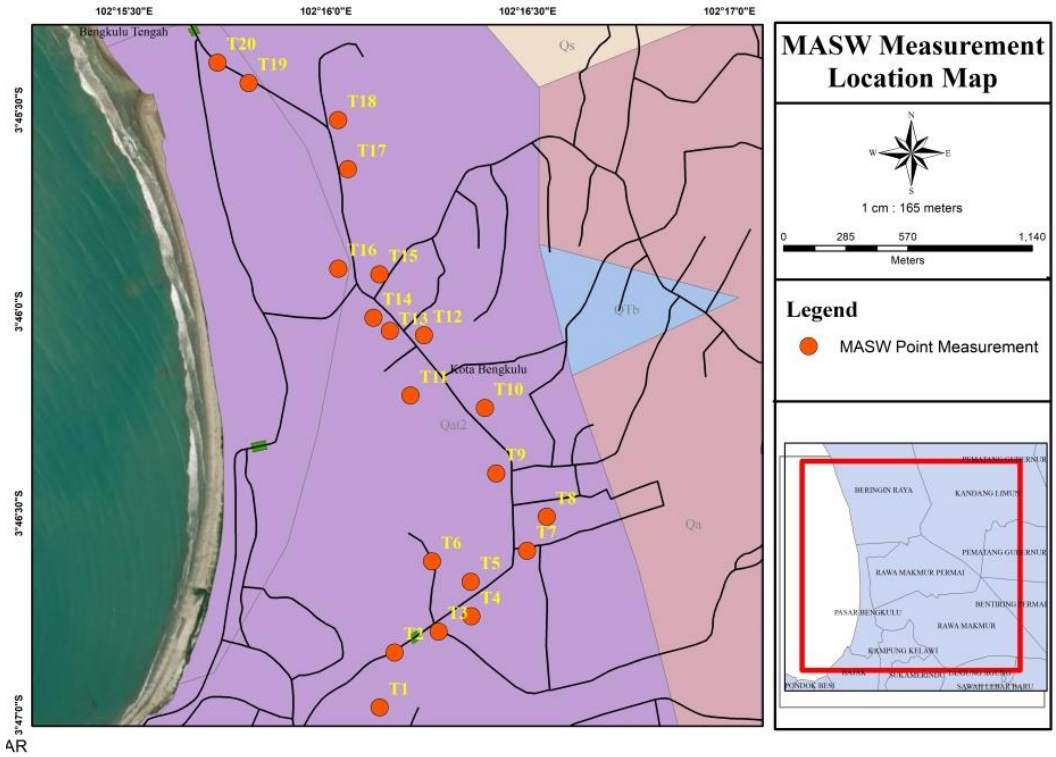

Figure 2. Map of the point measurement of Multichannel Analysis Surface Wave in the research location.

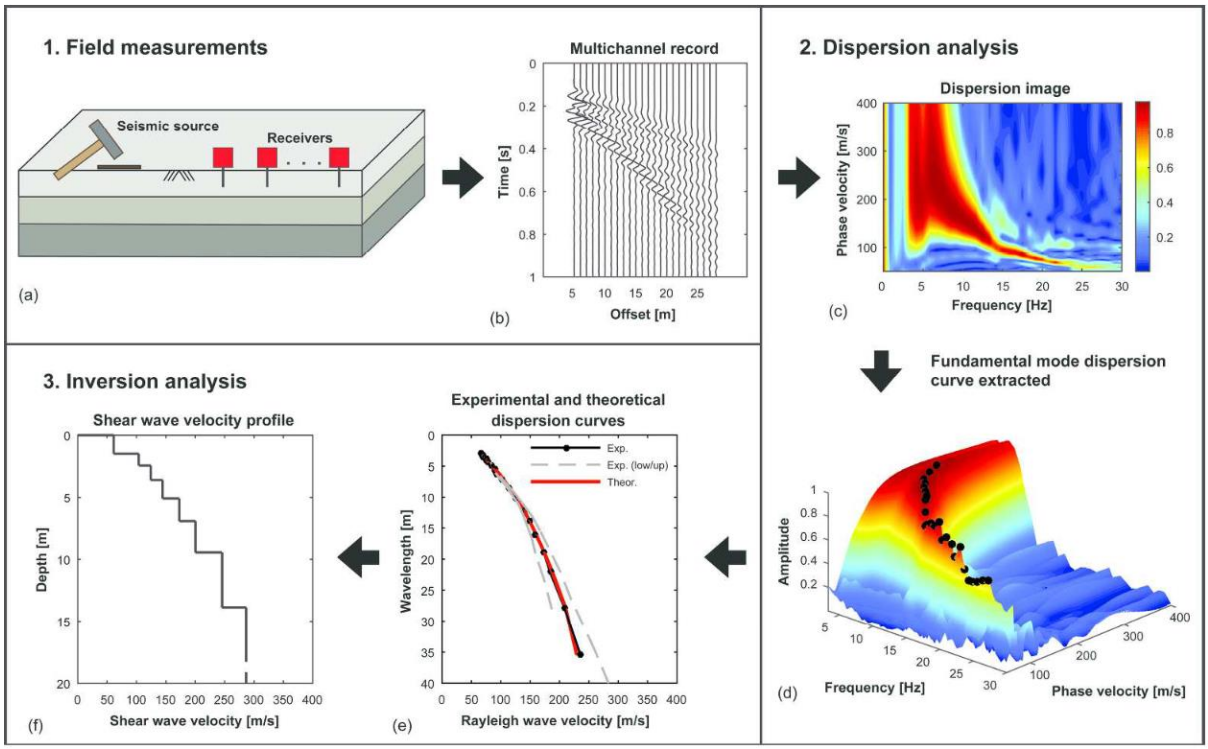

Figure 3. Overview of the MASW method: (*a*, *b*) field measurements; (*c*, *d*) dispersion analysis; (*e*, *f*) inversion analysis (Ólafsdóttir et al., 2017)**.**

A non-invasive geophysical technique known as Multichannel Analysis of Surface Wave (MASW) is often used to identify and quantify subsurface soil structure. MASW is based on the Rayleigh wave propagation theory, where it is formed through the interaction between shear waves and the surface soil layer. In addition, MASW can identify the Vs as a function of depth. From this velocity data,

information about the soil layers, such as thickness, hardness, and density, can be extracted. MASW is often used in construction planning and geological research (Muzli et al., 2016). It aids in geological research by mapping subsurface conditions and identifying geological formations, which are essential for infrastructure development and environmental assessments. It also evaluates the appropriateness of the ground for building structures in construction planning.

The principle in this method consists of three main steps (Figure 3), i.e., acquisition of seismic data, performing dispersion analysis, and finally converting the dispersion curve (Ólafsdóttir et al., 2017). The data acquisition tool was a MASW PSI 16S24-P digital seismograph. MASW seismic data collection begins with the installation of the tool at the study site. A total of 24 geophones were installed with a distance of 3 meters between geophones in each track, with the first and last far offset distance being 3 metres. A PASI seismograph was installed between the 12th and 13th geophones. The geophone cable was installed and connected between the cable connector and the geophone. Once the installation was complete, the PASI Seismograph was switched on and a new file was created by selecting the acquisition option and adding notes according to the names at the study site and setting the recording time. Triggers were placed near the metal plate and blows from the hammer as a seismic source were channelled to the metal plate. The recorded waves can be viewed by loading them from the PASI Seismograph. The final stage was to copy the data recorded by the Seismograph to a USB Drive and then save it in .DAT format for analysis. Next, the software operated to process seismic data for the MASW method, which is WinMASW, starting from picking data to producing an inversion of the surface wave dispersion curve obtained by processing results from MASW raw data.

Shear Wave Velocity (Vs)

Shear wave velocity (Vs), or secondary or S-wave velocity, is crucial for assessing soil and rock elasticity properties in geophysics. It measures the speed at which shear waves travel through the subsurface material. Unlike primary (P) waves, which compress and expand the material they move through, shear waves displace the material perpendicularly to their direction of travel, making Vs a direct indicator of the material's rigidity and shear strength. Vs is essential for evaluating the dynamic conditions of soil in shallow subsurface layers, particularly in geotechnical and earthquake engineering. Typically, Vs is higher in solid rocks than primary wave velocity due to the higher rigidity of rocks. However, Vs can vary significantly depending on the type of rock and the geological conditions. For instance, in areas with thick sedimentary deposits, Vs can be lower due to these materials' softer, less rigid nature, which can influence seismic wave behavior during earthquakes (Susilanto & Ngadmanto, 2015). The following is a formula for calculating the average velocity of shear waves at a depth of no more than 30 meters:

$$Vs30 = \frac{30}{\sum_{i=1}^{N} \frac{h_i}{v_i}} \quad (1)$$

where $Vs30$ is the average velocity of the layer reaching a depth of 30 m, hi is the layer thickness of 0 to 30 m and Vi is the shear wave velocity of the nth layer, these calculations help classify soil types and assess their seismic response, which is crucial for construction and infrastructure development in disaster-prone areas (Lantu et al., 2018).

Classification of Soils Based on Vs30

Soil classification is the classification of soils based on their physical, chemical and morphological characteristics. Usually, the

soil classification process considers aspects such as texture, structure, organic material content, color, and mineral composition. According to Indonesian National Standard (SNI) 1726:2019, there is a soil classification based on the Vs30 value as follows in Table 2 (Zawawi et al., 2023).

Table 2. Site classification based on SNI 1726:2019 by (Zawawi et al., 2023).

Classification Class	Vs30
SA (Hard Rock)	>1500
SB (Rocks)	>750-1500
SC (Hard, very compact soil and soft rock)	>350-750
SD (Medium soil)	175-350
SE (Soft soil)	<175
SF (Special soil)	Specific investigation

Soils requiring site-specific investigation include (Building Seismic Safety Council - BSSC, 2003):

1. Soils prone to potential failure or collapse under seismic conditions, such as soils susceptible to liquefaction, quick clays, and highly sensitive clays, as well as collapsible weakly cemented soils.
2. Peat and/or highly organic clays where the thickness (H) exceeds 10 feet (3 meters).
3. Very high plasticity clays where the thickness (H) exceeds 25 feet (8 meters) and the plasticity index (PI) exceeds 75.
4. Very thick layers of soft or medium stiff clays where the thickness (H) exceeds 120 feet (36 meters) and the undrained shear strength (su) is less than 1,000 pounds per square foot (50 kilopascals).

Classification of soils based on Vs30 values involves grouping soils based on the velocity of earthquake wave propagation in them at a depth of 30 meters. Vs30 is a parameter used to assess the potential for earthquake wave amplification as well as the vulnerability of structures to earthquakes. Soils with low Vs30 values tend to have lower stiffness and may experience earthquake wave amplification, while soils with high Vs30 values are typically denser and have a lower risk of damage from earthquakes.

Result and Discussion

The shear wave velocity (Vs) profile in the MASW method is a graphical representation of seismic wave velocity as a function of depth below the ground surface. To determine the seismic wave velocity at various depths below the ground surface, data obtained from seismic waves propagating in the MASW are analysed. The results of this analysis are then depicted in Vs profiles, which show how the seismic wave velocity changes with the depth of the subsoil, which can provide information about the structure of the subsoil.

The measurement results obtained from processing the Vs profile at points T4, T5, T6, T7, T11, T12, T13, T14, T19 and T20 are shown in Figure 4. The interpretation results refer to the soil classification based on the Vs30 value of SNI 1726:2019, which are 152, 152, 172, 142, 170, 121, 155, 168, 157 and 154 m/s is SE or soft soil.

The measurement results obtained from processing the Vs profile at points T1, T3, T9, T10, T16, T17 and T18 are shown in Figure 5. The interpretation results refer to the soil classification based on the Vs30 value of SNI 1726:2019, which are 229, 252, 242, 183, 296, 254 and 328 m/s, which are SD or medium soil.

The measurement results obtained from processing the Vs profile at points T2, T8 and T15 are shown in Figure 6. The interpretation results refer to the soil classification based on the Vs30 value of SNI 1726:2019, which are 438, 479 and 574 m/s is SC or hard soil/ soft rock.

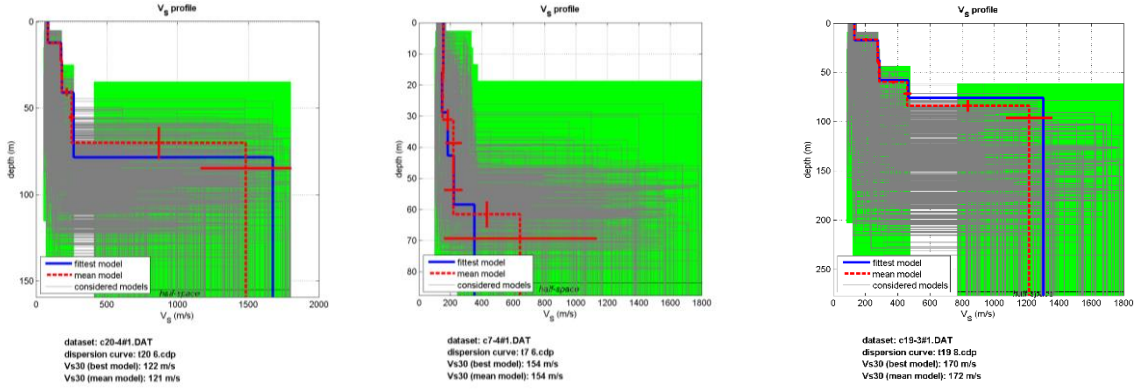

(a) (b) (c)

Figure 4. WinMASW Software Vs Profile (a) lowest Vs30 value in SE class. (b) average Vs30 value in SE class. (c) highest Vs30 value in SE class.

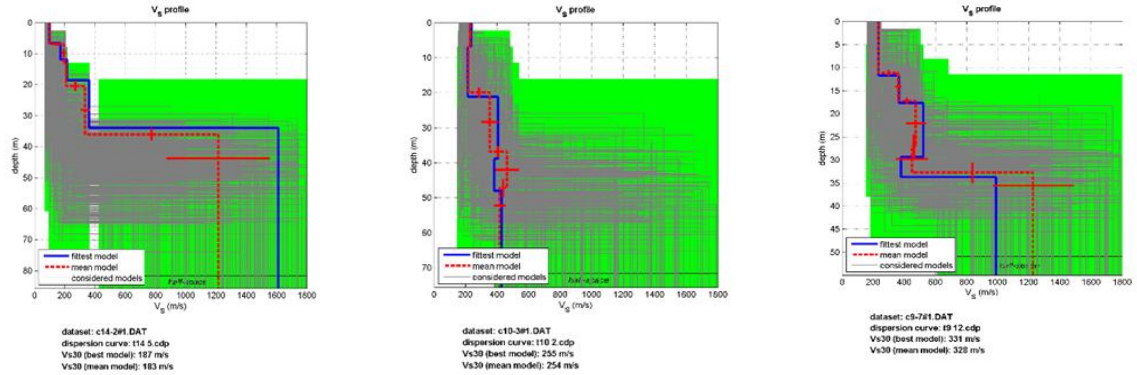

(a) (b) (c)

Figure 5. WinMASW Software Vs Profile (a) lowest Vs30 value in SD class. (b) average Vs30 value in SD class. (c) highest Vs30 value in SD class.

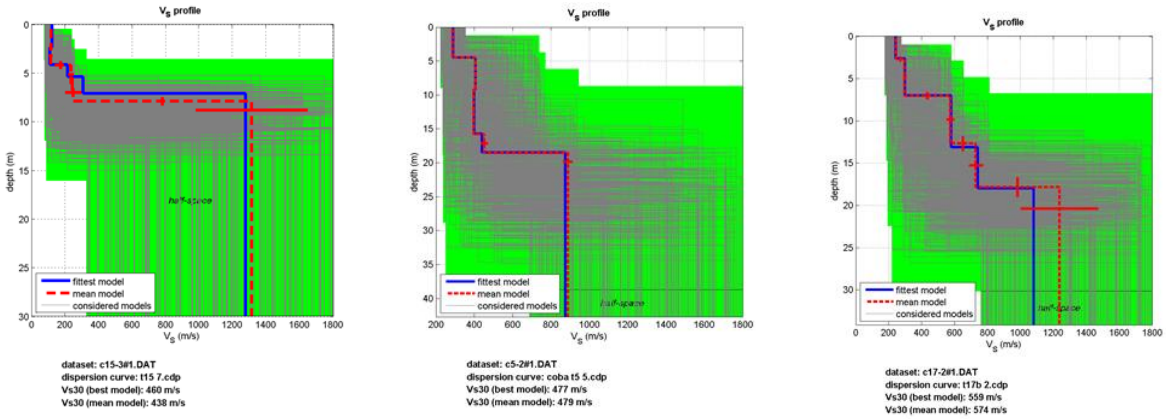

(a) (b) (c)

Figure 6. WinMASW Software Vs Profile (a) lowest Vs30 value in SC class. (b) average Vs30 value in SC class. (c) highest Vs30 value in SC class.

Analysis of measurement data using MASW at Rawa Makmur road revealed a variation in Vs30 values between 121 and 574 m/s. The characteristics of these values are reflected in the site class map (Figure 7) created by the interpolation method, where most areas are marked in dark purple or SD, according to the SNI 1726:2019

classification, with a value range of 175 – 350 m/s representing medium stiffness soils. This area shows adequate soil strength as it is between soft and hard soil but tends to be soft due to the geological formation which is alluvium terrace (Qat).

In general, the soil site classification based on the Vs30 value at Kalimantan Highway is divided into three types of site classifications, which are soft soil (SE), medium soil (SD), and hard soil, very dense, and soft rock (SC). Where the distribution is seen on the map in Figure 7, which shows that soft soil (SE) is represented in light purple, then medium soil (SD) is represented in dark purple, while hard soil, very dense and soft rock, is represented in blue. Areas with this soft soil classification are located almost along the highway in the Terrace Alluvium Formation (Qat). This formation is younger than the other soil types and needs to experience more pressure and time to compact and harden like the older soils, so the rocks are tenuous, which causes the Vs to be small that affects how fast the S-wave propagates; the denser the soil, the faster the S-wave propagates. This means that although they are both on alluvium soils, their soil density and compactness different (Ardianto, 2018).

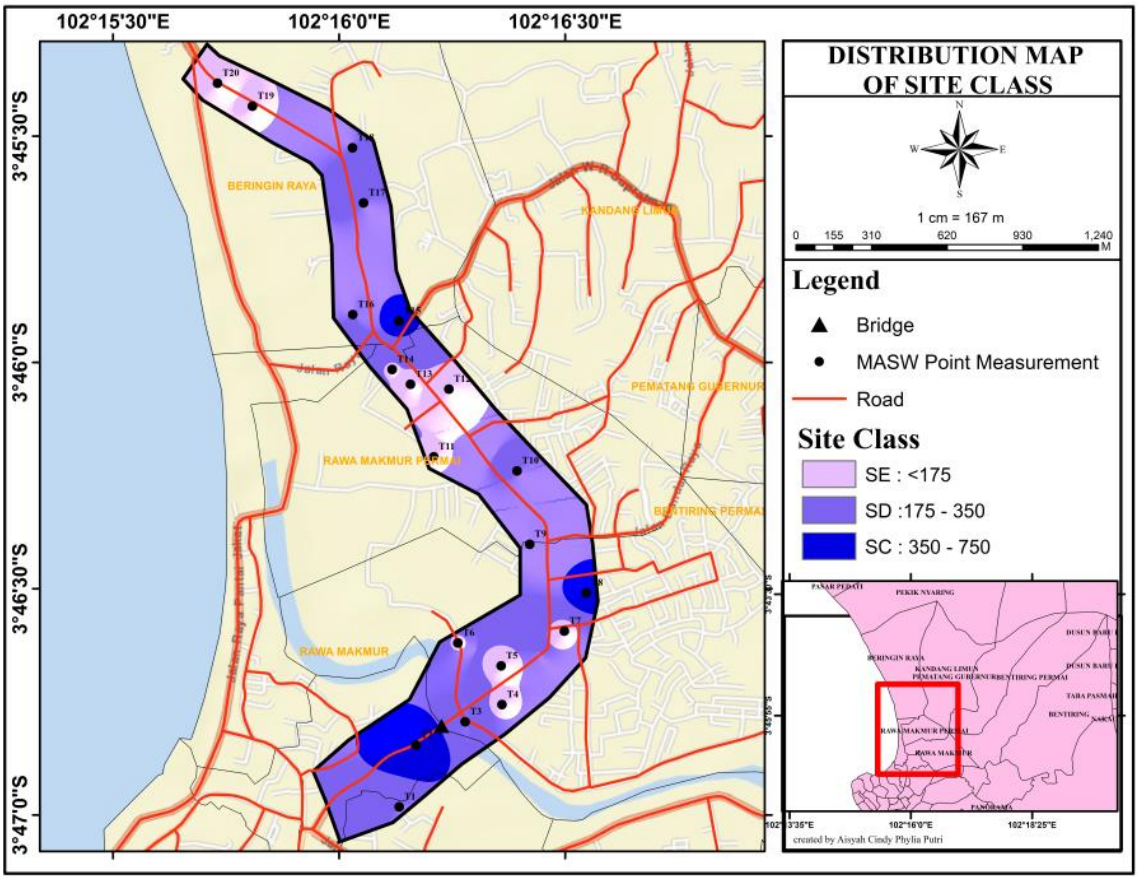

Figure 7. Map of site class.

In Figure 8, areas interpreted as showing moderate to high stiffness, shown in red-brown with Vs30 values ranging from 435 to 574 m/s, fall into the SC class, indicating hard, very dense soil and soft rock, with potential for deformation. However, higher soil density and consistency only occur at some points, such as at points 2, 8, and 15. Soils with Vs30 values greater than 350 m/s can be considered adequate foundations for infrastructure such as highways as they exhibit sufficient stability to withstand forces or shocks. According to research (Bustari & Wibowo, 2023), soils with Vs30 values between 240 and 410 m/s fall into the low to medium-risk category. However,

if infrastructure is built in areas with Vs30 values of at least 350 m/s, the soil's stability will be sufficient to support road construction.

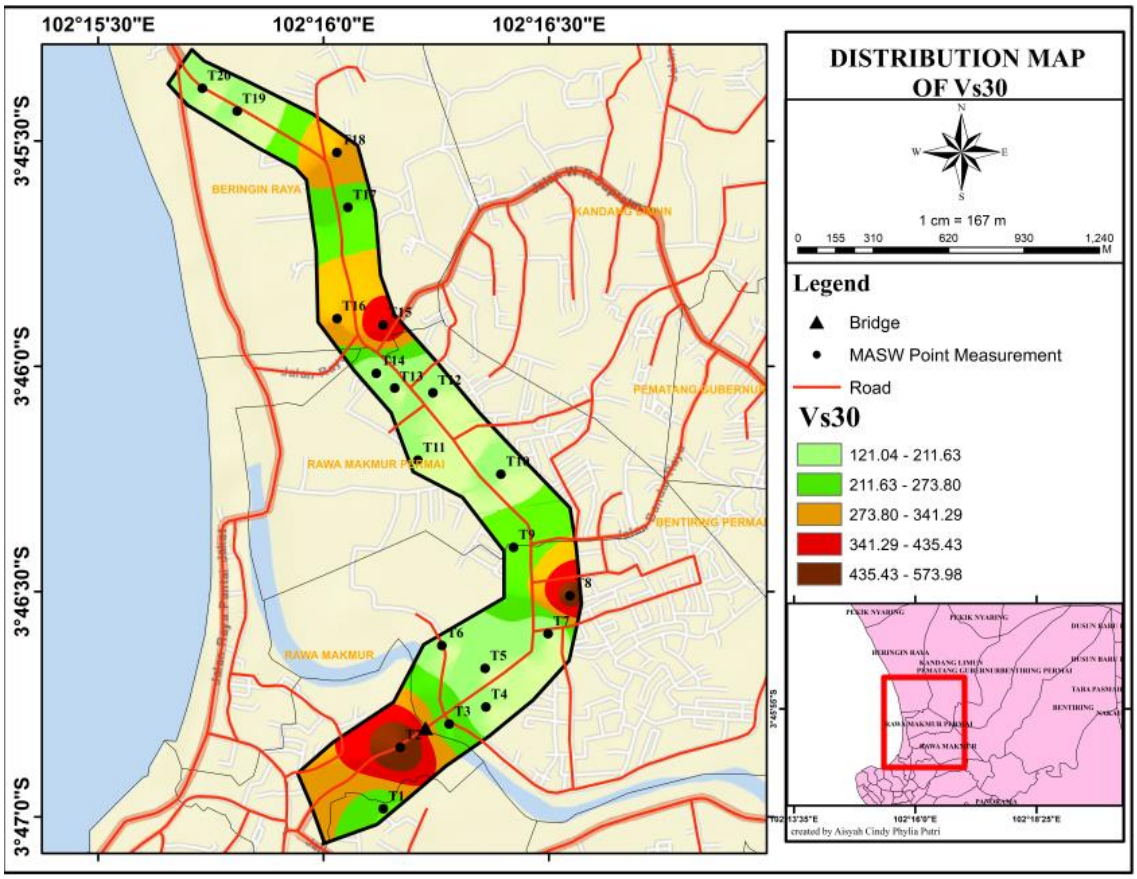

Figure 8. Map of Vs30 by Multichannel Analysis Surface Wave measurements.

Table 3. Vs30 data in the area arround Rawa Makmur by USGS.

No.	Longitude	Latitude	Vs30 (m/s)	Class Classification
1.	102.2667	-3.75833	258.982	SD (medium soil)
2.	102.2667	-3.76667	273.008	SD (medium soil)
3.	102.275	-3.76667	251.46	SD (medium soil)
4.	102.2667	-3.775	258.953	SD (medium soil)
5.	102.275	-3.775	238.575	SD (medium soil)
6.	102.2833	-3.775	245.3	SD (medium soil)
7.	102.2667	-3.78333	286.743	SD (medium soil)
8.	102.275	-3.78333	259.862	SD (medium soil)

The SE class classification for soft soil, with the lowest Vs30 value of 121 m/s and the highest of 172 m/s, marked in green, is located at points T11, T12, T13, and T14, stretching along 500 meters of the road body. Sedimentary layers with Vs30 values <175 m/s are considered layers with low seismic wave velocities, so the risk of experiencing changes is quite high. Relatively non-rigid and low-cohesion soils do not have sufficient strength to resist stresses, so geotechnical planning should be considered to ensure safety and stability.

Data on Vs30 values in the Rawa Makmur area, Bengkulu City (Table 3) published by the USGS shows an average of about 259 m/s which if interpreted this value falls into the soft medium soil classification (SD class) providing strong support for the acquisition results in this study.

As mapped Figure 9, it can be seen that only two locations have Vs30 values exceeding 270 m/s and this value is consistent with the results obtained by MASW processing in the nearby areas.

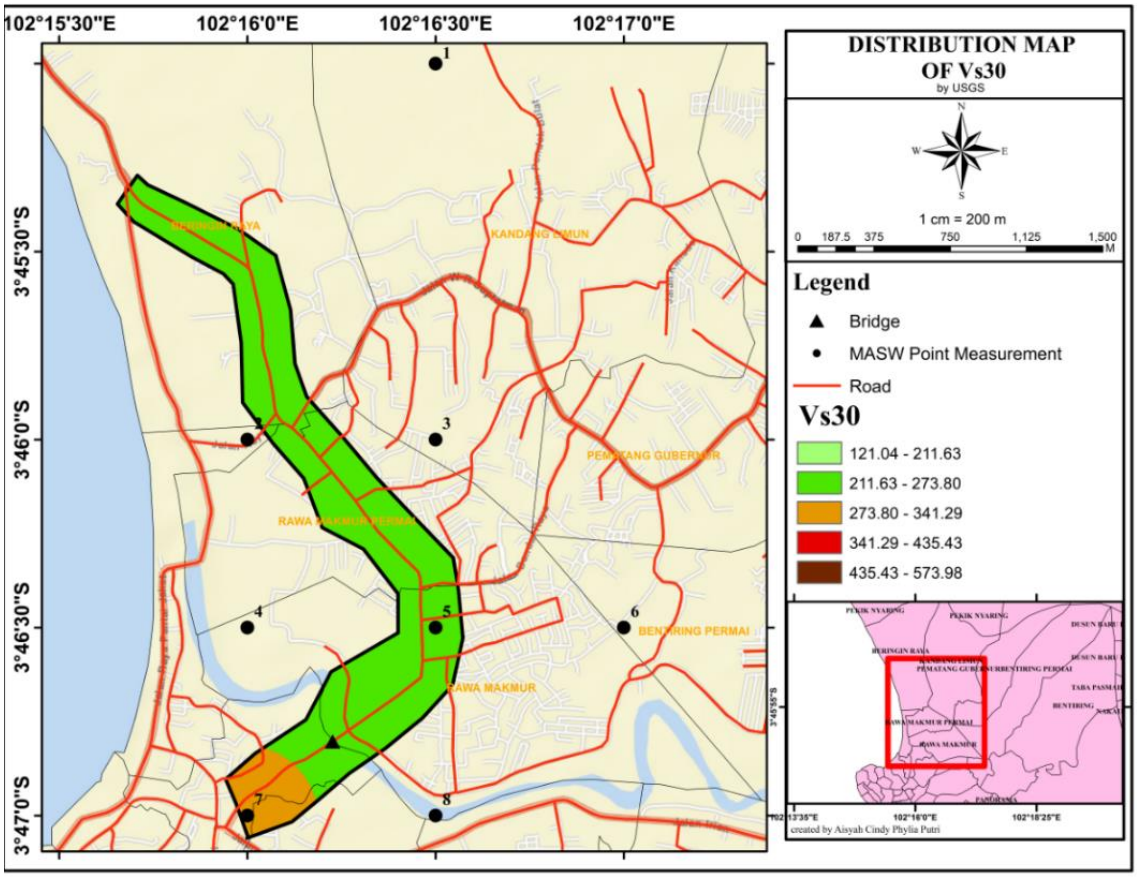

Figure 9. Map of Vs30 values based on USGS data.

Conclusion

The variation of Vs30 values ranges between 121 and 574 m/s, according to measurement data analysis using Multichannel Analysis Surface Wave (MASW) at Rawa Makmur road. The site class map shows the characteristics of these values: Vs30 values between 175 and 350 m/s indicate medium soil and Vs30 values above 350 m/s indicate stable hard soil. However, areas with medium to high stiffness can still experience deformation, especially in some places. Soils with Vs30 below 175 m/s are soft and easily deformed because Kalimantan Highway is located in an area of the Alluvium Terrace Formation (Qat), which is Quaternary in age and thus tends to have an unstable or poorly compacted structure. This condition makes the soil more susceptible to liquefaction and ground shifting, especially when exposed to earthquakes or heavy loads. Geotechnical planning must consider supporting factors to maintain the safety and stability of the structure.

Acknowledgements

Thanks to the Mitigation and Exploration Laboratory of Geophysics Bengkulu University team who have helped in the research process so that this paper can be useful information for the public and thanks also to the lecturers who have advised a lot.

Author Contribution

Aisyah Cindy Phylia Putri provided the main idea, processed the data, and wrote the article. Aisyah Cindy Phylia Putri and Andre Rahmat collected data, created the

survey design, and created the distribution map of the research results. The lecturers who guided this article are Refrizon and Arif Ismul Hadi.

Conflict of Interest

The authors declare no conflict of interest.

References

Al Ansory, A. R., Raihana, H., Farid, M., & Hadi, A. I. (2024). Investigation of Sediment Layer Thickness Estimation at Bengkulu University Hospital Based on Microtremor Data. *Jurnal Geocelebes*, *8*(1), 1–10. https://doi.org/10.20956/geocelebes.v8i1.28144

Ardianto. (2018). *Pemetaan Kecepatan Gelombang Geser (Vs30) Metode Multichannel Analysis of Surface Wave untuk Zonasi Amplifikasi Gempa Wilayah Surabaya Bagian Timur*. ITS.

Building Seismic Safety Council -BSSC. (2003). NEHRP Recommended Provisions for Seismic Regulations for New Buildings and Other Structures (FEMA 450). *Part 1*, *Fema 450*, 338.

Budianto, G., Sinaga, J. E. E., Pritama, V. L., Suhendra., & Halauddin. (2023). Potensi genangan banjir berdasarkan nilai porositas dan resistivitas batuan di kecamatan muara bangkahulu, kota bengkulu. *Wahana Fisika*, 8(1), 76–90. https://doi.org/10.17509/wafi.v8i1.57874

Bustari, A. A., & Wibowo, N. B. (2023). Pemetaan sebaran nilai Vs30, faktor amplifikasi tanah, dan peak ground acceleration wilayah Bantul timur. *Cakrawala Jurnal Ilmiah Bidang Sains*, 1(2), 73–80. https://doi.org/10.28989/cakrawala.v1i2.1436

Butzer, K. W., Helgren, D. M., Fock, G. J., & Stuckenrath, R. (1973). Alluvial Terraces of ohe Lower Vaal River, South Africa: A Reappraisal And Reinvestigation. *The Journal of Geology*, 81(3), 341–362. https://doi.org/10.1086/627875

Dewi, N. A., Tohari, A., & Muttaqien, I. (2020). Evaluasi Potensi Likuifaksi Di Wilayah Cekungan Bandung Berdasarkan Metode Analisis Multi-Sensor Gelombang Permukaan. *RISET Geologi Dan Pertambangan*, 30(2), 241–256. https://jrisetgeotam.lipi.go.id/index.php/jrisgeotam/article/view/1131

El Oshebi, F. M., Shaltami, O. R., Fares, F. F., Al Barghathi, J. A., El Ogali, M., Errishi, H., & Badi, A. M. (2020). Alluvial Terraces As a Measure of Vertical Movements and Neotectonics: Evidences From Wadi Sidi Moussa, Cyrenaica, NE Libya. *EPH - International Journal of Applied Science*, 6(3), 25–32. https://doi.org/10.53555/eijas.v6i3.96

Hadi, A. I., Refrizon, R., Halauddin, H., Lidiawati, L., & Edo, P. (2021). Interpretasi Tingkat Kekerasan Batuan Bawah Permukaan di Daerah Rawan Gempa Bumi Kota Bengkulu. *Indonesian Journal of Applied Physics*, 11(1), 11–24. https://doi.org/10.13057/ijap.v11i1.46525

Hasya, C. A., Khaizal, K., & Irwandi, I. (2021). Perbandingan Metode Multichannel Analysis of Surface Wave dan Metode Cone Penetration Test Terhadap Analisis Lapisan Tanah. *Journal of The Civil Engineering Student*, 3(1), 8–14. https://doi.org/10.24815/journalces.v3i1.12265

Kementerian Pekerjaan Umum dan Perumahan Rakyat. (2016). *Spesifikasi Pekerjaan Tanah*.

Lantu, L., Aswad, S., Fitriani, F., & Marjiyono, M. (2018). Pemetaan Wilayah Rawan Bencana Gempabumi Berdasarkan Data Mikrotremor Dan Data Bor. *Jurnal Geocelebes*, 2(1), 20–30.

https://doi.org/10.20956/geocelebes.v2i1.3721

Lin, C.-P., Chang, C.-C., & Chang, T.-S. (2004). The use of MASW method in the assessment of soil liquefaction potential. *Soil Dynamics and Earthquake Engineering*, 24(9–10), 689–698. https://doi.org/10.1016/j.soildyn.2004.06.012

Lubis, A. M., Saputra, A., Suhendra, S., Saputra, R., & Samdara, R. (2021). Penentuan Ketebalan Sedimen pada Segmen Kumering, Sesar Sumatra di Daerah Liwa Lampung Barat dengan Menggunakan Metode Seismik Aktif MASW. *Jurnal Lingkungan Dan Bencana Geologi*, 12(3), 137–147. https://doi.org/10.34126/jlbg.v12i3.334

Mase, L. Z., Sugianto, N., & Refrizon. (2021). Seismic hazard microzonation of Bengkulu City, Indonesia. *Geoenvironmental Disasters*, 8(5), 1–17. https://doi.org/10.1186/s40677-021-00178-y

Mufardis, A., Khaizal, K., & Irwandi, I. (2023). Pemetaan Vs30 dan Analisis Potensi Likuifaksi Berdasarkan Vs Menggunakan Metode MASW di Kecamatan Banda Raya dan Jaya Baru Kota Banda Aceh. *Journal of The Civil Engineering Student*, 5(2), 162–168. https://doi.org/10.24815/journalces.v5i2.20992

Muzli, M., Mahesworo, R. P., Madijono, R., Siswoyo, S., Pramono, S., Dewi, K. R., Budiarta, B., Sativa, O., Sulistyo, B., Swastikarani, R., Oktavia, N., Moehajirin, M., Efendi, N., Wijaya, T. A., Subadyo, B., Mujianto, M., Suwarto, S., & Pramono, S. (2016). Pengukuran Vs30 Menggunakan Metode MASW Untuk Wilayah Yogyakarta. *Jurnal Meteorologi Dan Geofisika*, 17(1), 25–32. https://doi.org/10.31172/jmg.v17i1.374

Nofirman. (2016). Interpretasi Satuan Litologi, Satuan Bentuk Lahan, dan Struktur Geologi dengan Integrasi Citra SRTM Di Wilayah Kota Bengkulu. *Jurnal Geografflesia*, 1(2), 27–37.

Ólafsdóttir, E. Á., Erlingsson, S., & Bessason, B. (2017). Tool for analysis of MASW field data and evaluation of shear wave velocity profiles of soils. *Canadian Geotechnical Journal*, 55(2), 217–233. https://doi.org/10.1139/cgj-2016-0302.

Oldknow, C. J., & Hooke, J. M. (2017). Alluvial terrace development and changing landscape connectivity in the Great Karoo, South Africa. Insights from the Wilgerbosch River catchment, Sneeuberg. *Geomorphology*, 288, 12–38. https://doi.org/10.1016/j.geomorph.2017.03.009

Park, C. B., Miller, R. D., & Xia, J. (1999). Multichannel analysis of surface waves. *Geophysics*, 64(3), 800–808. https://doi.org/10.1190/1.1444590

Prasisila, M., Refrizon., & Hadi, A. I. (2021). Klasifikasi Kelas Situs Tanah dengan Nilai Vs30 di Kecamatan Muara Bangkahulu Kota Bengkulu menggunakan Metode Multichannel Analysis of Surface Wave (MASW). *Prosiding Seminar Nasional Fisika*, *7.0*, 277–282. http://proceedings.upi.edu/index.php/sinafi/article/view/1843/1644

Rosyidi, S. A. P. (2015). Pemetaan Daya Dukung Tanah Dan Diskontinuitas Struktur Tanah Dasar Menggunakan Metode *Multi- Channel Analysis of Surface Waves* (MASW). *Seminar Nasional Teknik Sipil V Tahun 2015 - UMS*, G-161–G-169. https://publikasiilmiah.ums.ac.id/handle/11617/6427

Sugianto, N., Farid, M., & Suhendra, S. (2017). Kondisi Geologi Lokal Kota Bengkulu Berdasarkan Ground Shear Strain (GSS). *Spektra: Jurnal Fisika*

Dan Aplikasinya, 2(1), 29–36. https://doi.org/10.21009/spektra.021.05

Suhono, T., & Al Fatta, H. (2021). Penyusunan Data Primer sebagai Dasar Interoperabilitas Sistem Informasi pada Pemerintah Daerah menggunakan Diagram RACI (Studi Kasus: Pemerintah Kabupaten Purworejo). *Jnanaloka*, 2(1), 35–44. https://doi.org/10.36802/jnanaloka.2021.v2-no1-35-44

Suparno., Feriska, Y., Pramono, H., Khamid, A., & Apriliano, D. D. (2023). Analisa Kerusakan Jalan Kabupaten Ruas Klampok – PG Banjaratma Kabupaten Brebes. *Journal of Science, Engineering and Information Systems Research*, 1(1), 10–18. https://jurnal.eraliterasi.com/index.php/erasains/article/view/98/84

Susilanto, P., & Ngadmanto, D. (2015). Analisis Kecepatan Gelombang Geser (Vs) di Cilacap, Jawa Tengah sebagai Upaya Mitigasi Bencana Gempabumi. *Jurnal Meteorologi dan Geofisika*, 16(1), 57–64. https://doi.org/10.31172/jmg.v16i1.263

Susilanto, P., Ngadmanto, D., Sunardi, B., & Rohadi, S. (2019). Analisis Kecepatan Gelombang Geser (Vs) Sebagai Upaya Mitigasi Bencana Gempabumi di Kulonprogo, DIY. *Jurnal Lingkungan Dan Bencana Geologi*, 10(2), 41–50. https://doi.org/10.34126/jlbg.v10i2.215

Vikki., Azwar, A., Zulfian., Arman, Y., & Perdhana, R. (2022). Pendugaan Penyebab Keretakan Jalan di Desa Serindang Berdasarkan Interpretasi Data Geolistrik. *Jurnal Kumparan Fisika*, 5(3), 201–210. https://doi.org/10.33369/jkf.5.3.201-210

Zawawi, A. F., Sunardi, B., & Prayoedhie, S. (2023). Penentuan Klasifikasi Tanah Dengan Menggunakan Metode Multi-channel Analysis of Surface Waves Di Kapanewon Pleret, Kabupaten Bantul. *Jurnal Stasiun Geofisika Sleman*, 1(2), 01–05. https://jurnal.stageofsleman.id/index.php/jsgs/article/view/6

ISSN: 2579-5821 (Print)
ISSN: 2579-5546 (Online)
URL address: http://journal.unhas.ac.id/index.php/geocelebes
DOI: 10.70561/geocelebes.v9i1.40206

Jurnal Geocelebes Vol. 9 No. 1, April 2025, 15 – 27

Analysis of Landslide Hazard Levels on the Palopo – Luwu Road using GIS and Finite Element Method

Anshar Abdullah Jawil*, Kadek Nando Setiawan

Department of Mining Engineering, University Andi Djemma, Palopo 91922, Indonesia.

*Corresponding author. Email: anshar@unanda.ac.id

Manuscript received: 23 September 2024; Received in revised form: 6 March 2025; Accepted: 23 April 2025

Abstract

Indonesia is one of the countries that often experiences landslides during the rainy season. The Palopo–Luwu main road is a landslide-prone area in North Bastem sub-district because it has a topographic condition with a very steep slope. Therefore, it is important to conduct research on the analysis of the potential for landslides in the area. The method used in this study is Weighted Overlay based on Geographic Information Systems (GIS) in making landslide-prone maps. Data processing with weighting or scoring on parameters such as slope, rainfall, rock type, soil type, and land cover. While the Finite Element Method (FEM) is used to model slope stability with input data on physical and mechanical properties of rocks and slope geometry data as a basis for calculating the slope safety factor (FK). The results of the study showed that almost 85% of the research area is a high landslide potential area which is the Palopo–Luwu main road area, this was validated from laboratory test data which was then analyzed for slope stability showing FK value <1.25, which is 0.936 and the actual condition of the slope in the field has collapsed. The mapping results can be used as a useful tool for land use planning and risk reduction in the research area.

Keywords: FEM; FK; GIS; landslide; weighted overlay.

Citation: Jawil, A. A., & Setiawan, K. N. (2025). Analysis of Landslide Hazard Levels on the Palopo – Luwu Road using GIS and Finite Element Method. *Jurnal Geocelebes*, 9(1): 15–27, doi: 10.70561/geocelebes.v9i1.40206

Introduction

Indonesia is one of the countries that often experiences landslides during the rainy season (Susilo et al., 2020). A landslide is the movement of earthen materials down a slope under the influence of gravity and occurs when earthen material exceeds the shear strength (Pawluszek et al., 2020; Jawil & Pontus, 2023). landslides can be regarded as one of the most frequent geological hazards in mountainous areas (Chen & Zhang, 2021). Researchers found the factors most important for landslides to be geological and geomorphological conditions, precipitation, in addition to disturbances due to human activity playing an important role in the occurrence of landslides (Neamat & Karimi, 2020). Landslide disasters can result in loss of biodiversity, human lives, property, and damage to infrastructure (Saleem at al., 2020). Luwu Regency is one of the regencies that has the potential to be prone to landslides. According to disaster data from South Sulawesi Province, there have been 18 landslides in Luwu Regency since July 2021, while in North Bastem District itself, there have been 3 landslides since 2023. One of the recent landslide disasters occurred on February 26, 2024 on the Palopo-Luwu main road, which killed 5 residents and cut off access to the intercity road.

The high incidence of landslides in the North Bastem area, which is the only traffic route between Palopo City and Luwu Regency, requires research on the analysis of the potential for landslides, especially in

the Palopo–Luwu main road area. Therefore, it is important to conduct research with a combination of several methods to obtain more accurate results in predicting or modeling the landslide potential of an area.

Advances in information and communication technology are developing very rapidly, especially Geographic Information Systems (GIS). This system can be used to analyze disaster risks by considering spatial data in more detail. GIS is considered an efficient and cost-effective technology that can display a large set of geographically referenced data, by combining physical processes and disaster-causing factors (Wang et al., 2020). The results of landslide vulnerability mapping are then validated with the results of slope stability analysis using FEM (Finite Element Method). The safety factor (FK) value is used to ensure that the slope is in a safe condition. The safety factor value is obtained from the comparison of the total retaining force to the force that causes the slope to collapse. The combination of these two methods is used to obtain spatial information. The results of laboratory testing are used for slope stability modeling which strengthens the results of spatial landslide potential mapping. This is very important to do to get an initial picture of the areas that are included in the Red Zone and still have a high level of landslide potential.

The FEM stress-strain assessments are usually applied to evaluate the landslide body's progressive failure as well as to introduce initial velocity and later acceleration up to the moment major deformations are observed in the slope and computational convergence is achieved (Cuomo et al., 2021). FEM has been reported to be more effective for slope stability analysis (Chen et al., 2019). This is observed by Li et al. (2016), due to the considerable reduction in the number of analyses required in the calculation process which subsequently leads to an improvement in computational efficiency at low probability levels and this is important in slope design practice. The approach proposed in this study allows the utilization of information obtained from a simple method (GIS) in a more advanced model, FEM, to ensure reliability

Materials and Methods

Collecting Data

The data collection used is primary data and secondary data. Primary data is data obtained from direct measurements in the field, such as rock samples and slope geometry (Figure 1). Field investigations are conducted to determine field conditions by taking documentation photos of slope conditions, geology, and vegetation (Figure 2). While secondary data is obtained from several related agencies and official government sites such as land use maps, soil types, geological conditions, rainfall, and topographic data of the research area.

Figure 1. (left) Measurement of slope geometry, and (right) Soil Sampling.

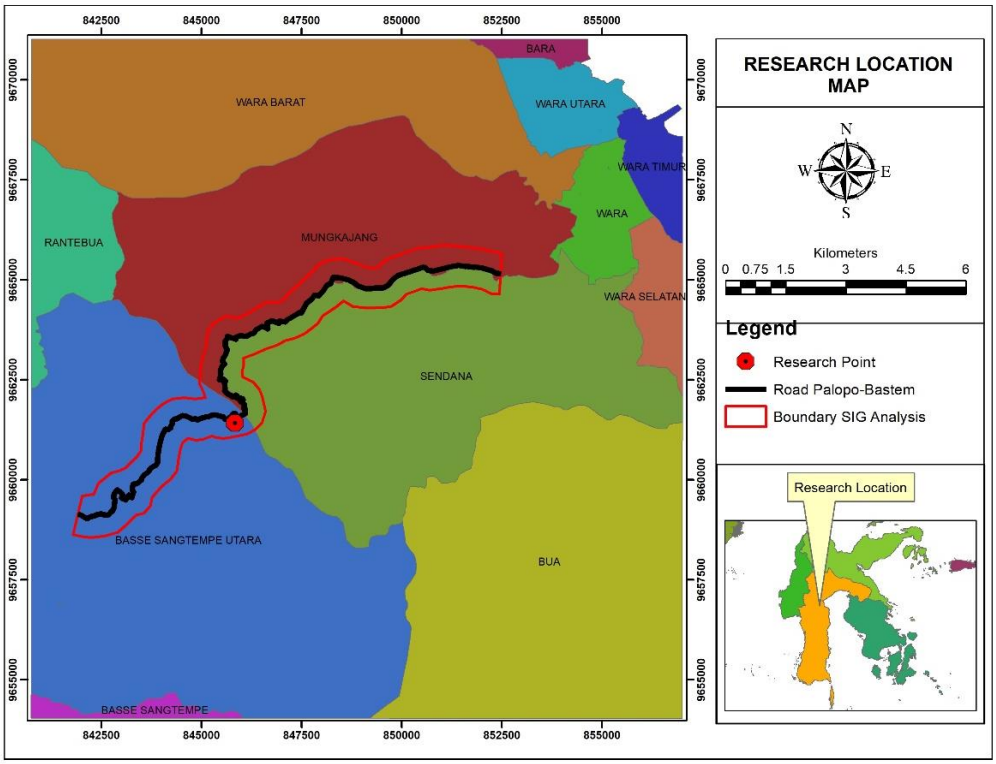

Figure 2. Research location map.

Data Processing and Laboratory Testing

The method used in making landslide susceptibility maps is Weighted Overlay. This technique combines the weighting of each parameter and the scoring of each parameter class (Khatun et al., 2023). Then the rainfall map, rock type map, soil type map, land cover map are overlaid to get an overview of the landslide level in the research area. Laboratory tests were conducted on 10 rock samples to obtain rock property values including physical properties (unique weight and water content) and mechanical properties (cohesion and friction angle). The results of laboratory analysis were used as input for rock layer property values. slope stability modeling using the FEM.

Direct shear test includes determining the shear strength of consolidated drained and consolidated undrained soil materials in a direct shear test. This test is carried out by forming a specimen which is then passed through a shear test equipment media with a loading speed that can be adjusted (Du et al., 2021). FEM is a method of analyzing rock/soil slopes that are divided into several small block zones, in this research model it is divided into 4,500 number of surfaces computed (Pilecka et al., 2022). Elements in a reduced zone are connected by node points. The analysis involves calculating displacements at each node, then using interpolation functions (shape functions) to estimate stresses and strains within elements (Brady & Brown, 2006). The factor of safety (FK) is derived from these computations using slope modeling software.

The Bishop method is used to analyze the slip surface. In this method, it is assumed that the total normal forces are located/ working at the center of the base of the section and can be determined by decomposing the forces on the section vertically or normally (Nath et al., 2021). Equilibrium requirements are applied to the sections that form the slope. The Bishop method assumes that the forces acting on the section have a zero resultant in the vertical direction. This method reduces the shear strength to describe the slope failure,

so the value obtained from this approach is used as a safety factor.

Data analysis

Data analysis was carried out by comparing the results of landslide disaster potential mapping using GIS and the results of slope stability modeling using FEM, the classification of landslide vulnerability levels will be confirmed by the slope safety factor value from the modeling input with field data. Slope stability modeling also conducted sensitivity analysis on the input rock material properties. The parameters used in landslide vulnerability mapping are slope gradient, rainfall, rock type, soil type, and land cover. The percentage of indicator weight of each parameter refers to PU Regulation No. 22 of 2007.

Results and Discussion

Land Slope

The slope of the research area is divided into 5 classes with 90% of the area being dominated by slopes above 25% (Figure 3). This defines that the research area is a steep topography. The main road of Palopo–Luwu crosses between the steep cliffs. Steep slopes or cliffs will increase the driving force. Steep slopes are formed due to erosion by river water, springs, sea water, and wind.

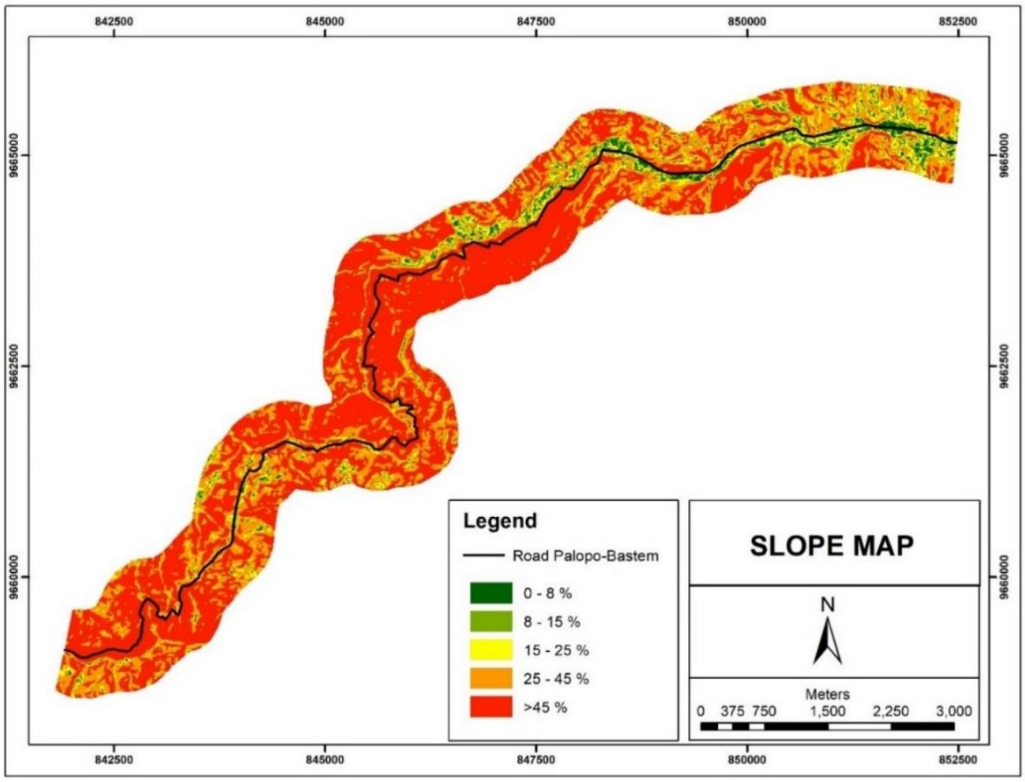

Figure 3. Land slope classification.

Table 1. Land slope classification.

Slope %	Weight	Score
>45		5
30-45		4
15-30	20%	3
8-15		2
<8		1

Land slope has a weight of 20% with the highest score being 5 for land slopes above 45% (Table 1). According to Rawat & Pant (2023), land with a slope of more than 45% has greater potential compared to land with a slope below 45%. The steep slope of the land also causes the runoff water to flow quickly, which can cause erosion which is an early symptom of landslides.

Rainfall

The research area is a plateau, so the rainfall in the area is quite high, that is 3000 - 3500 mm/year included in a very wet area with an assessment score of 5 (Figure 4). The rainfall factor has a weight of 30% (PU Regulation No. 22 of 2007). High rainfall can be a supporting factor for landslides (Liu et al., 2021). In mountain regions, landslides are often triggered by intensive rainfall. Rainfall and infiltration enhance moisture content, which further decreases the matrix suction and soil shear strength (Huang et al., 2021). According to Liu (2021), landslides were triggered by rainfall of a certain intensity and, according to the results obtained from the present tests, the rainfall intensity must exceed 40 mm/h to trigger a landslide.

A long dry season will cause large amounts of water to evaporate on the surface of the soil. Pores or cavities in the soil will appear, then cracks and fissures will occur on the surface. When it rains, water will seep into the cracked parts. The soil will quickly expand again. At the beginning of the rainy season, the water content in the soil becomes saturated in a short time. Heavy rain at the beginning of the season can cause landslides because through the cracked soil, water will enter and accumulate at the base of the slope, causing lateral movement. If there are trees on the surface, landslides can be prevented because the water will be absorbed by the plants. Plant roots also function as soil binders.

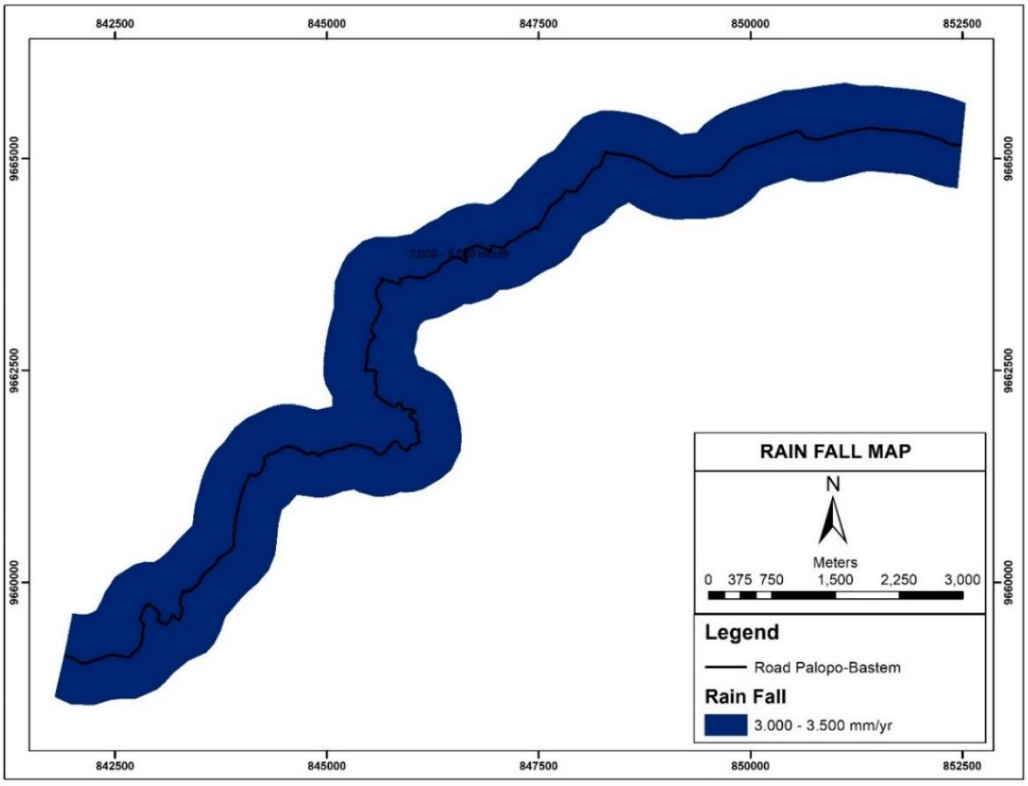

Figure 4. Rain fall map.

Rock Type

The nature of each rock is different, it depends on the origin of the formation of the rock. In general, rocks are influenced by texture, structure, fracture, mineral content, weather, and sedimentation. Morphologically, the area in the Malili sheet is divided into 4 units, which are Mountainous Area, Hilly Area, Karst Area, and Plains Area (Simandjuntak et al., 2007). The mountainous area occupies the western - southeastern part of the Malili sheet. The Hilly Area occupies the central to northeastern part of the Malili sheet, with

an altitude between 200 – 700 meters above sea level. The Karst Region occupies the northeastern part of the Malili sheet, with an elevation ranging between 800–1700 meters above sea level (masl), formed by limestone. The Lowland Region covers the southern part of the Malili sheet, stretching from north of Palopo, Sabbang, and Masamba to Bone-Bone.

The Majene Sheet and the Western Part of the Palopo Sheet are formed by various types of rocks such as sedimentary, metamorphic, volcanic, and intrusive rocks. Their ages range from Mesozoic to Quaternary. The oldest unit in this Sheet is Metamorphic Rock (TRw) which consists of schist, genes, phyllite and slate. This unit may be equated with the Wana Complex in the Pasangkayu Sheet which is thought to be older and Cretaceous and is overlain unconformably by the Latimojong Formation (Kls). The formation is composed of phyllite, quartzite, metamorphic mudstone, and marble, of Cretaceous age (Figure 5).

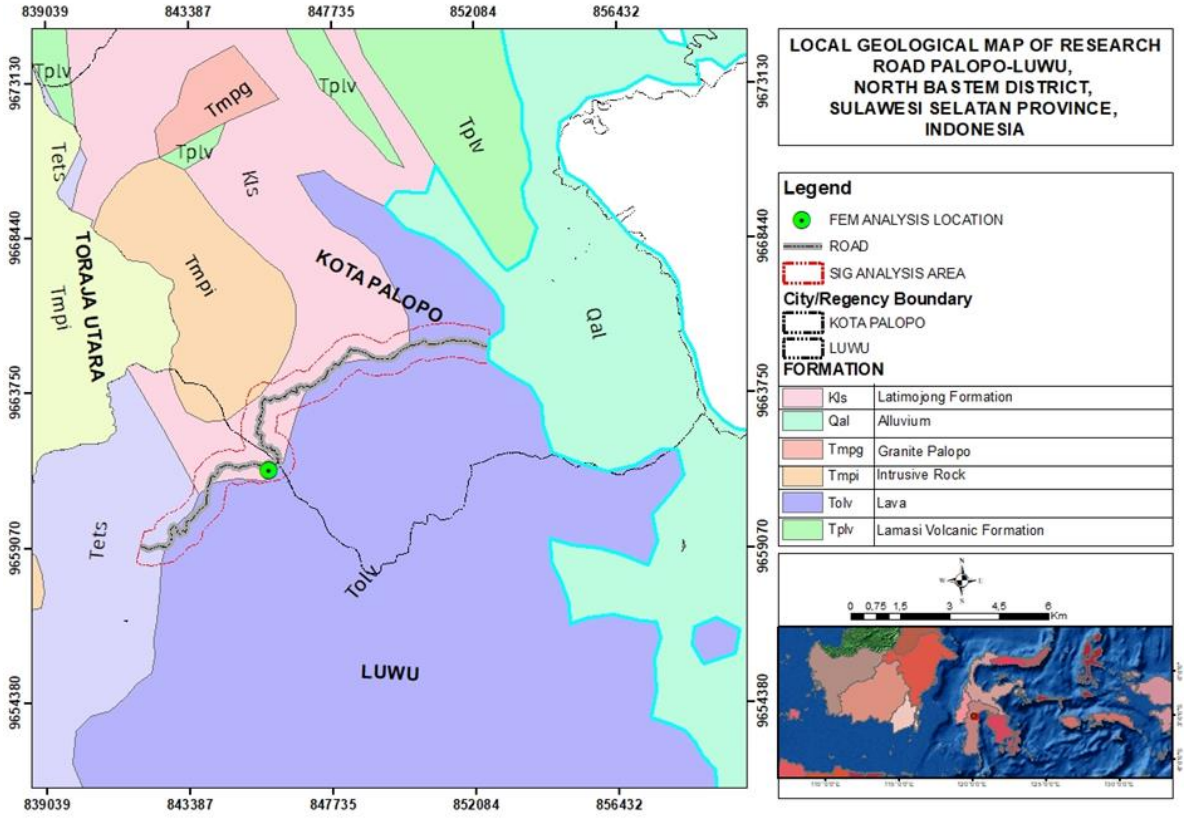

Figure 5. Geological map (modified from Simandjuntak et al., 2007).

Table 2. Rock type classification.

Rock Type	Weight	Score
Alluvial Plain		1
Alluvial Plain (lava)		1
Granite Hills	20%	3
Limestone Hills		2
Limestone Hills (shale)		2

In the research area there are 5 types of rocks, that is alluvial plains, alluvial plains (lava), granite hills, limestone hills, and limestone hills (shale) (Figure 6 and Table 2). The research area is dominated by limestone hills with an area of 0.128 km^2, alluvial plains with an area of 0.123 km^2 and granite hills with an area of 0.025 km^2. In general, volcanic sedimentary rocks and sedimentary rocks are sand-sized and a mixture of gravel, sand, and clay is less strong. These rocks will easily become soil if they experience a weathering process and are generally susceptible to landslides if they are on steep slopes.

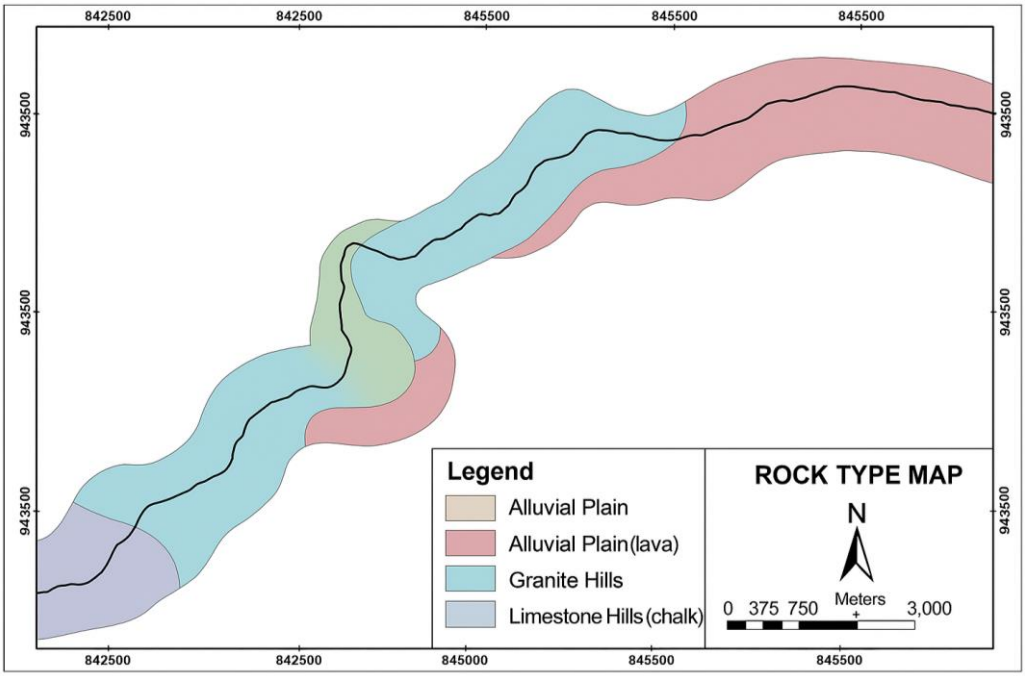

Figure 6. Rock type classification.

Soil Type

The types of soil in the research area are divided into 3, that is alluvial with a score of 1, regosol (ferric arcrisols) and regosol (orthic arcrisols) with a score of 5 (Figure 7). The specific gravity of the soil contributes 15% (Table 3).

Table 3. Soil Type Classification

Soil Type	Weight	Score
Aluvial	15%	1
Regosol (ferric arcrisols)		5
Regosol (Orthic Arcrisols)		5

Land Cover

Table 4. Land cover classification.

Land Cover	Weight	Score
Thicket	15%	4
Dry Forest		3
Settlement		2

Land cover in the research area is divided into three areas (Table 4), that is the thicket area is the largest area, that is 96%, while the residential area and dry land forest are around 4% (Figure 8).

Landslide Potential Map

Based on the results of the total score analysis of the parameters at the research location, 3 landslide vulnerability class classifications were obtained, that is low, medium, and high potential. The high landslide potential area is 372 hectares (42.4%), medium potential is 371 hectares (42.3%) and low potential is 134 hectares (15.2%). The vulnerability level of the landslide potential zone is high if the total weighted value is in the range of 2.40 - 3.00, the vulnerability level is medium if the total weighted value is in the range of 1.70 - 2.39, the vulnerability level is low if the total weighted value is in the range of 1.00 - 1.69. The assessment of the vulnerability level of a landslide potential zone is carried out by adding the weighted values of 5 (five) indicators of slope, rainfall, rock type, soil type, and type of land cover is 134 hectares (15.2%) (Figure 9).

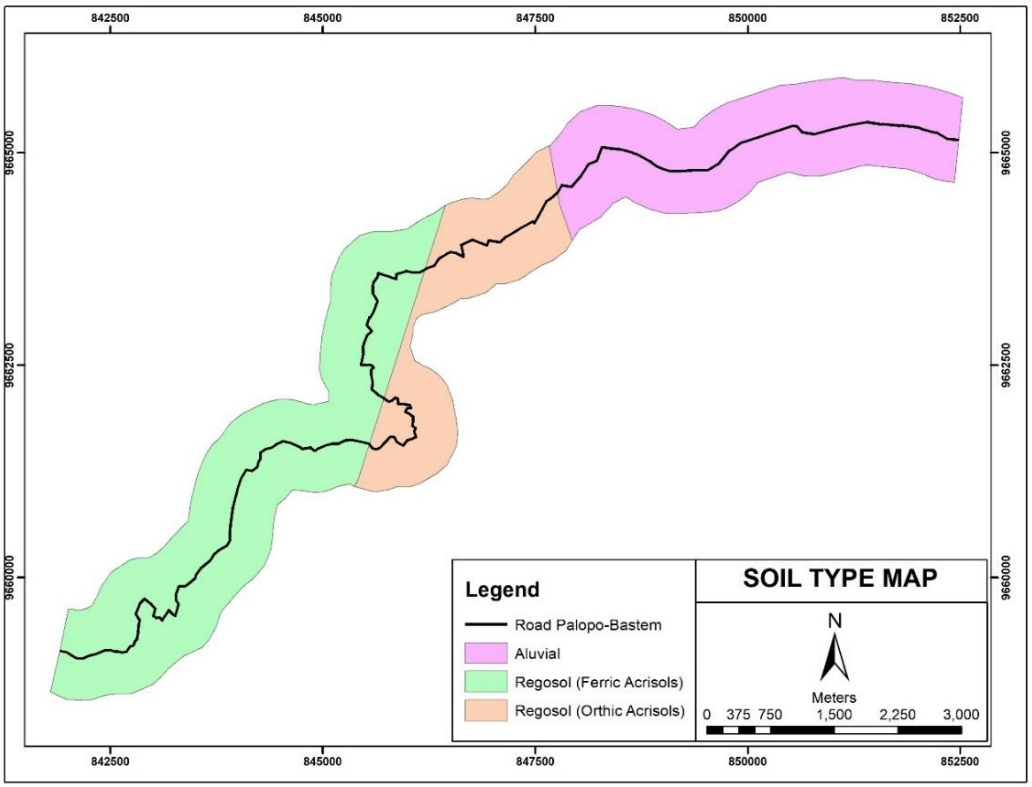

Figure 7. Soil type classification.

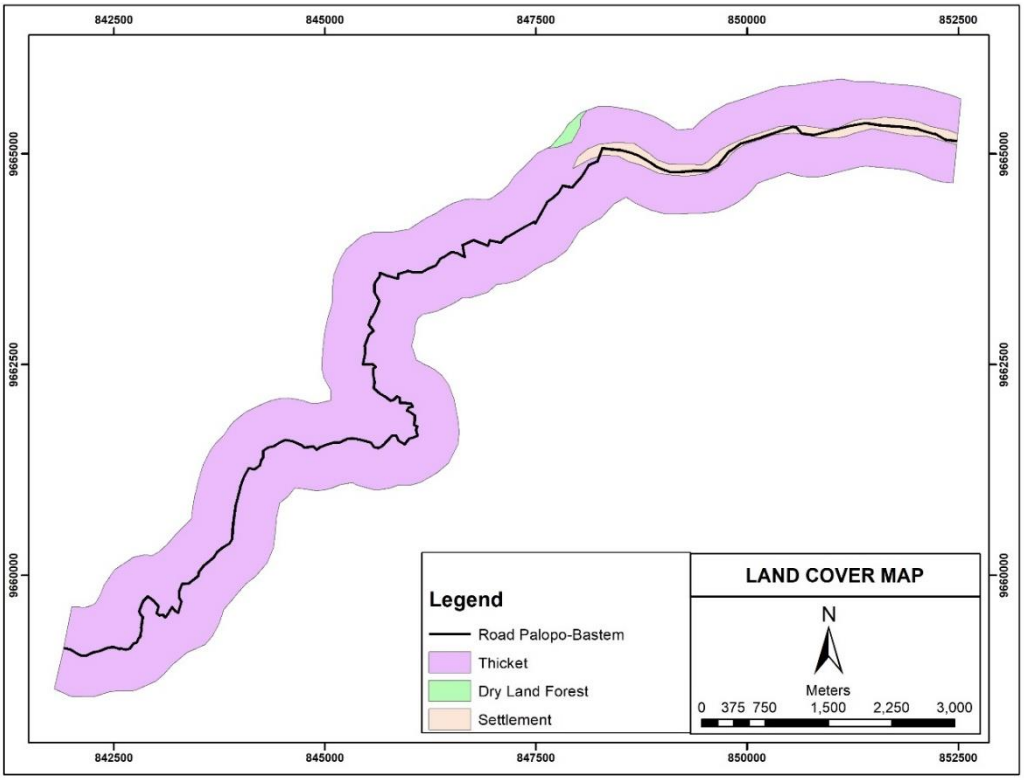

Figure 8. Land Cover Classification

These results show that almost 85% of the research area is an area with a high level of landslide s, which is a concern in carrying out prevention or monitoring in at the red zone points of the Palopo–Luwu main road.

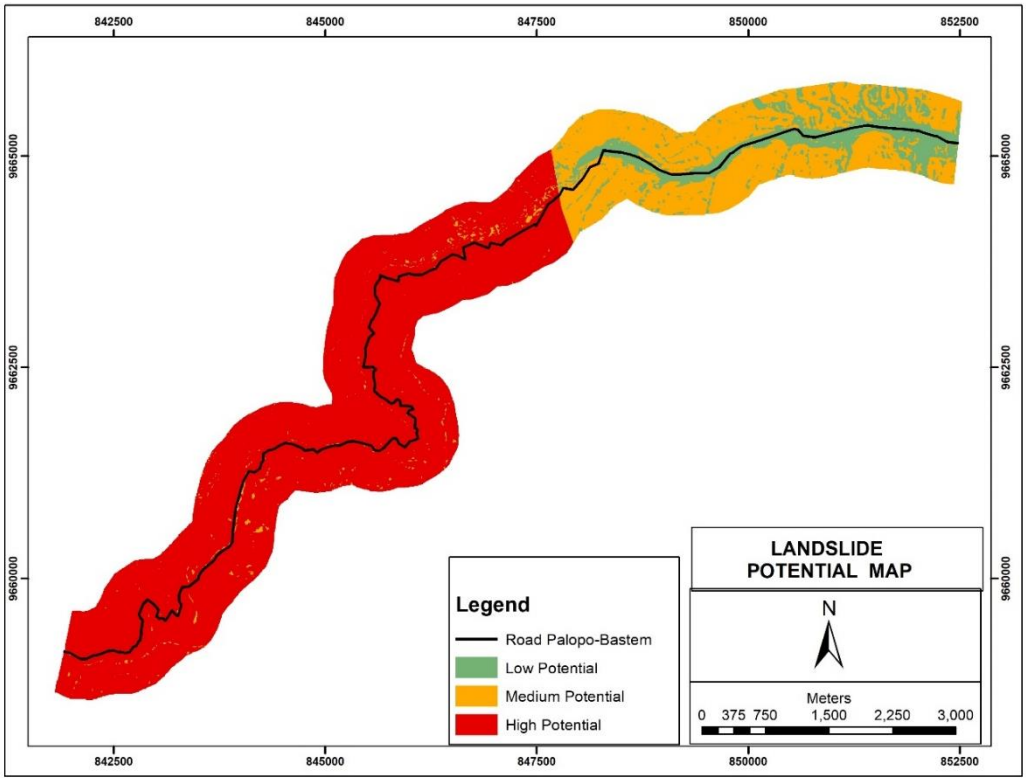

Figure 9. Landslide potential map.

Testing of Physical and Mechanical Properties of Rocks

From the results of laboratory testing of the physical properties of soil samples in the research area, the values of water content, wet soil density, dry soil density were obtained, while the mechanical properties test was in the form of cohesion values and friction angles in the topsoil layer. The test results of 10 soil samples have a cohesion value of 0.325 - 0.701 kg/m^3 and an internal friction angle of 30 - 42 degrees (Table 5).

Table 5. Direct shear strength test.

ID	Easting	Northing	Cohesion	Natural Angle of Repose
LR1-01	844,109.214	9,662,057.656	0.626	40
LR1-02	844,108.612	9,662,051.532	0.350	37
LR2-01	844,109.214	9,662,057.656	0.350	40
LR2-02	844,109.318	9,662,057.677	0.525	39
LR3-01	844,083.856	9,662,077.134	0.701	39
LR3-02	844,083.917	9,662,077.398	0.701	39
LR4-01	844,079.918	9,662,079.513	0.325	30
LR4-02	844,079.965	9,662,079.422	0.601	42
LR5-01	844,086.201	9,662,071.984	0.400	40
LR5-02	844,009.432	9,662,079.167	0.400	35

The water content in the soil samples ranges from 12.05% - 33.90%, the wet weight ranges from 1.54 - 2.03 gr/cm^3 and the dry weight is 1.21 - 1.80 gr/cm^3 (Table 6).

Based on field observations, the layer beneath the soil consists of weathered shale, underlain by basalt rock. The determination of uniaxial compressive strength (UCS) values for the weathered shale and basalt in the field refers to the rock and soil strength classification guidelines (Wyllie & Mah, 2004).

Field observations indicate that the weathered shale falls into the 'Easily scraped by a fingernail (S5)' category, with

an estimated UCS range of 3 MPa. Meanwhile, the basalt is classified as 'Hard rock - requires a single hammer blow to fracture (R4),' yielding an estimated UCS of 60 MPa.

These field observations were used to estimate the mi, GSI, and disturbance factor values for both the weathered shale and basalt. Subsequently, the cohesion and internal friction angle values were employed to determine and the results of which are presented in Table 7 (Hoek & Brown, 2019).

Table 6. Water content and density test.

ID	Long	Lat	Average Moisture Content	Wet Density	Dry Density
LR1-01	844,109.214	9,662,057.656	12.43	2,029	1,805
LR1-02	844,108.612	9,662,051.532	12.05	1,617	1,443
LR2-01	844,109.214	9,662,057.656	12.90	1,629	1,443
LR2-02	844,109.318	9,662,057.677	15.94	1,797	1,550
LR3-01	844,083.856	9,662,077.134	27.41	1,618	1,270
LR3-02	844,083.917	9,662,077.398	17.82	1,859	1,578
LR4-01	844,079.918	9,662,079.513	32.34	1,605	1,213
LR4-02	844,079.965	9,662,794.227	25.80	1,765	1,403
LR5-01	844,086.201	9,662,071.984	24.08	1,540	1,242
LR5-02	844,009.432	9,662,079.167	33.90	1,688	1,261

Table 7. Hoek and Brown classification (Hoek & Brown, 2019).

Hoek and Brown Classification		Weathered Layer	Basalt Bed Rock
UCS of Intact Rock	sigci	3 Mpa	60 Mpa
Geological Strength Index	GSI	10	30
Material constant	m_i	25	25
Disturbance Factor	D	0	0
Mohr-Coulomb Fit			
Cohesion	C	0.043	0.031
Friction	phi	31.97	57.28

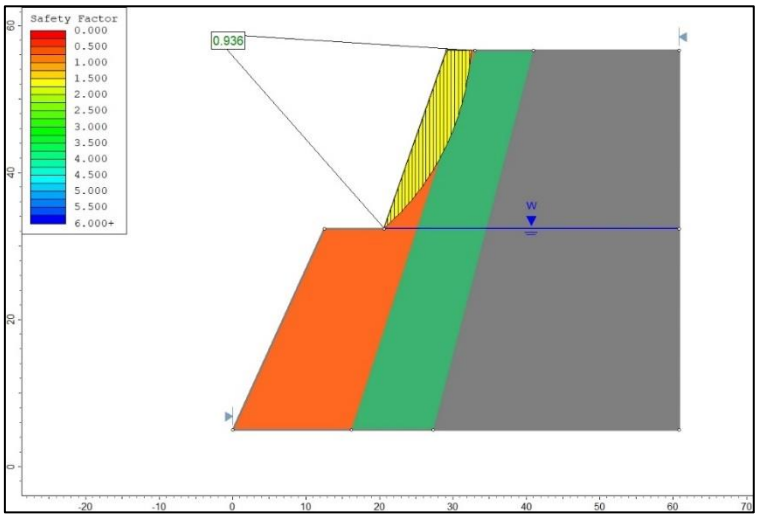

Figure 10. Landslide analysis.

The high potential for landslides on road slopes is caused by the discontinuity planes found on the slopes and the slope geometry that is not in accordance with the research of Loilatu & Iswandaru (2022) which proves the influence of slope geometry on landslides. In this study, slope stability analysis was carried out using geometry based on field surveys, which is an upper slope slope of 75 degrees with a road width of 10 meters and a lower slope slope of 65 degrees, which shows a very steep geometry, resulting in an FK value of 0.396 or <1.25 which indicates that the slope

conditions are less stable and have the potential for landslides (Figure 10). This is in accordance with the results of mapping using GIS which on coordinate 844,083.917 (Easting) and 9,662,077.398 (Northing) shows that the area is an area with high landslide potential (Figure 9).

Conclusion

The results of the study showed that almost 85% of the research area is a high landslide potential area which is the Palopo–Luwu main road area, this was validated from laboratory test data which was then analyzed for slope stability showing an FK value <1.25, which is 0.936 and the actual condition of the slope in the field has collapsed.

Acknowledgements

This research was supported by the POP BIMA Research Grant (2024) from the Ministry of Education, Culture, Research, and Technology, Republic of Indonesia. The authors gratefully acknowledge the Department of Mining Engineering, University Andi Djemma, for providing laboratory facilities and technical assistance. We also thank the Luwu Regency Government for sharing geospatial data and the student research team for their contributions to field data collection.

Author Contributions

Anshar Abdullah Jawil provided conceptualization, funding acquisition, methodology, supervision, writing original draft. Kadek Nando Setiawan provided data curation, formal analysis (GIS/FEM), software, visualization, writing—review & editing. Both authors contributed equally to fieldwork, validation, and manuscript finalization.

Conflict of Interest

The authors declare no financial or personal conflicts of interest.

References

Brady, B. H. G., & Brown, E. (2006). *Rock Mechanics For Underground Mining*. Chapman and Hall.

Chen, W., & Zhang, S. (2021). GIS-based comparative study of Bayes network, Hoeffding tree and logistic model tree for landslide susceptibility modeling. *Catena*, 203, 105344. https://doi.org/10.1016/j.catena.2021.105344

Chen, X., Zhang, L., Chen, L., Li, X., & Liu, D. (2019). Slope stability analysis based on the Coupled Eulerian-Lagrangian finite element method. *Bulletin of Engineering Geology and the Environment*, 78(6), 4451–4463. https://doi.org/10.1007/s10064-018-1413-4

Cuomo, S., Di Perna, A., & Martinelli, M. (2021). Modelling the spatio-temporal evolution of a rainfall-induced retrogressive landslide in an unsaturated slope. *Engineering Geology*, 294, 106371. https://doi.org/10.1016/j.enggeo.2021.106371

Du, K., Li, X., Wang, S., Tao, M., Li, G., & Wang, S. (2021). Compression-shear failure properties and acoustic emission (AE) characteristics of rocks in variable angle shear and direct shear tests. *Measurement*, 183, 109814. https://doi.org/10.1016/j.measurement.2021.109814

Hoek, E., & Brown, E. T. (2019). The Hoek–Brown failure criterion and GSI – 2018 edition. *Journal of Rock Mechanics and Geotechnical Engineering*, 11(3), 445–463. https://doi.org/10.1016/j.jrmge.2018.

08.001

Huang, G., Zheng, M., & Peng, J. (2021). Effect of Vegetation Roots on the Threshold of Slope Instability Induced by Rainfall and Runoff. *Geofluids*, 2021(1), 6682113. https://doi.org/10.1155/2021/6682113

Jawil, A. A., & Pontus, A. J. (2023). Analisis Penurunan Muka Tanah (Subsidens) Menggunakan Metode Empirik Di Terowongan Penstock Sta 10+ 150 PLTA Kerinci Merangin, Kabupaten Kerinci, Provinsi Jambi. *Jurnal Teknologi Mineral FT Unmul*, 11(1), 26–33. http://dx.doi.org/10.30872/jtm.v11i1.11455

Khatun, M., Hossain, A. S., Sayem, H. M., Moniruzzaman, M., Ahmed, Z., & Rahaman, K. R. (2023). Landslide susceptibility mapping using weighted-overlay approach in Rangamati, Bangladesh. Earth Systems and Environment, https://doi.org/10.1007/s41748-022-00312-2

Li, D.-Q., Xiao, T., Cao, Z.-J., Phoon, K.-K., & Zhou, C.-B. (2016). Efficient and consistent reliability analysis of soil slope stability using both limit equilibrium analysis and finite element analysis. *Applied Mathematical Modelling*, 40(9), 5216–5229. https://doi.org/10.1016/j.apm.2015.11.044

Liu, Y., Deng, Z., & Wang, X. (2021). The effects of rainfall, soil type and slope on the processes and mechanisms of rainfall-induced shallow landslides. Applied Sciences, 11(24), 11652. https://doi.org/10.3390/app112411652

Loilatu, R., & Iswandaru, I. (2022). Analisis Kestabilan Lereng Andesit Menggunakan Metode FEM pada PT. X. *Jurnal Riset Teknik Pertambangan*, 2(1), 15–23. https://doi.org/10.29313/jrtp.v2i1.782

Nath, S. K., Sengupta, A., & Srivastava, A. (2021). Remote sensing GIS-based landslide susceptibility & risk modeling in Darjeeling–Sikkim Himalaya together with FEM-based slope stability analysis of the terrain. *Natural Hazards*, 108(3), 3271–3304. https://doi.org/10.1007/s11069-021-04823-5

Neamat, S., & Karimi, H. (2020). A systematic review of GIS-based landslide Hazard Mapping on Determinant Factors from International Databases. *2020 international conference on advanced science and engineering (ICOASE)*, 180–183. https://doi.org/10.1109/ICOASE51841.2020.9436611

Pawluszek-Filipiak, K., Oreńczak, N., & Pasternak, M. (2020). Investigating the effect of cross-modeling in landslide susceptibility mapping. *Applied Sciences*, 10(18), 6335. https://doi.org/10.3390/app10186335

Pilecka, E., Szwarkowski, D., Stanisz, J., & Blockus, M. (2022). Analysis of a landslide on a railway track using laser scanning and FEM numerical modelling. *Applied Sciences*, 12(15), 7574. https://doi.org/10.3390/app12157574

PU Regulation No.22 (2007). Kementerian Pekerjaan Umum dan Perumahan Rakyat, Indonesia.

Rawat, P. K., & Pant, B. (2023). Geoenvironmental GIS development to investigate Landslides and Slope Instability along Frontal zone of Central Himalaya. *Natural Hazards Research*, 3(2), 196–204. https://doi.org/10.1016/j.nhres.2023.03.005

Saleem, J., Ahmad, S. S., & Butt, A. (2020). Hazard risk assessment of landslide-prone sub-Himalayan region by employing geospatial modeling approach. *Natural Hazards*, 102(3), 1497–1514. https://doi.org/10.1007/s11069-020-03980-3

Simandjuntak, T. O., Rusmana, E, Suroso, S., & Supandjono, J. B. (2007). *Peta Geologi Lembar Malili*. Pusat Penelitian dan Pengembangan Geologi, Indonesia.

Susilo, A., Fitriah, F., Ayu Rachmawati, E. T., & Suryo, E. A. (2020). Analysis of landslide area of Tulung subdistrict, Ponorogo, Indonesia in 2017 using resistivity method. *Smart and Sustainable Built Environment*, 9(4), 341–360. https://doi.org/10.1108/SASBE-06-2019-0082

Wang, G., Chen, X., & Chen, W. (2020). Spatial prediction of landslide susceptibility based on GIS and discriminant functions. *ISPRS International Journal of Geo-Information*, 9(3), 144. https://doi.org/10.3390/ijgi9030144

Wyllie, D. C, & Mah, C. (2004). *Rock Slope Engineering Civil and Mining*, 4th Edition. CRC Press.

ISSN: 2579-5821 (Print)
ISSN: 2579-5546 (Online)
URL address: http://journal.unhas.ac.id/index.php/geocelebes
DOI: 10.70561/geocelebes.v9i1.43184

Jurnal Geocelebes Vol. 9 No. 1, April 2025, 28 – 42

Microbiological Study of *Escherichia Coli* Contamination in Dug Wells in Demak District, Central Java

Narulita Santi[1]*, Celsy Miftaqul Tiara Fanny[1], Dina Rahayuning Pangestuti[2], Thomas Triadi Putranto[1], Maya Aiko Salsabila Putri[1]

[1]Department of Geological Engineering, Faculty of Engineering, Diponegoro University, 50275, Tembalang, Semarang City, Central Java, Indonesia.
[2]Department of Public Health Nutrition, Faculty of Public Health, Diponegoro University, 50275, Tembalang, Semarang City, Central Java, Indonesia.

*Corresponding author. Email: narulita.santi@live.undip.ac.id

Manuscript received: 10 February 2025; Received in revised form: 10 April 2025; Accepted: 25 April 2025

Abstract

Demak Regency is a peri-urban area in Java experiencing an increasing demand for clean water due to population growth and development. Groundwater is the primary source to meet this demand, although its quality is often threatened by pollution from household waste and unprotected septic tanks. This study aims to evaluate groundwater quality in Demak District with the Escherichia coli presence parameter in unconfined aquifers using a GIS-based spatial approach and IDW interpolation method. The geology of the study area includes sandstone, carbonate mudstone, and alluvium lithologies, with most regions having flat slopes. The hydrogeological potential of the study area shows diverse aquifer productivity, with groundwater levels ranging from 0.3–41 meters. The results of the groundwater quality analysis in the study area showed that 47% of the samples exceeded the safe limit for *Escherichia coli* by Ministry of Health Number 2 Year 2023. The shallow depth of the groundwater table and poor well construction allow the infiltration of contaminants from the land surface into the groundwater, especially from polluting sources around the well. This study provides an essential overview of groundwater quality in the Demak District, which can support sustainable groundwater management and improved sanitation to improve public health.

Keywords: contamination; *Escherichia coli*; groundwater quality; unconfined aquifer.

Citation: Santi, N., Fanny, C. M. T., Pangestuti, D. R., Putranto, T. T., & Putri, M. A. S. (2025). Microbiological Study of *Escherichia Coli* Contamination in Dug Wells in Demak District, Central Java. *Jurnal Geocelebes*, 9(1):28–42, doi: 10.70561/geocelebes.v9i1.43184

Introduction

Demak Regency is one of the peri-urban areas with high population density and intensive agricultural activities, potentially increasing the risk of contamination of groundwater sources (Alifya & Mardiansjah, 2021). Demak's geographical location directly adjacent to Semarang City as an economic center has led to a high population growth rate, reaching an average of 1.09% by 2023. Rapid residential and economic development resulted in a population density of 1,269 people/km² (BPS, 2024), which further increased the demand for clean water, especially from groundwater sources. Problems that are often encountered include groundwater owned by the community that does not meet the criteria for clean and safe water (Rizal & Asyfiradayati, 2024). Water is a vital resource for life, but when contaminated by biological pollutants such as Escherichia coli, viruses, and parasites, it can cause serious health impacts, especially in developing countries that have limited access to clean water and adequate sanitation (Kristanti et.al., 2022). In this case, *E. coli* is an important microbiological indicator for determining water quality, given that its presence often indicates the presence of fecal pollution that can

endanger human health (Rongre et al., 2018). *E. coli* can cause various diseases whose transmission involves contaminated water, such as diarrhea, typhoid, and dysentery, known as waterborne diseases (Priyanto, 2019). The effect of Escherichia coli bacteria can also cause death (Awuy, et, al., 2018). To find out whether the water used contains E-Coli bacteria is not easy, because its size is very small and invisible to the eye (Fauziah, 2021).

Hydrogeological conditions in the northern part of Demak have a shallower groundwater depth compared to the depth of water in the southern part of Demak (Putranto et al, 2021). The quality of groundwater in Demak Regency is uncertain, as many residents still rely on well water as their main source. Many of these wells are located close to pollutant sources, such as toilet waste, household waste, and leaking septic tanks. The non-optimal physical condition of these wells can affect the bacteriological quality of the well water. Previous studies have shown that the suboptimal physical condition of wells also greatly contributes to the decline in groundwater quality, which is an important concern for public health (Syafarida et al., 2022). The bacteriological quality of unqualified dug well water will be higher when compared to qualified dug wells (Dewi et al., 2019). Therefore, it is important to evaluate groundwater quality in community dug wells to provide relevant information for groundwater resource management and public health protection efforts.

Although there have been previous studies on groundwater quality in this area, there has been no specific research on microbiological parameters, such as the presence of *E. coli* Therefore, the use of a Geographic Information System (GIS) based spatial approach and Inverse Distance Weighting (IDW) method is essential to determine the concentration and distribution pattern of *E. coli*. This study aims to identify groundwater quality based on *E. coli* in community-owned unconfined aquifers that are expected to provide recommendations for sustainable groundwater management and microbiological pollution mitigation in Demak Regency.

Materials and Methods

The study area is in the northern part of Java Island, and most of the study area is directly adjacent to the Java Sea. The morphology of this area includes alluvial plains with elevations between 0 and 15 meters, while the southern part has structural hills that reach elevations of 15 to 325 meters. Geologically, this area belongs to the alluvial plains of Northern Java and is within the Bogor – North Serayu – Kendeng Anticlinorium Zone (van Bemmelen, 1949). The stratigraphy of this area is divided into six rock units arranged sequentially from the oldest to the youngest. The rock units are carbonate sandstone unit, carbonate mudstone, carbonate sandstone, carbonate sandstone, sandstone and carbonate mudstone, volcanic breccia unit, and alluvial sediment unit, which dominates almost the entire area of Demak Regency. The alluvial deposits, consisting of sand, gravel, and clay, have highly variable porosity. The flow of water in these alluvial deposits units is highly dependent on the proportion of each material.

Demak District has two cross-municipal groundwater basins, which are CAT Semarang-Demak and CAT Kudus, where the potential availability of groundwater reaches 1,249 million m^3/year (Rifai, 2022). There are two types of aquifers in this region, which are aquifers that flow through intergranular spaces, small productive fissured or nested aquifers, and rare groundwater areas. Intergranular flow aquifers fall into three main categories: high-productivity and widely distributed aquifers, widely distributed productive

aquifers, and widely distributed moderately productive aquifers. High productivity aquifers consist of alluvium material with high porosity and medium to high permeability, allowing significant water flow. These alluvium deposits, present in Demak District, can potentially increase the aquifer's ability to store and transport water.

The relationship between *E. coli* concentrations and aquifer characteristics is essential, as the rocks that make up an aquifer affect its porosity and permeability. Aquifers with high porosity allow for more significant water movement, potentially increasing the risk of contamination by *E. coli*.

The research method is divided into two main stages: collection and processing. The data collection phase was conducted from June 27 to July 3, 2024, and included secondary and primary data obtained directly from the research site through geological and hydrogeological mapping. Geological mapping provided information on the geology and land use data of the investigation area, while hydrogeological mapping provided data on the groundwater table, elevation, groundwater samples, and the results of insitu measurements, including temperature, pH, DHL and TDS. Groundwater samples were taken from unconfined aquifers (community dug wells) to ensure the accuracy of data related to water quality and *E. coli* distribution. Data related to groundwater quality sampling locations in the Demak District are presented in Table 1.

Table 1. Groundwater sample locations for each sub-district

No	Sub-district	Number of Sample Points	Sample Code
1	Karangawen	3	SG 3, SG 38, SG 39
2	Mranggen	5	SG 5, SG 10, SG 11, SG 22, SG 40
3	Guntur	2	SG 26, SG 27
4	Karangtengah	2	SG 9, SG 17
5	Sayung	2	SG 12, SG 23
6	Bonang	2	SG 36, SG 37
7	Demak	2	SG 15, SG 16
8	Wedung	1	SG 20
9	Mijen	1	SG 13
10	Wonosalam	5	SG 14, SG 25, SG 29, SG 30, SG 33
11	Karanganyar	1	SG 35
12	Gajah	1	SG 34
13	Dempet	2	SG 7, SG 32
14	Kebonagung	1	SG 8

Description: Code of Sample Containing *E. coli*

Microbiological testing was conducted at the Testing and Calibration Laboratory to analyze the *E. coli* content in the samples, by the APHA 9221-G standard, 23rd Edition 2017, using the Most Probable Number (APM) method. APM is a statistical method used to estimate the number of microorganisms, such as bacteria, in a sample (Sunarti et al., 2015). In this context, APM/100 ml indicates the number of *E. coli* measured in 100 milliliters of groundwater. The laboratory data obtained was then analyzed using GIS software by applying the IDW interpolation technique, a simple deterministic method that considers a point's value based on surrounding values. The data collected was then analyzed to identify the concentration and distribution pattern of bacteria and the relationship between geological and hydrogeological factors with the presence of these bacteria in the Demak District. The methodological steps applied, from data collection to interpretation of results, can be seen in Figure 1.

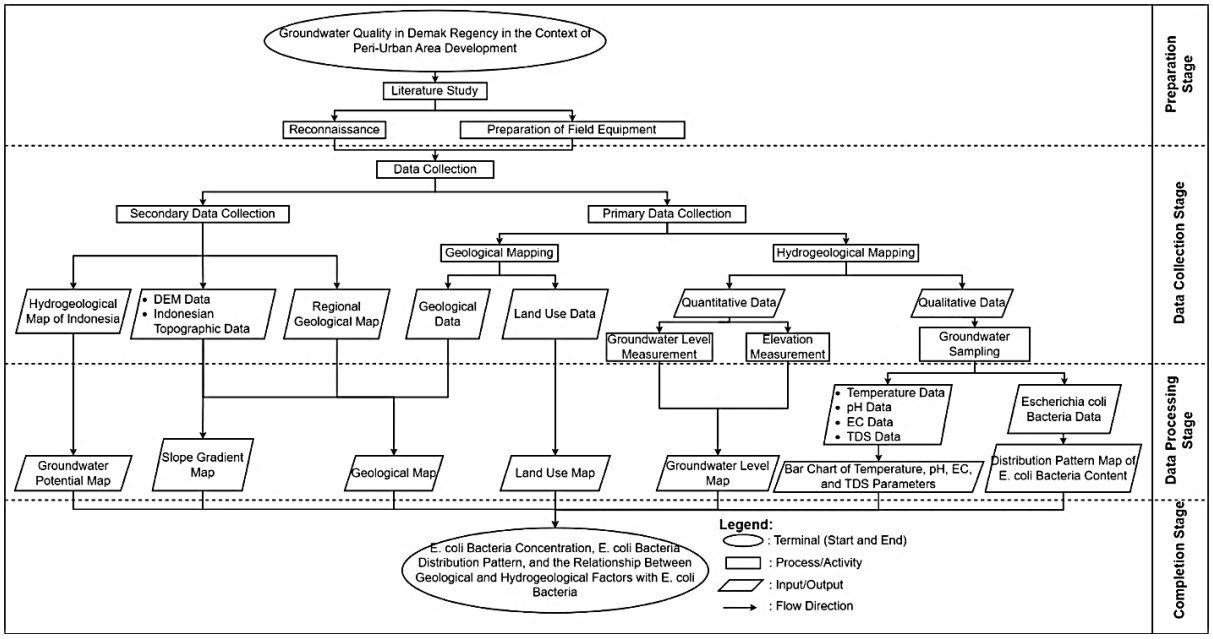

Figure 1. Research flow chart.

Results and Discussion

Groundwater Level Analysis of the Study Area

Based on the results of hydrogeological mapping in the study area, shows the dependence of the community on shallow groundwater sources for daily needs. Visualization of well location points and groundwater flow directions was carried out using GIS applications, which produced an interactive map of the Demak Regency area. The results of the survey of 30 wells showed that the groundwater table elevation varied between 0.24 to 41.17 m, with the highest groundwater table found in Banyumeneng Village, Mranggen Sub-district, and the lowest in Bungo Village, Wedung Sub-district. This difference in elevation causes groundwater flow to move from higher to lower areas, with the direction of groundwater flow in Demak Regency generally moving from south to north, following the topography of the area which slopes to the north (Figure 2).

Analysis of E. coli *Concentration in the Study Area*

The analysis was conducted on 30 dug well points in unconfined aquifers in the study area. The results of this test were compared with the quality standards set in the Minister of Health Regulation No. 2 of 2023. The results show that the concentration of *E. coli* in groundwater varies (Figure 3). The highest value reached 1400 APM/100 ml in sample SG 34. On the other hand, sample points such as SG 8, SG 9, SG 10, SG 14, SG 17, SG 25, SG 26, SG 27, SG 30, SG 33, SG 35, SG 36, SG 37, SG 38, SG 39, and SG 40 showed results of 0 APM/100 ml, indicating the absence of bacterial contamination at these locations. Meanwhile, other samples showed varying concentrations, such as SG 3 with 5 APM/100 ml, SG 5 with 2 APM/100 ml, SG 7 with 9 APM/100 ml, and SG 20, SG 29, and SG 32 with 450 APM/100 ml each.

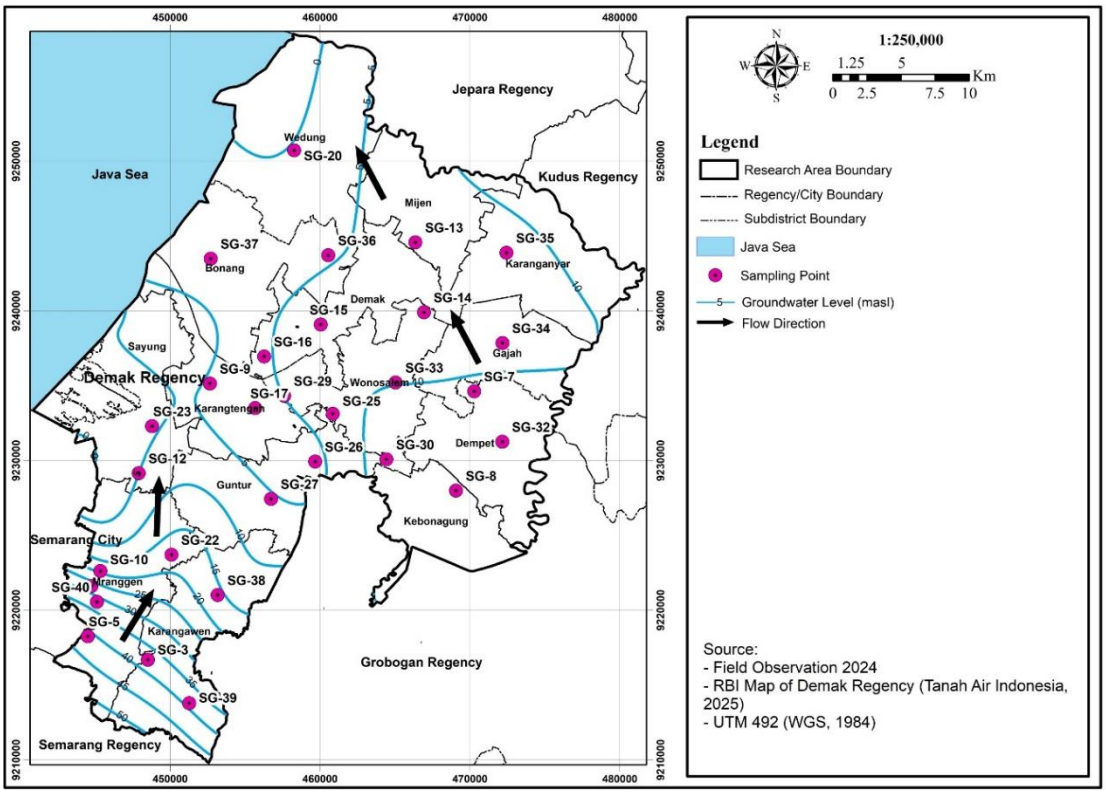

Figure 2. Groundwater table map of the study area.

Based on the quality standard for clean water, the concentration of *E. coli* in 100 ml should not be detected (Ministry of Health, 2023). However, the test results showed that 14 out of 30 sample points in Demak Regency exceeded the permissible limit, indicating potential groundwater pollution from urban activities. High concentrations of *E. coli* are caused by various factors, including the cleanliness of the environment around the well, cracks in the well wall or ring, and too close a proximity between the bathroom, toilet, or septic tank and the well. The physical condition of wells near sources of contamination, such as latrines, livestock pens, damp areas, or garbage dumps, as well as leaks in well construction that allow waste to flow through soil cracks, also increase the risk of contamination (Marsono, 2009). Previous research has also shown that groundwater pollution is often associated with poor sanitation practices and inadequate waste management, which can worsen groundwater quality in urban areas (Rifai, 2022).

Effect of Depth of Groundwater Table on E. coli *Content*

Based on Marlinda et al. (2019), the content of *E. coli* in groundwater is influenced by the variable depth of the groundwater table, where these bacteria tend to be found more often in shallow groundwater layers. This result aligns with the data shown in Figure 4, which shows that most of the groundwater samples containing *E. coli* have a water table depth of less than 15 meters. Data on the depth of the groundwater table in the study area can be seen in Table 3. The depth of the water table is measured vertically from the ground surface to the level where the groundwater is located. Shallow water table depths are more susceptible to bacterial contamination from the ground surface due to their proximity to potential pollution sources, such as septic tanks, domestic waste disposal sites, or livestock pens. The proximity of the water table to the surface allows bacteria and other contaminants from human and animal activities to enter more easily through infiltration or slow groundwater movement at that depth. The

increasing the depth of the water table can reduce *E. coli* concentrations, indicating that deeper soil layers can act as natural filters that reduce bacterial contamination (Marlinda et al., 2019).

Distribution Pattern of E. coli

The selection of sampling points was based on the distribution of land use, geological conditions, and population density. Analysis of *E. coli* concentrations was conducted to identify the bacteria levels at each sampling point and determine the factors influencing these results.

The mapping of the distribution pattern of groundwater quality based on the concentration of *E. coli* in Demak Regency, analyzed using the IDW method, can be seen in Figure 5. Areas with the highest concentrations, marked in red, were found in several sub-districts, such as the Wedung, Sayung, Wonosalam, Gajah, and Dempet sub-districts, at sample points SG 23, SG 20, SG 29, SG 34, and SG 32. The distribution pattern shows that areas around points with high concentrations tend to have more excellent bacterial content, while areas further away from points with high concentrations show a decrease in bacterial content, which is indicated by a gradation of color from red to dark green, where dark green indicates areas with low bacterial concentrations. The color sequence from dark green to red depicts a gradual increase in concentration.

E. coli in groundwater in residential areas can endanger human health, especially if the water is consumed without boiling. The bacteria can produce toxins in contaminated drinking water and cause diarrheal disease, one of the many diseases caused by the poor microbiological quality of drinking water (Sulistiyawati, 2019). Previous studies have shown that factors such as land use, population density, and geological conditions contribute significantly to groundwater contamination by *E. coli* (Marlinda et al., 2019). Therefore, it is essential to ensure drinking water is free from bacterial contamination to prevent health risks.

Based on the research of Jung et al. (2014), microbial contamination of water often comes from human-associated feces (wastewater treatment plants, combined sewage overflows (CSOs), non-collective sewage systems), domestic animals (manure spreading, manure overflows).

Observations of 30 dug wells in Demak Regency show that the wells are in unconfined aquifers and are utilized by the community for various daily needs, such as bathing, cooking, drinking, washing clothes, washing household appliances, as well as watering plants and washing vehicles. The characteristics of the dug wells studied in relation to potential sources of pollutants in the vicinity, such as the distance between the well and the septic tank, the distance between the well and the source of waste, the condition of the well floor, as well as the distance between landfills and cattle pens, are described in Table 2. In the context of health, dug wells that meet standards must have certain characteristics, including strong well walls or rings, impermeable floors, adequate well lips, effective wastewater disposal channels, and well covers to avoid direct contamination (Mudatsir, 2020). The difference in *E. coli* content between wells SG 34 and SG 40, despite having similar environmental parameters, is likely influenced by several factors that determine the level of bacterial contamination. One such factor is the physical condition of the well in SG 34, potential leaks in the well walls or a poorly sealed cover may increase the risk of contaminant ingress from the surface. The closer proximity of SG 34 to septic tanks and cattle pens compared to SG 40 also contributes to greater potential for contamination. The cattle pens around SG 34 are larger in scale compared to those around SG 40, which could lead to higher levels of contamination.

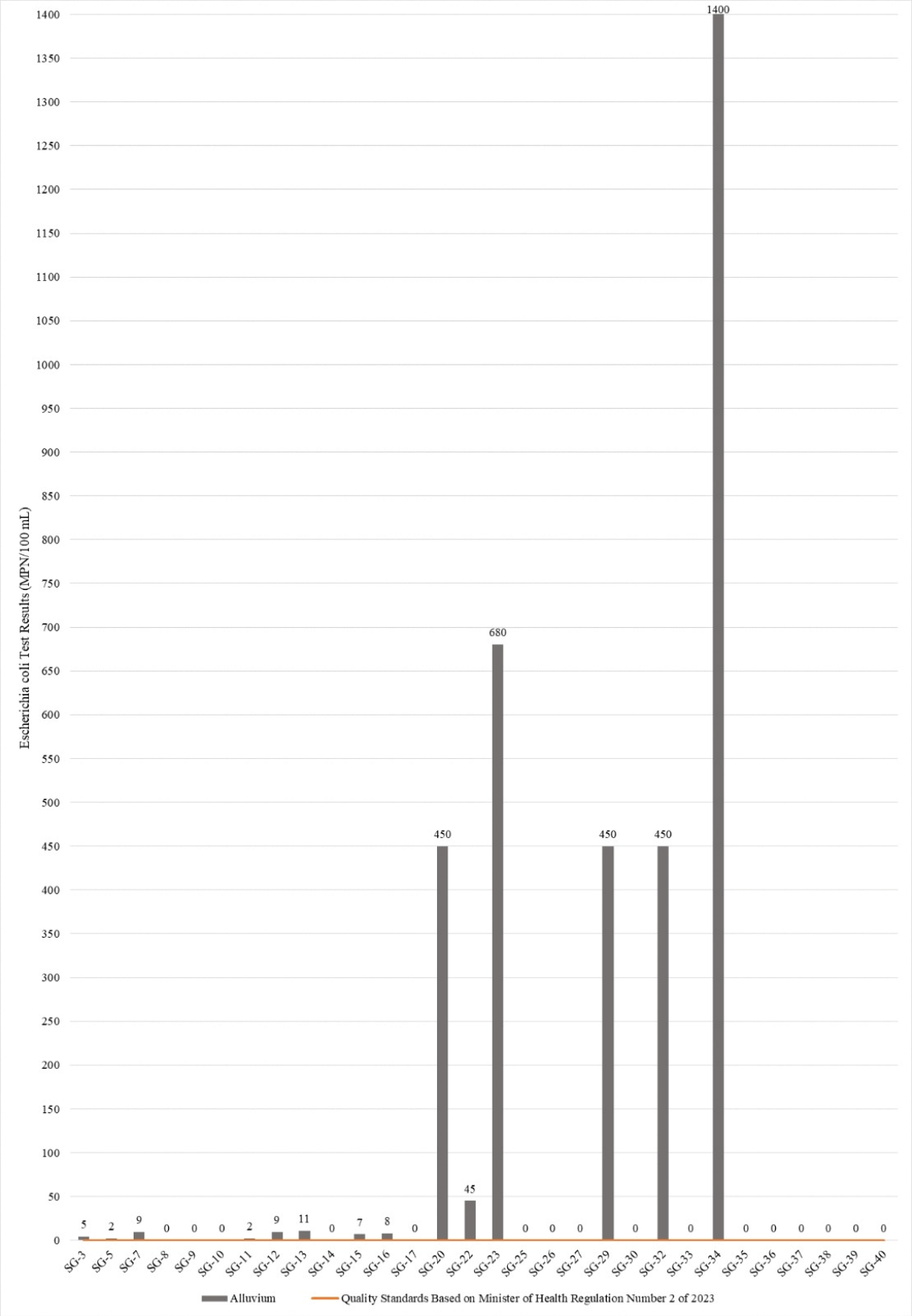

Figure 3. Concentration of *E. coli* in Groundwater in Demak Regency (n=30)

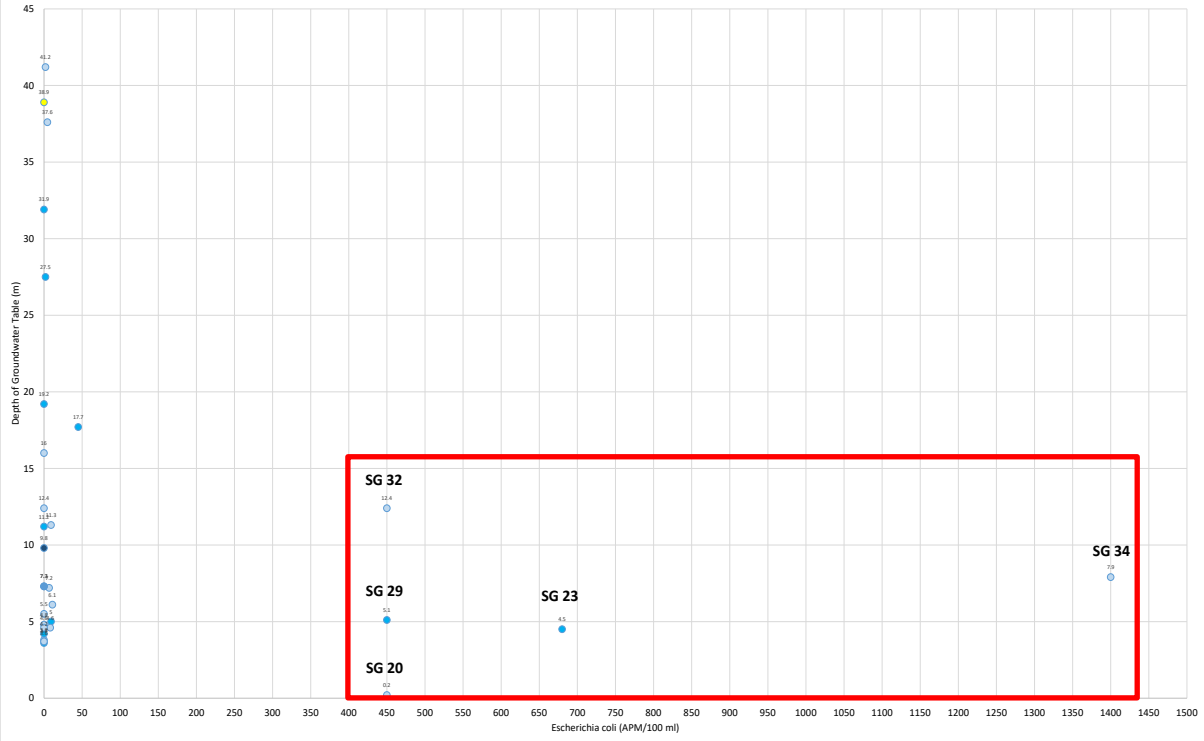

Figure 4. The relations between *E. coli* concentration and Depth of Groundwater Table in the study area.

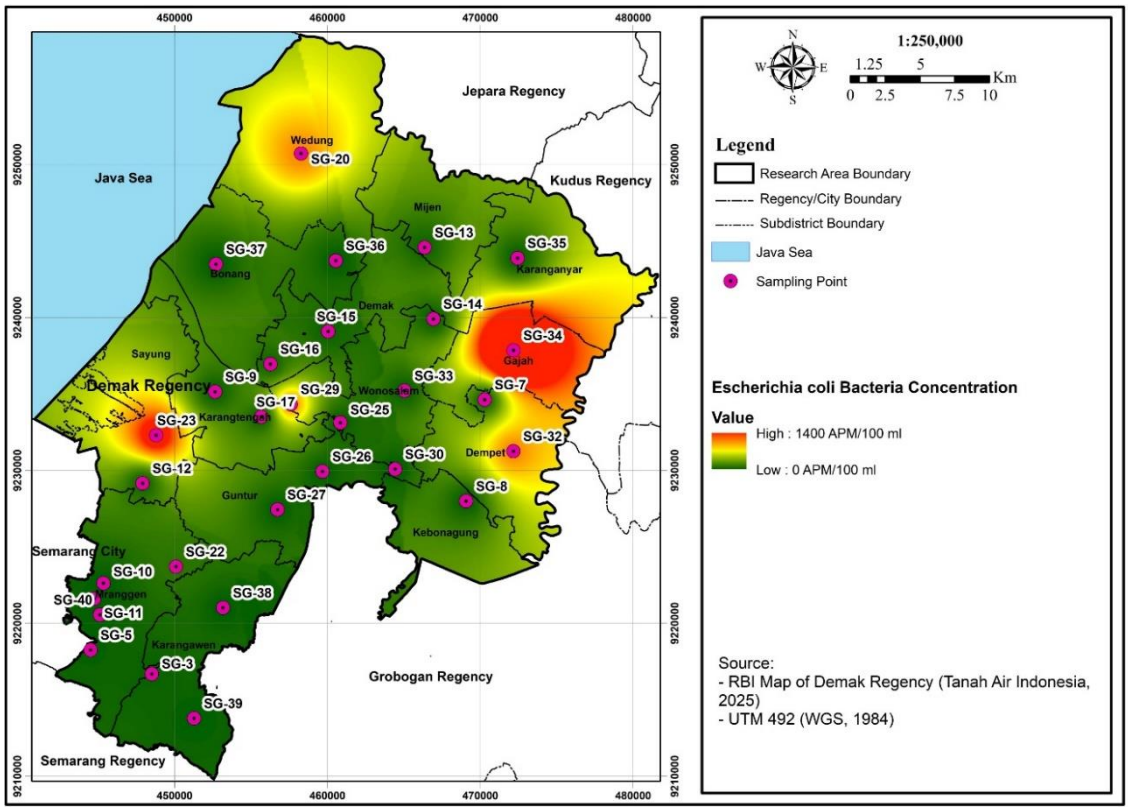

Figure 5. Map of the distribution pattern of *E. coli* in the study area.

There is a significant relationship between septic tank wastewater management systems and *E. coli* content which has an impact on the quality of dug well water (Achmad et al., 2020).

From the mapping results (Table 3), the SG 34 sampling point in the Gajah sub-district recorded the highest 1400 APM/100 ml concentration, indicating that this location was seriously polluted. Physical

observations showed that SG 34 did not meet well construction standards, such as the absence of strong walls, impermeable floor, and well cover. The well's proximity to septic tanks and livestock pens (less than 10 m) exacerbates the contamination, as the groundwater around the well is potentially exposed to fecal bacteria from both humans and animals. Sampling point SG 20, which recorded a bacteria concentration of 450 APM/100 ml, also showed a similar pattern. This well is located close to a garbage dump and chicken slaughterhouse, which are potential sources of bacteria and pollutants. Inadequate environmental hygiene conditions around this well facilitated the increase in the concentration of pathogenic microorganisms in the groundwater. On the other hand, sampling point SG 5 with a concentration of 2 APM/100 ml shows that the unsafe distance between the well and septic tank (less than 10 m) still has the potential to trigger contamination, albeit at a lower level. Several other sampling points also showed a significant correlation between the physical quality of the well and bacterial contamination. For example, sampling point SG 11 had high bacterial concentrations because household waste was discharged directly into the river, less than 10m from the well. This indicates that improper waste disposal practices worsen groundwater quality. Sampling point SG 29 had a contamination of 450 APM/100 ml, which could be attributed to the poor physical condition of the well, such as the absence of well walls and impermeable floor, making the groundwater vulnerable to exposure to bacteria from external sources.

Table 2. Observation results of sampling points in Demak Regency

No	Pollutant Source	Eligible	Not Eligible	Eligible (%)	Not Eligible (%)
1	Septic tank distance >10 m	21	9	70	30
2	Distance with sewage >10 m	19	11	63.33	36.67
3	Physical condition well	12	18	40	60
4	Distance to trash can >10 m	27	3	90	10
5	Distance with to livesrock pens >10 m	28	2	93.33	6.67

Table 3. Complete description of the condition of the observation well.

Sample Code	*E- coli* (APM/100 ml)	Lithology	Land Use	Depth of Groundwater Table (m)	Groundwater Potential
SG 3	4.5	Alluvium	Residential Area	37.6	Moderately productive aquifer, with wide distribution
SG 5	2	Alluvium	Residential Area	41.2	Moderately productive aquifer, with wide distribution
SG 7	9.3	Alluvium	Residential Area	11.3	Moderately productive aquifer, with wide distribution
SG 8	0	Alluvium	Residential Area	11.2	Productive aquifer with wide distribution
SG 9	0	Alluvium	Residential Area	4.8	Moderately productive aquifer, with wide distribution
SG 10	0	Alluvium	Residential Area	19.2	Productive aquifer with wide distribution
SG 11	2	Alluvium	Residential Area	27.5	Productive aquifer with wide distribution
SG 12	9.3	Alluvium	Residential Area	5	Productive aquifer with wide distribution
SG 13	11	Alluvium	Residential Area	6.1	Moderately productive aquifer, with wide distribution

Sample Code	*E- coli* (APM/100 ml)	Lithology	Land Use	Depth of Groundwater Table (m)	Groundwater Potential
SG 14	0	Alluvium	Residential Area	3.8	Moderately productive aquifer, with wide distribution
SG 15	6.8	Alluvium	Residential Area	7.2	Moderately productive aquifer, with wide distribution
SG 16	8.22	Alluvium	Residential Area	4.6	Moderately productive aquifer, with wide distribution
SG 17	0	Alluvium	Residential Area	3.6	Productive aquifer with wide distribution
SG 20	450	Alluvium	Residential Area	0.2	Moderately productive aquifer, with wide distribution
SG 22	45	Alluvium	Residential Area	17.7	Productive aquifer with wide distribution
SG 23	680	Alluvium	Residential Area	4.5	Productive aquifer with wide distribution
SG 25	0	Alluvium	Residential Area	7.3	Highly productive aquifer, with wide distribution
SG 26	0	Alluvium	Residential Area	4.2	Productive aquifer with wide distribution
SG 27	0	Alluvium	Residential Area	5.5	Moderately productive aquifer, with wide distribution
SG 29	450	Alluvium	Residential Area	5.1	Productive aquifer with wide distribution
SG 30	0	Alluvium	Residential Area	12.4	Highly productive aquifer, with wide distribution
SG 32	450	Alluvium	Residential Area	12.4	Moderately productive aquifer, with wide distribution
SG 33	0	Alluvium	Residential Area	9.8	Highly productive aquifer, with wide distribution
SG 34	1400	Alluvium	Residential Area	7.9	Moderately productive aquifer, with wide distribution
SG 35	0	Alluvium	Residential Area	7.3	Productive aquifer with wide distribution
SG 36	0	Alluvium	Residential Area	4.6	Moderately productive aquifer, with wide distribution
SG 37	0	Alluvium	Residential Area	3.7	Moderately productive aquifer, with wide distribution
SG 38	0	Alluvium	Residential Area	16	Moderately productive aquifer, with wide distribution
SG 39	0	Carbonate sandstone interbedded with siltstone	Residential Area	38.9	Groundwater scarce areas
SG 40	0	Alluvium	Residential Area	31.9	Productive aquifer with wide distribution

Overall, the results of this analysis show that the physical quality and location of wells have a significant impact on *E. coli* concentrations in groundwater. Wells with

inadequate construction and near pollutant sources, such as septic tanks, livestock pens, or landfills, tended to show high bacterial concentrations. According to Widiyanti (2019), also stated that contamination of well water by *E. Coli* bacteria is related to pollutant sources such as septic tanks, the distance between wells and pollutant sources, landfills, and inadequate sanitation facilities. In the study by Rahman et al (2021), it is also stated that it is important to emphasize water quality monitoring and adequate hygiene practices to improve public health outcomes. Therefore, improved sanitation infrastructure, improved well construction, and community education on well maintenance and waste management practices are necessary to maintain groundwater quality.

Distribution Point Analysis of E. coli *Concentration*

Based on the A-B cross-section conducted with an incision from point A to point B, as seen in Figure 6 and Figure 7, the lithology along the cross-section shows an alluvium layer. This incision cuts through three test wells: SG 25, SG 33, and SG 34. Test results showed that wells SG 25 and SG 33 did not contain *E. coli*, despite having shallow water table depths. This indicates that the existing conditions in wells SG 25 and SG 33 meet sanitary requirements. In addition, well SG 35 has a high Electrical Conductivity (DHL) value, generally containing more mineral ions, such as sodium, calcium, or magnesium. Increased levels of these ions can increase the osmotic pressure of the environment, which in turn creates stress on bacterial cells, inhibiting their cellular activity or even causing death. Inorganic ions or metals in high concentrations in water with high DHL can also have antimicrobial effects, directly inhibiting or limiting the growth of *E. coli* (Arivo & Annissatussholeha, 2017). In contrast, SG 34 showed a very high *E. coli* content, reaching 1400 APM/100 ml. This high bacterial content is most likely due to the groundwater table being less than 15 m deep and the existing condition of the well not meeting sanitary standards. The shallow depth of the water table and poor well construction allow for infiltration of contaminants from the land surface into the groundwater, especially from polluting sources in the vicinity of the well. The low DHL value in SG 34 indicates that this well contains a lesser number of dissolved ions, resulting in a lower osmotic pressure. These conditions create a more conducive environment for bacterial growth, allowing *E. coli* to survive and thrive better as they do not face inhibition from inhibitory ions or high osmotic stress.

The results of the A-B cross-section analysis show that the lithology of the area consists of alluvium layers with different well characteristics. Wells SG 25 and SG 33 were not contaminated with *E. coli*, indicating good sanitation standards. The high electrical conductivity (DHL) values in these two wells created high osmotic pressure, which inhibited bacterial growth. In contrast, well SG 34 had a very high *E. coli* content. This was influenced by the shallow water table, low DHL values and poor sanitary conditions, which allowed infiltration of contaminants from the soil surface. According to Murray et al. (2018), it is necessary to emphasize the education of dug well owners regarding testing and maintaining well quality for public health. This conclusion confirms the importance of maintaining sanitation, DHL values, and managing the depth of the groundwater table to prevent bacterial contamination.

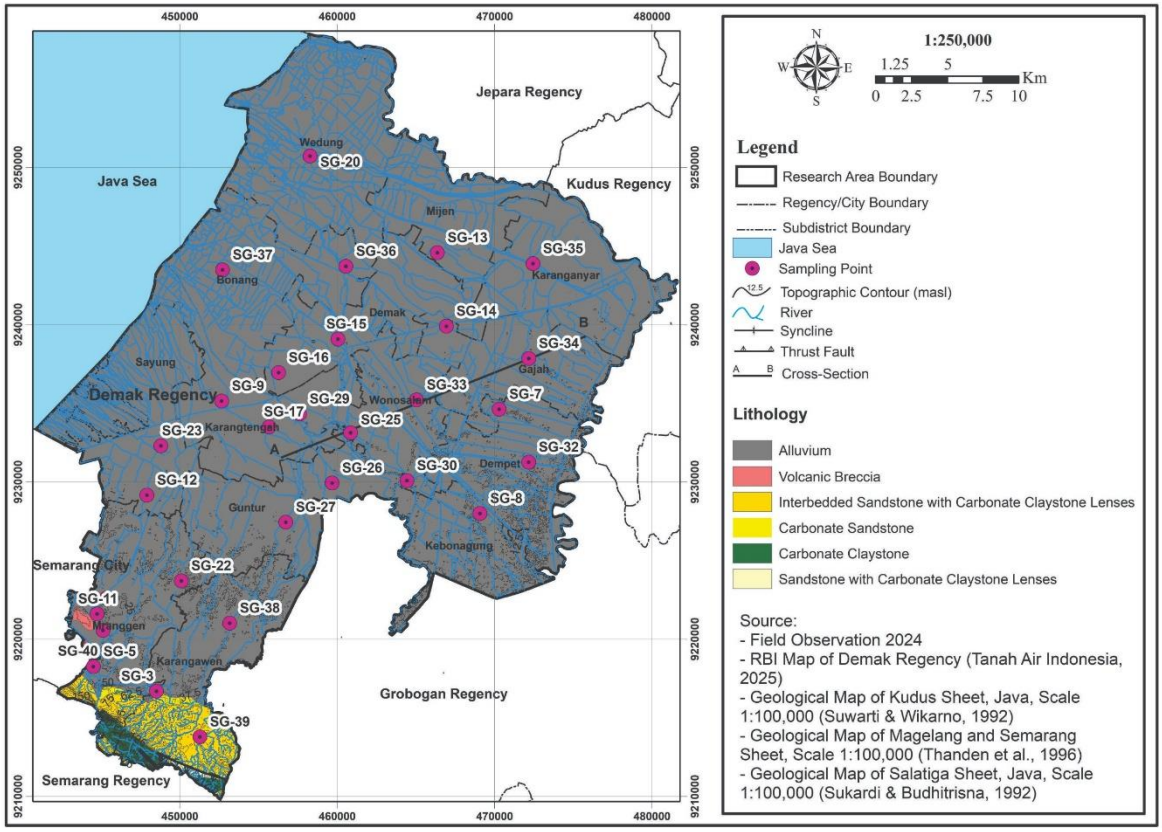

Figure 6. Cross-sectional incision map of the study area.

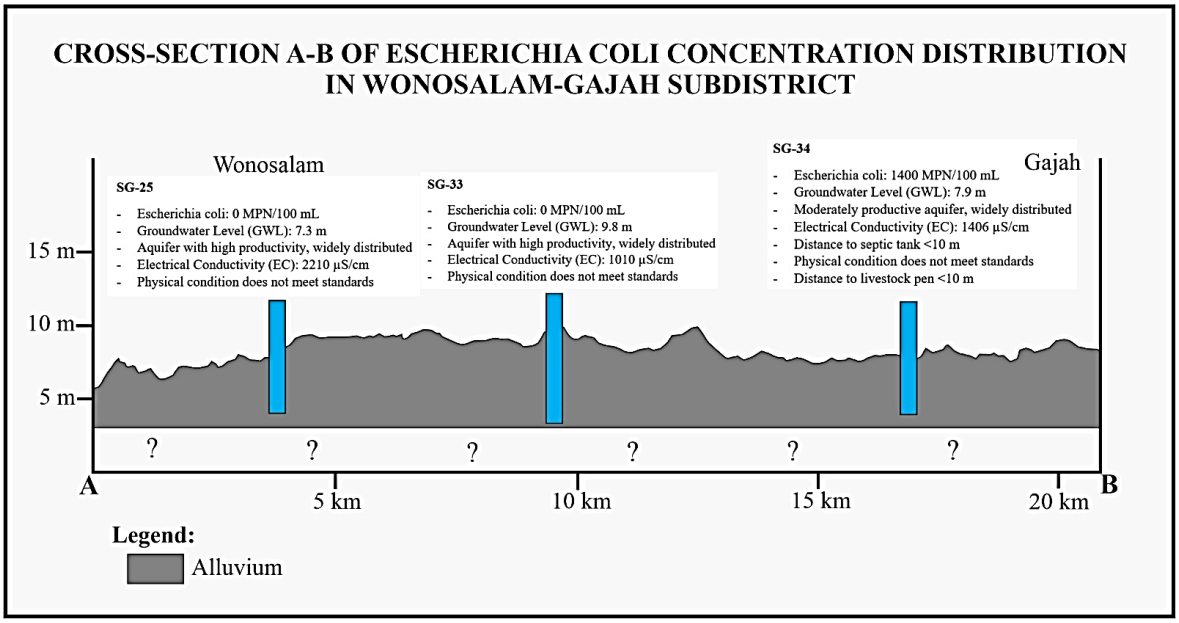

Figure 7. Cross-section of *E. coli* distribution points in the study area.

Conclusion

Based on the results of the research conducted, it can be concluded that the study area has diverse geological conditions, including carbonate sandstone, carbonate mudstone, volcanic breccia, and alluvium. Groundwater potential in the area indicates the presence of aquifers with high productivity and wide distribution, as well as aquifers with medium to small local productivity. The groundwater table varies from 0.24 to 41.17 meters, with flow patterns leading from south to north. *E. coli* concentrations in the Demak area also varied, with the highest value reaching

1400 APM/100 ml in sample SG 34, while sample points SG 8 to SG 40 showed results of 0 APM/100 ml, indicating no contamination. Other samples showed varying concentrations, such as SG 3 with 5 APM/100 ml and SG 20 with 450 APM/100 ml. Most of the dug wells contaminated with *E. coli* have shallow groundwater tables and are in aquifers with extensive productivity, and the existing conditions of the wells that do not meet the requirements further exacerbate the level of contamination. These findings indicate the importance of sanitation management and groundwater quality monitoring to prevent bacterial contamination in the study area.

Acknowledgements

The authors would like to express their deepest gratitude to all those who have contributed to this research. Special thanks go to the advisors who have provided valuable guidance and direction. The authors are also grateful to the financial supporters who have made this research possible, especially the RKAT of the Faculty of Engineering, Diponegoro University, which has supported the implementation and funding of the research. In addition, the authors would like to thank the Professors at Diponegoro University for the data provided, as well as the editors, reviewers, and proofreaders who have provided valuable input for the improvement of this manuscript. Thanks also go to the technicians who helped set up the equipment, as well as all those involved in the field survey, who contributed directly to the data collection.

Author Contribution

Each team member had an important contribution to this research. Authors 2 and 5 conceived and designed the experiments, as well as conducted dug well water sampling and laboratory analysis to identify the presence of Escherichia coli. Authors 1, 3 and 4 analyzed the data and compiled the report supporting the conclusions of this study in Demak District, Central Java.

Conflict of Interest

The authors declare that there is no conflict of interest in this research.

References

Achmad, B. K., Jayadipraja, E. A., & Sunarsih, S. (2020). Hubungan Sistem Pengelolaan (Konstruksi) Air Limbah Tangki Septik dengan Kandungan *Escherichia coli* terhadapat Kualitas Air Sumur Gali. *Jurnal Keperawatan & Kesehatan Masyarakat Cendekia Utama*, 9(1), 24–36. https://doi.org/10.31596/jcu.v9i1.512

Alifya, S. N., & Mardiansjah, F. H. (2021). Transformasi Wilayah Kabupaten Demak Sebagai Kawasan Pinggiran di dalam Proses Metropolitanisasi Semarang. *Jurnal Wilayah dan Lingkungan*, 9(2), 109–126. https://doi.org/10.14710/jwl.9.2.109-126

Arivo, D., & Annissatussholeha, N. (2017). Pengaruh Tekanan Osmotik PH, dan Suhu Terhadap Pertumbuhan Bakteri *Escherichia Coli*. *Jurnal Ilmu Kedokteran dan Kesehatan*, 4(3), 153–160. https://ejurnalmalahayati.ac.id/index.php/kesehatan/article/view/1311

Awuy, S. C., Sumampouw, O. J. & Boky, H. B. (2018). Kandungan *Escherichia Coli* pada Air Sumur Gali dan Jarak Sumur dengan Septic Tank di Kelurahan Rap-Rap Kabupaten Minahasa Utara Tahun 2018. *KESMAS: Jurnal Kesehatan Masyarakat Universitas Sam Ratulangi*, 7(4). https://ejournal.unsrat.ac.id/index.php/kesmas/article/view/23138

BPS. (2024). *Demak Regency in Figures 2024*. https://demakkab.bps.go.id/en/publication/2024/02/28/0a23b78977c3997ab86da46f/kabupaten-demak-dalam-

angka-2024.html

Dewi, P. N., Darundiati, Y. H., & Setiani, O. (2019). Hubungan Sanitasi Lingkungan dan Bakteriologis Air Sumur Gali dengan Kejadian Diare di Kelurahan Genuksari Kecamatan Genuk Kota Semarang. *Jurnal Kesehatan Masyarakat*, 7(4), 187–194. https://ejournal3.undip.ac.id/index.php/jkm/article/view/24365

Fauziah, R. (2021). Expert System Application to Diagnose *Escherichia Coli* (*E-Coli*) Bacteria in Refilled Drinking Water using the Certainty Factor Method. *Infokum*, 9(2), 159–164. http://seaninstitute.org/infor/index.php/infokum/article/view/107

Jung, A.-V., Le Cann, P., Roig, B., Thomas, O., Baurès, E., & Thomas, M.-F. (2014). Microbial Contamination Detection in Water Resources: Interest of Current Optical Methods, Trends and Needs in the Context of Climate Change. *International Journal of Environmental Research and Public Health*, 11(4), 4292–4310. https://doi.org/10.3390/ijerph110404292

Kristanti, R.A., Hadibarata, T., Syafrudin, M., Yilmaz, M., & Abdullah, S. (2022). Microbiological Contaminants in Drinking Water: Current Status and Challenges. *Water, Air, & Soil Pollution*, 233, 299. https://doi.org/10.1007/s11270-022-05698-3

Marlinda, M., Moelyaningrum, A. D., & Ellyke, E. (2019). Keberadaan Bakteri Eschericia Coli dan Coliform pada Sumur Gali dan Bor Rumah Pemotongan Hewan. *Jurnal Kesehatan Lingkungan Jurnal dan Aplikasi Teknik Kesehatan Lingkungan*, 16(1), 679–688.

Marsono. (2009). *Faktor-Faktor yang Berhubungan dengan Kualitas Bakteriologis Air Sumur Gali di Permukiman Studi di Desa Karanganom, Kecamatan Klaten Utara, Kabupaten Klaten*. Universitas Diponegoro.

Ministry of Energy and Mineral Resources. (2017). *Regulation of the Minister of Energy and Mineral Resources of the Republic of Indonesia Number 2 Year 2017 on Groundwater Basins in Indonesia*. Ministry of Energy and Mineral Resources.

Ministry of Health. (2023). *Permenkes No. 2 Year 2023*. Ministry of Health of the Republic of Indonesia.

Mudatsir. (2020). Uji Mikrobiologi Air Sumur Gali Berdasarkan Sumber Pencemar di Desa Limphok dan Beurabung Kecamatan Darussalam, Aceh Besar. *Jurnal Kedokteran Syiah Kuala*, 20(1), 9–18. https://doi.org/10.24815/jks.v20i1.3660

Murray, R. T., Rosenberg Goldstein, R. E., Maring, E. F., Pee, D. G., Aspinwall, K., Wilson, S. M., & Sapkota, A. R. (2018). Prevalence of Microbiological and Chemical Contaminants in Private Drinking Water Wells in Maryland, USA. *International Journal of Environmental Research and Public Health*, 15(8), 1686. https://doi.org/10.3390/ijerph15081686

Putranto, T. T., Susanto, N., & Pangestuti, D. R. (2021). Groundwater quality of unconfined aquifer in Demak Regency. *Indonesia. Journal of Physics: Conference Series*, 1943(1), 012002. https://doi.org/10.1088/1742-6596/1943/1/012002

Priyanto, D. (2019). Peran Air dalam Penyebaran Penyakit. *Balaba: Jurnal Litbang Pengendalian Penyakit Bersumber Binatang Banjarnegara*, 7(1), 27–28.

Rahman, M. M., Kunwar, S. B., & Bohara, A. K. (2021). The interconnection between water quality level and health status: An analysis of *Escherichia coli* contamination and drinking water from Nepal. *Water Resources and*

Economics, 34, 100179. https://doi.org/10.1016/j.wre.2021.100179

Rifai, M. (2022). *Pengelolaan Terhadap Pemanfaatan Air Tanah di Kabupaten Demak*. Matriks Teknik Sipil, 10(1), 1–7. https://doi.org/10.20961/mateksi.v10i1.50094.

Rizal, A. M., & Asyfiradayati, R. (2024). Differences in the reduction of coliform bacteria and *Escherichia coli* with the chlorine diffuser method combined with silica sand in clean water. *Science Midwifery*, 12(3), 1193–1199. https://midwifery.iocspublisher.org/index.php/midwifery/article/view/1632

Rongre, A. J. P., Joseph, W. B. S., & Pinontoan, O. R. (2018). Kandungan *Escherichia coli* dan Kondisi Fisik Sumur Gali di Kelurahan Kakaskasen III Lingkungan III Kecamatan Tomohon Utara Kota Tomohon. *KESMAS: Jurnal Kesehatan Masyarakat Universitas Sam Ratulangi*, 7(4). https://ejournal.unsrat.ac.id/index.php/kesmas/article/view/23181

Sulistiyawati, I. (2019). Kuantitas Total Bakteri Coliform pada Instalasi Pengolahan Limbah Cair Medis Laboratorium Klinik. *Jurnal Ilmiah Universitas Batanghari Jambi*, 19(3), 675–677. https://doi.org/10.33087/jiubj.v19i3.718

Sunarti, R. N. (2015). Uji Kualitas Air Sumur Dengan Menggunakan Metode MPN (*Most Probable Numbers*). *Bioilmi: Jurnal Pendidikan Biologi*, 1(1), 30–34. https://doi.org/10.19109/bioilmi.v1i1.1128

Syafarida, U. Y., Jati, D. R., & Sulastri, A. (2022). Analisis Hubungan Konstruksi Sumur Gali dan Sanitasi Lingkungan Terhadap Jumlah Bakteri Coliform Dalam Air Sumur Gali (Studi Kasus: Desa PAL IX, Kecamatan Sungai Kakap). *Jurnal Ilmu Lingkungan*, 20(3), 437–444. https://doi.org/10.14710/jil.20.3.437-444

van Bemmelen, R. W. (1949). *The Geology of Indonesia*. Martinus Nyhoff, Netherland: The Haque.

Widiyanti, B.L. (2019). Studi Kandungan Bakteri *E.Coli* pada Airtanah (*Confined Aquifer*) di Permukiman Padat Penduduk Desa Dasan Lekong, Kecamatan Sukamulia. *Journal of Geography Science and Education Studies*, 3(1), 1–12. https://doi.org/10.29408/geodika.v3i1.1471

ISSN: 2579-5821 (Print)
ISSN: 2579-5546 (Online)
URL address: http://journal.unhas.ac.id/index.php/geocelebes
DOI: 10.70561/geocelebes.v9i1.34399

Jurnal Geocelebes Vol. 9 No. 1, April 2025, 43 – 58

Predicting the Distribution of CO_2 Impurities in Hydrocarbons: Seismic Reservoir Characterization in the Northern South Sumatera Basin

Ricky Rahmawati[1], Wahidah[1]*, M. Noor Alamsyah[2], Dadan Hamdani[1], Andi Alamsyah[1]

[1]Geofisika, Universitas Mulawarman, Samarinda 75123, Indonesia.
[2]Geofisika, PetroChina International Jabung, DKI Jakarta 12940, Indonesia.

*Corresponding author. Email: wahidah@fmipa.unmul.ac.id

Manuscript received: 31 March 2024; Received in revised form: 14 April 2025; Accepted: 25 April 2025

Abstract

An oil and gas field containing less than 50% carbon dioxide (CO_2) impurities is considered economically viable. This study focuses on the 'X' area, located in the northern part of the South Sumatra Basin, and evaluates the sensitivity of elastic parameters—specifically P-impedance and Vp/Vs ratio—to hydrocarbon presence. Additionally, the study assesses the distribution of sandstone reservoirs within the Lower Talang Akar Formation (LTAF) using seismic reservoir characterization methods, while also analyzing the spatial correlation of natural CO_2 impurities. Using data from 11 wells equipped with S-wave logs, a multi-attribute analysis was applied to predict reservoir properties in 57 additional wells. Sensitivity analysis of hydrocarbons, reservoir, and non-reservoir zones was then conducted using elastic log parameters. Seismic attributes such as variance and ant tracking were utilized to detect fault patterns and potential fractures. Moreover, Relative Acoustic Impedance maps—based on negative and minimum amplitude summations—were generated to visualize sandstone reservoir distribution and CO_2 impurity saturation derived from well tests. Results show that hydrocarbons exhibit greater sensitivity to the Vp/Vs ratio than to P-impedance, although sandstone reservoirs generally display low P-impedance values. Faults in the LTAF surface trend north-south, northwest-southeast, and northeast-southwest, with the highest density in the eastern region of area 'X'. Thick sandstone reservoirs are predominantly found in the northern, southern, western, and southeastern sectors. CO_2 saturation trends decrease westward, aligning with reservoir presence and fracture intensity. Zones with thick reservoirs and low CO_2 levels are identified as key targets for future exploration and development.

Keywords: Multiatribute; P-impedance; Seismic Attributes; South Sumatera Basin; Vp/Vs ratio.

Citation: Rahmawati, R., Wahidah, W., Alamsyah, M. N., Hamdani, D., & Alamsyah, A. (2025). Predicting The Distribution of CO_2 Impurities in Hydrocarbons: Seismic Reservoir Characterization in the Northern South Sumatera Basin. *Jurnal Geocelebes* 9(1):43–58, doi: 10.70561/geocelebes.v9i1.34399

Introduction

Hydrocarbons from well drilling typically contain impurities, one of which is carbon dioxide (CO_2). These impurities affect the economic viability of an oil and gas field (Hidayat et al., 2020). Sembiring et al. (2019) explain that high CO_2 content reduces hydrocarbons' quality and calorific value and that Indonesian gas wells often exhibit very high CO_2 concentrations in natural gas. Variations in CO_2 saturation levels within hydrocarbon gases have been documented across the South Sumatra Basin (Alamsyah et al., 2023). Fields with CO_2 impurity levels exceeding 50% are often reconsidered or even discontinued for further development.

The 'X' area, situated in the northern part of the South Sumatra Basin (Figure 1), produces gas saturated with CO_2. Over 60 wells have been drilled to date, penetrating the main producing reservoir, a CO_2-saturated gas sandstone reservoir located within the Lower Talang Akar Formation (LTAF). The syn-rift LTAF reservoir, deposited during the initial basin development phase, consists of alluvial and fluvial deposits that transitioned to deltaic

deposits due to transgression (Figure 2-rigth). The sediment model, reservoir characteristics, and geometry of the LTAF (Figure 2-left) are influenced by fault movement, distribution patterns, and basin slope.

Reservoir characterization, a crucial aspect in understanding reservoir properties and detecting its distribution (Ambarsari et al., 2020), is a key player in field development. This study focuses on identifying rock elasticity parameters, P-impedance, and Vp/Vs ratio, which are sensitive in identifying hydrocarbons, reservoirs, and non-reservoirs. It also aims to qualitatively assess fault and fracture distribution and intensity using seismic data, determine reservoir distribution qualitatively integrated with CO_2 impurity distribution, and identify economically viable prospective areas for further development.

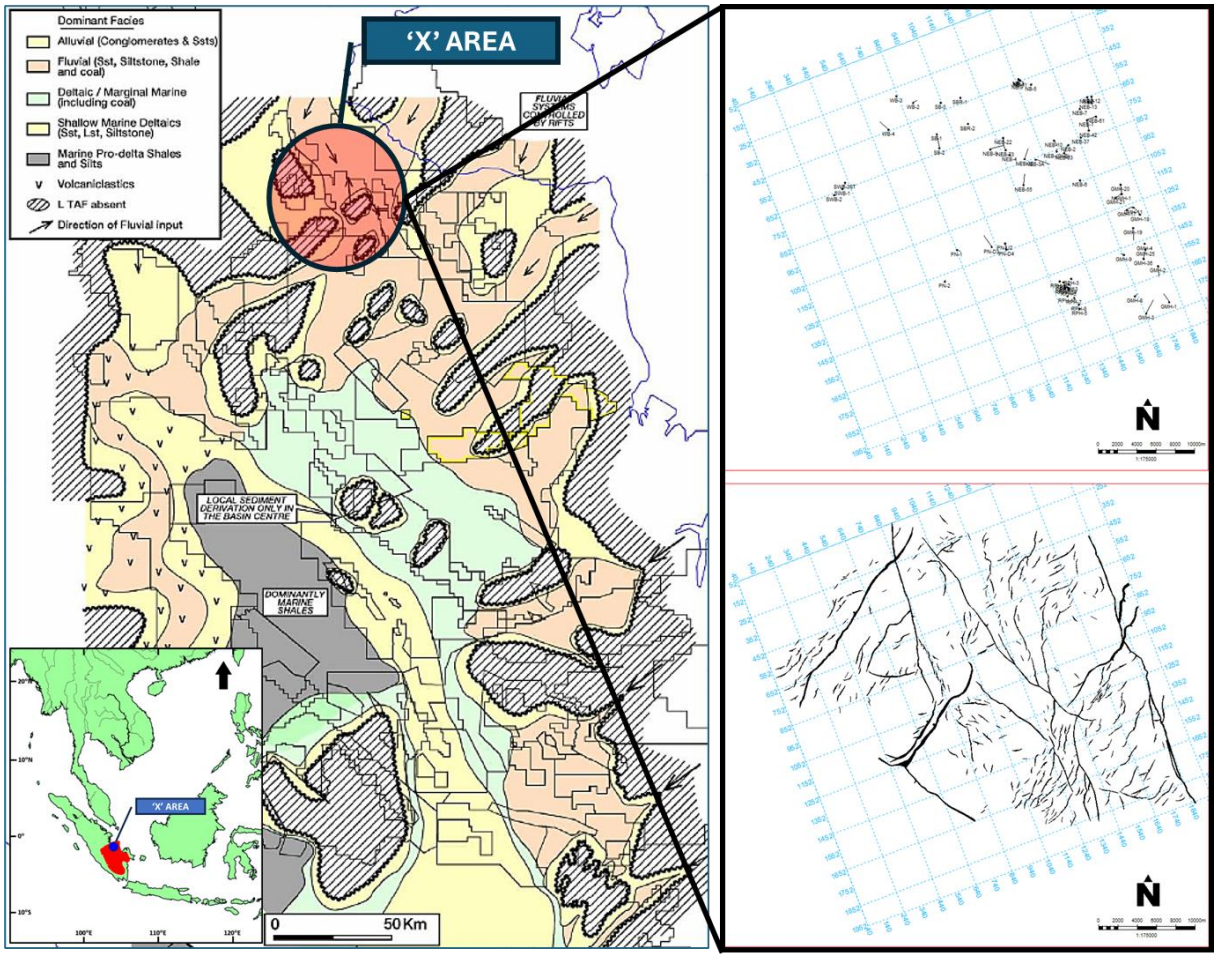

Figure 1. The 'X' area, situated in the northern part of the South Sumatra Basin overlaid with paleogeography of LTAF (Modified from Ginger & Fielding, 2005). Left, 3D Seismic Basemap with well location and fault configuration on LTAF, X Area

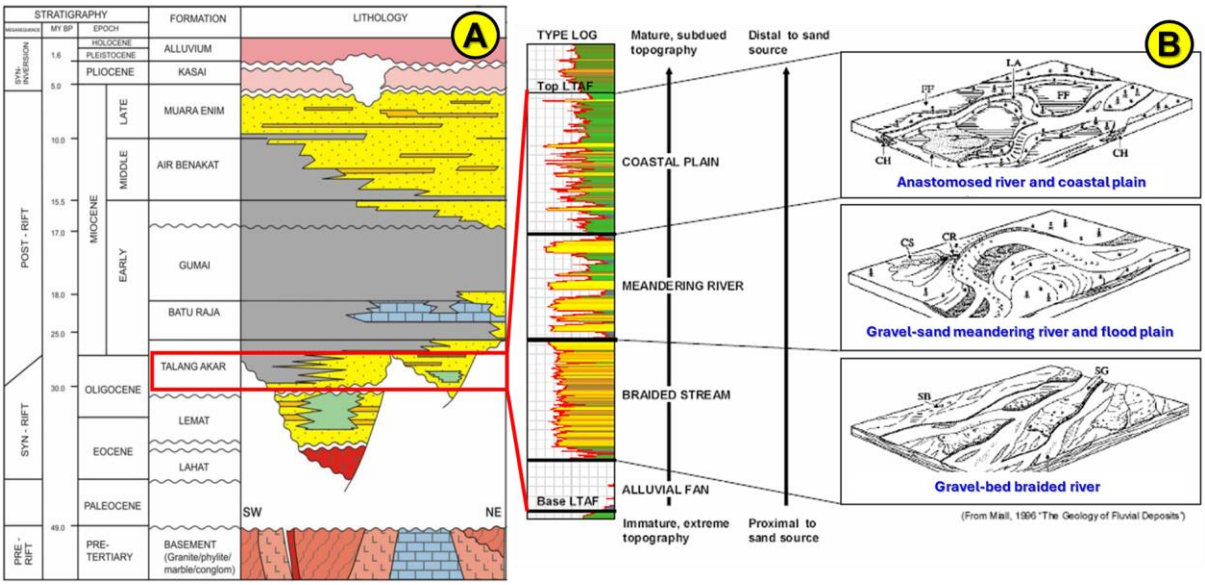

Figure 2. (A) South Sumatra Basin generalized structural and stratigraphy section. (B) The sediment model, reservoir characteristics, and geometry of the LTAF from Log Data (Modified from Ginger & Fielding, 2005).

Materials and Methods

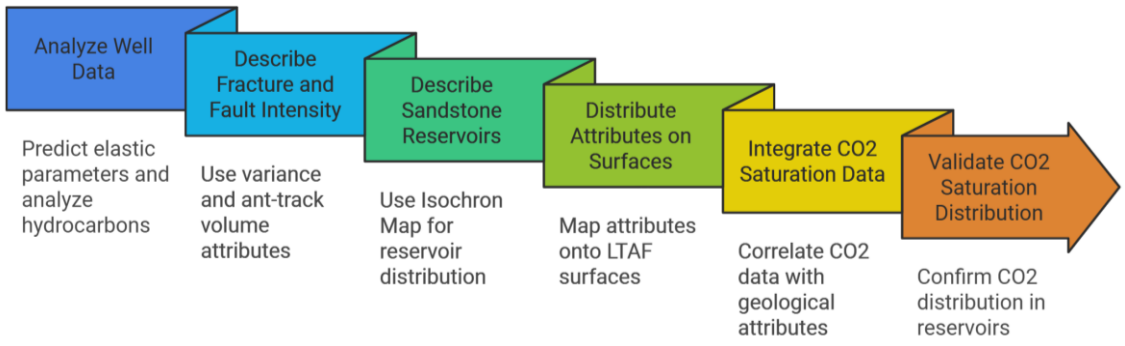

Figure 3. Study sequence to validate the distribution of CO_2 saturation in the sandstone reservoirs of the LTAF.

The data used in this study are well data and 3D post-stack seismic and the results of LTAF and Basement structure interpretation. Figure 3 shows the first stage of this study is the analysis of well data in the form of prediction of elastic parameters S-Wave by multi attribute method and sensitivity analysis of hydrocarbons, reservoirs, and non-reservoirs using elastic parameters P-Impedance, Vp/Vs ratio. The next stage is the description of fracture and fault intensity using variance and ant-track volume attributes. The results of these volume attributes are distributed on the LTAF and basement surfaces. The distribution of sandstone reservoirs in the LTAF interval is described with the Isochron Map, the sum of negative amplitude and relative impedance degenerate attributes from the LTAF-Basement interval analysis window. Finally, integrating CO_2 saturation distribution from well data qualitatively with fracture and fault intensity distribution and sandstone reservoir distribution represents the LTAF interval. This integration is essential to validate the distribution of CO_2 saturation in the sandstone reservoirs of the LTAF so that we can predict its origin, saturation, and distribution.

Multiatribute analysis for S-Wave Log prediction

Multiattribute analysis is performed with multiattribute linear regression which aims to find an operator in predicting well logs. Validation is a parameter to determine the correctness of the number of attributes used (Pratama et al., 2019). The target log is modeled by a linear equation (Pratama et al., 2019):

$$L\,(t) = w_0 + w_1A_1(t) + w_2A_2(t) + w_3A_3(t) \quad (1)$$

where, L represents the target log and w_n represents the number of log weights and represents the attributes.

The weights in this equation are generated by minimizing the mean-square prediction error (Pratama et al., 2019):

$$E^2 = \sum_{i=1}^{N}(L_i - w_0 - w_1A_{1i} - w_2A_{2i} - w_3A_{3i})^2 \quad (2)$$

where E represents the error, i represents the i-th well and N is the number of known points (i.e. samples) in the analysis.

The validation error for each number of attributes is always greater than the training error due to deleting data (when having one well that lacks log completeness is used). When plotting the average error against the number of attributes used, the training process shows a continuous decrease. However, the validation process often shows a minimum number, and then increases again. This minimum number is the ideal number of attributes to use, and more attributes only cause overtraining. (Pratama, et al., 2019).

Sensitivity analysis

Log derivative is a step before conducting sensitivity analysis by cross plotting log P-Impedance and Vp/Vs ratio. The logs used are gamma ray logs to distinguish non reservoir zones and sandstone reservoirs, resistivity logs to distinguish non reservoir zones and fluid-filled reservoirs, and Poisson's ratio logs to discriminate the type of fluid filling the reservoir. The derived logs are made following the equation (Russell, 2017).

$$Ip = Vp \times \rho \quad (3)$$

$$\sigma = \frac{GR - GR_{ss}}{GR_{shale - GR_{ss}}} \times (\sigma_{shale} - \sigma_{ss}) + \sigma_{ss} \quad (4)$$

$$\text{Vp/Vs Ratio} = log\ Vp \times log\ Vs \quad (5)$$

where,

Ip : P-Impedance ((ft/s)*(g/cc))
Vp : P-Wave Velocity (ft/s)
Vs : S-Wave Velocity (ft/s)
ρ : Density (g/cc)
GR_{Bss} : Baseline sand (American Petroleum Institute or API)
GR_{BShale}: Baseline shale (American Petroleum Institute or API)
σ_{Bss} : Poisson's value of sandstone (unitless)
σ_{BShale} : Poisson's value of shale (unitless)

Rock physics analysis is conducted to understand the character and physical properties of rocks and fluids using well data, seismic data, or both. Russell (2015) cross plotted the P-impedance parameter with the Vp/Vs ratio to separate lithologies and fluids into five clusters: shale, wet sand, gas sand, and cemented sand with reference to the rock physics template shown in Figure 4.

There is a contrast in Poisson's ratio in porous rock layers that contain fluid (especially gas), and the Vp value also decreases (Figure 5). So, Poisson's ratio can be used in identifying the presence of gas.

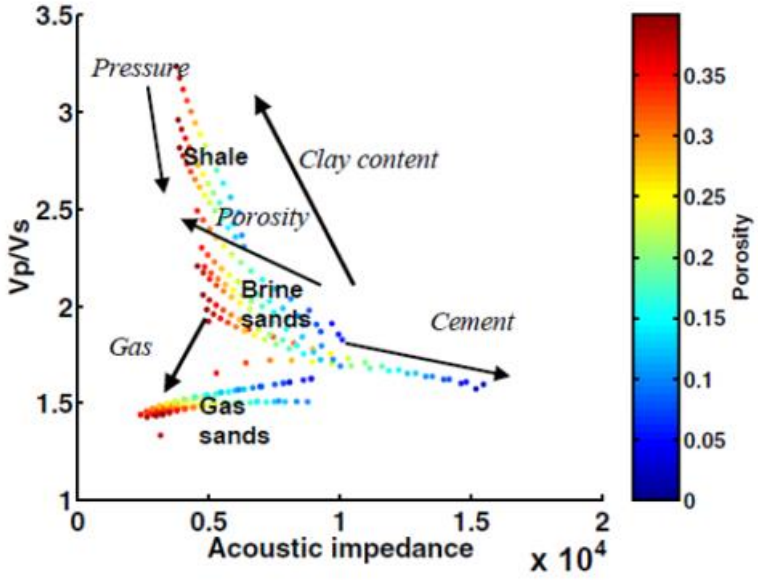

Figure 4. Rock physics template (Russell, 2015).

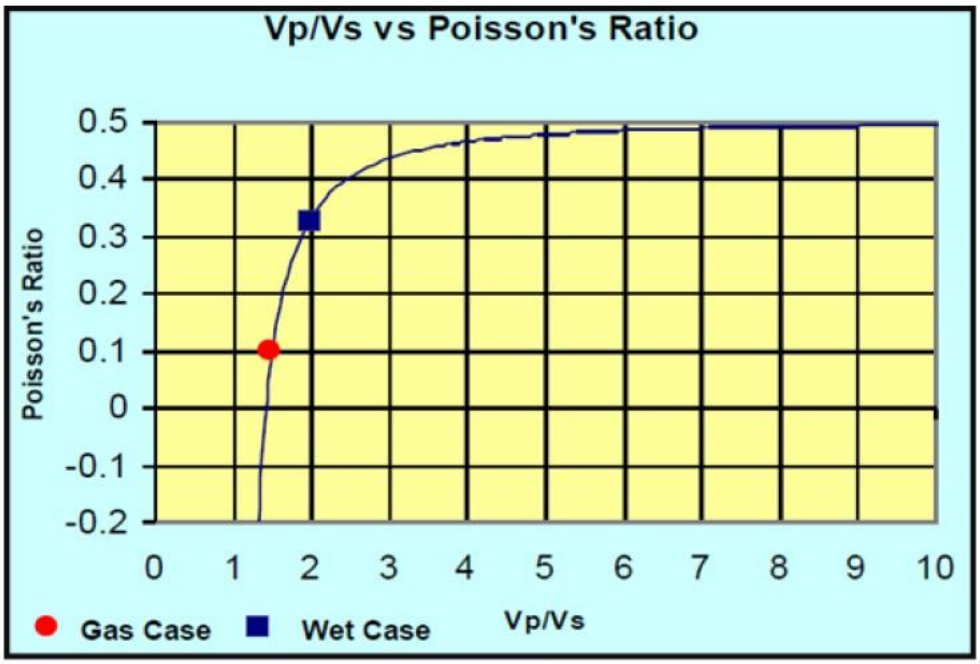

Figure 5. Plot Vp/Vs ratio vs Poisson's ratio (Alamsyah & Muhtar, 2017).

Seismic attributes

The types of amplitude attributes used in seismic attribute analysis in this study are as follows;

a. Variance Attribute

The variance attribute is called edge detection because it serves to clarify the edge of a surface change. This attribute detects slope changes in seismic data by comparing some data around the main data (Hijria & Danusaputro, 2016). Mathematically, the calculation of Variance normalization is as follows:

$$Variance = \frac{1}{J-1}\sum_{j=1}^{J}(Uji - < Uj >)^2 \quad (6)$$

where, J showing the center trace. <Uj> the mean value of the test and i is the analysis window. This attribute parameter is on the difference in waveforms or traces that are measured based on similarities both

adjacent and vertically. So, it is very effective in describing the boundaries or edges of the main fault zones and fractures (Hijria & Danusaputro, 2016).

b. Ant Tracking Attribute

Variance and ant-track attribute volumes can describe amplitude discontinuities so that they are good at delineating fault structures, fractures, and reservoir bodies in a region (Ngeri et al., 2015; Hijria & Danusaputro, 2016; Abdel-Fattah et al., 2020; Alamsyah et al., 2023). The scattering map obtained is a representation of the intensity of the amplitude discontinuity pattern identified with a darker color, bright red or bright blue. This intensity can be interpreted as the intensity of fractures and faults that we believe are seismically visible (Figure 6).

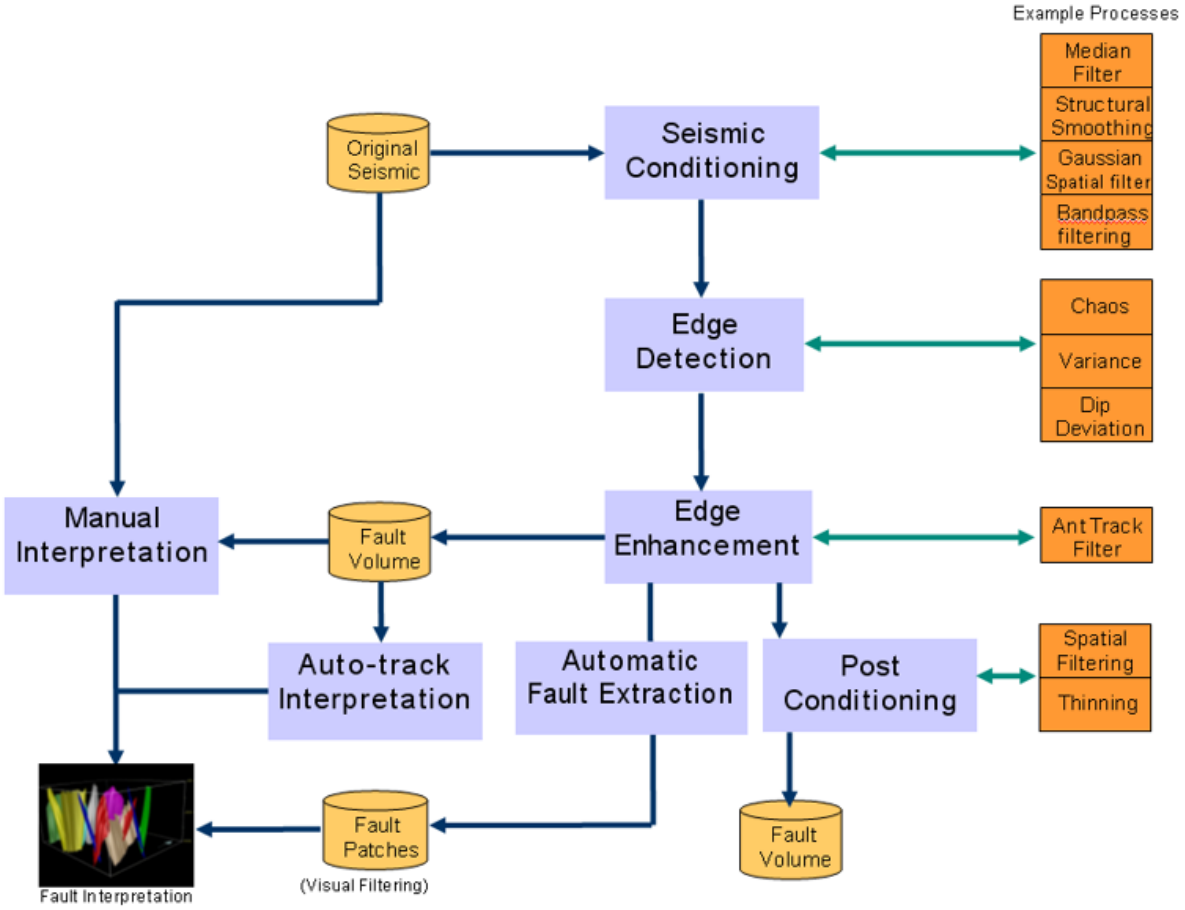

Figure 6. Schematic of ant tracking methodology (Ali et al., 2016).

c. Relative Impedance Acoustic Attributes (RAI)

Reservoir distribution in relative impedance acoustic attribute by Emujakporue & Enyenihi (2020) this attribute is used to describe sequence boundaries, and thickness variations. The acoustic impedance of a medium is given as:

$$I = \rho V \qquad (7)$$

where,

V : velocity (m/s)
I : acoustic impedance (kg/m^{2}s)
ρ : density (kg/m^3)

High relative acoustic impedance values are associated with shale-bearing facies, while lower values are associated with sand intervals (Emujakporue & Enyenihi, 2020).

d. Sum of Negative Amplitude attribute

The sum negative amplitude attribute can be calculated by summing the negative

amplitudes shown in the following equation (Alamsyah, et al., 2023).

$$SNA = \sum_{i=1}^{N}(-a_i)N \qquad (8)$$

Where, a_i is the i-th amplitude value, with i=1,2,3, etc., and N is the number of negative amplitudes.

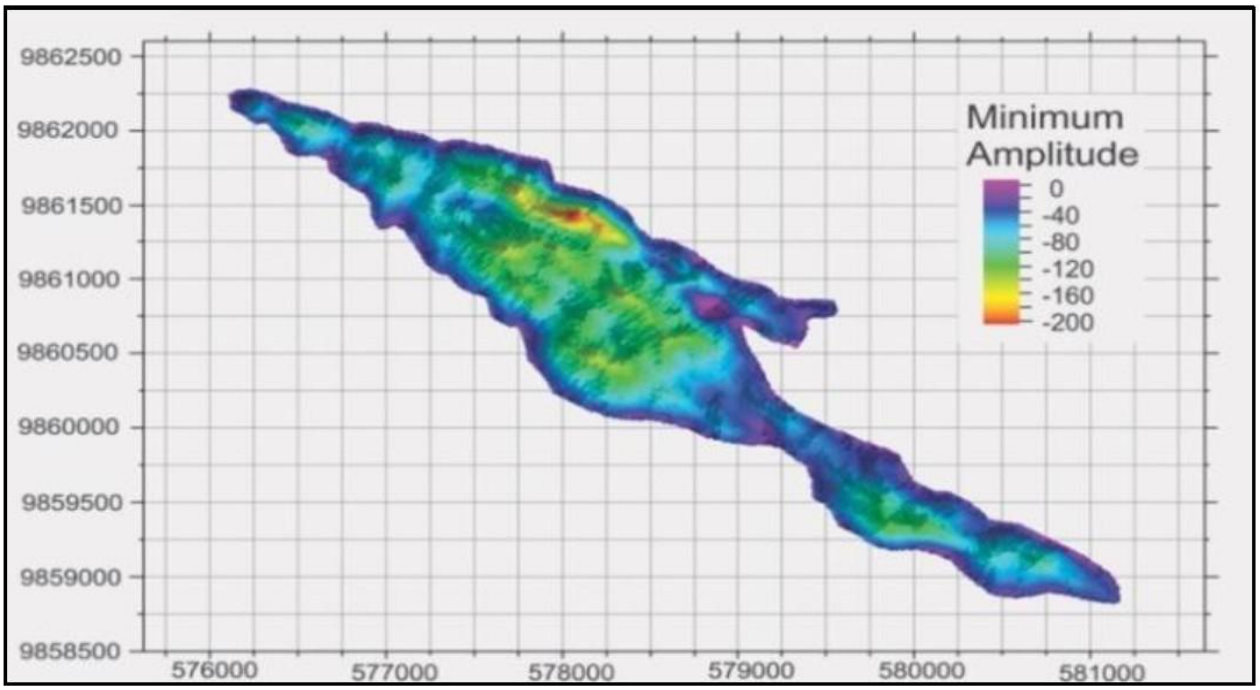

Figure 7. Example of minimum amplitude attribute application (Haris et al., 2018).

e. Minimum Amplitude Attribute

The minimum amplitude attribute calculates the minimum value of the trough or its minimum amplitude. This attribute in Haris et al. (2018) is used to see the distribution that shows the channel geometry of the sand body, which is obtained by extracting the tuning amplitude from the target reservoir surface area. The tuning amplitude illustrates that the channel sand body forms an elongated cluster and develops in a northwest to southeast direction as shown in Figure 7.

The sum of negative amplitude attribute results from the summation of negative values within the upper and lower analysis window coverage of the interest zone in the seismic data, which can indicate the presence of sand reservoirs and the presence of gaseous hydrocarbons, provided that the hydrocarbon zone is characterized by low impedance which is identical to the presence of through in the seismic cross section (Didi et al., 2022; Côrte et al., 2020; Okeke et al., 2021 and Hesham, et al., 2023). The relative acoustic impedance attribute is based on comparing the contrast between the reservoir impedance and the surrounding lithology in a particular interval. This attribute is widely used to delineate sequence boundaries, areas of unconformity and discontinuity, and the presence of fluid in the reservoir (Emujakporue & Enyenihi, 2020; Lohitanon, 2021; Allo et al., 2022; Franklin et al., 2023).

Results and Discussion

Multiattribute Analysis

Multiattribute analysis was applied to 53 wells to predict logs because these wells did not have complete S-Wave logs.

The list of available attributes is shown in the right-side of Figure 8. Looking at the error trends in training and validation shows that log prediction only uses 4 attributes because the 5th attribute is

overtrained which is shown by the increasing validation error value. This is shown in left-side.

The predicted log S-wave output is shown in Figure 9. Multiattribute analysis was performed with inputs from wells RPH-16 and RPH-7 that had the originals S-Wave to predict the S-wave in wells RPH-8 and RPH-5. The correlation is 0.9, which indicates a good correlation of the multiattribute analysis result. Based on the result of overall multiattribute analysis on 57 wells, the S-wave log prediction results show a good correlation value of ≥ 0,86.

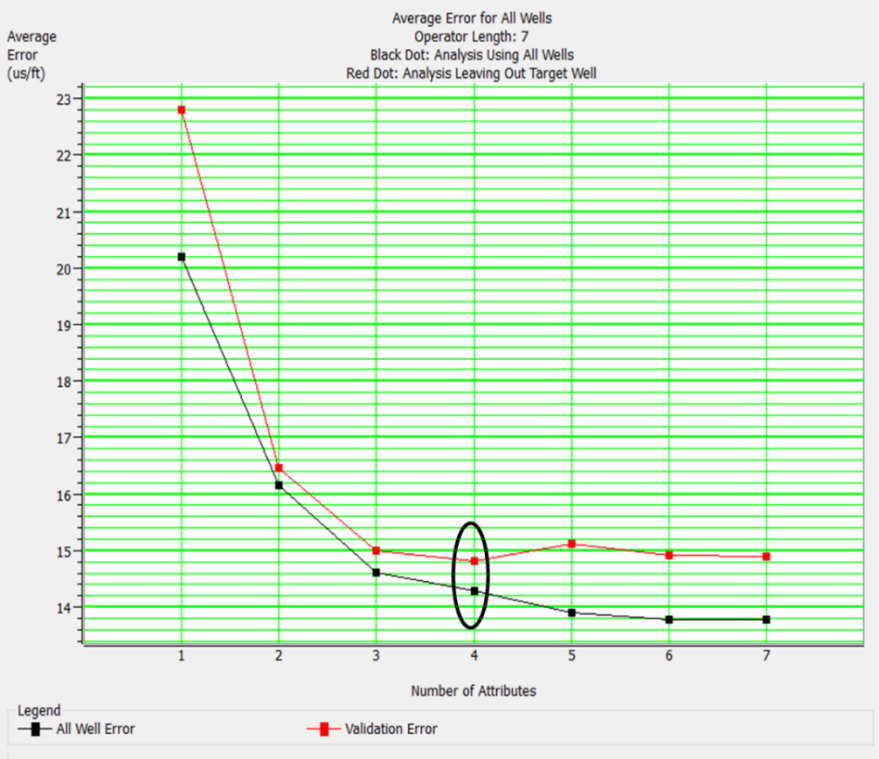

Multiple Attribute Correlation Results

Multi-Attribute List: Multi Attribute List 1

	Target	Final Attribute	Training Error	Validatior
1	Sqrt(S-wave)	Sqrt(Neutron Porosity)	20.226909	22.816695
2	Sqrt(S-wave)	Log(P-wave)	16.176267	16.476597
3	Sqrt(S-wave)	(Gamma Ray)**2	14.631167	15.025293
4	Sqrt(S-wave)	Sqrt(Density)	14.309914	14.838132
5	Sqrt(S-wave)	Log(Resistivity)	13.914447	15.144828
6	Sqrt(S-wave)	Sqrt(Porosity)	13.808217	14.929293
7	Sqrt(S-wave)	Sqrt(Permeability)	13.802008	14.917780

Figure 8. (Bottom) List of available attributes for predicting Log S-Wave and (top) is error plot for each attribute showing the 4th best attribute.

Sensitivity Analysis

This analysis is divided into 3 which aims to separate the reservoir and non-reservoir zones using as in Figure 10, to separate the fluid filled reservoir zone and non-reservoir as in Figure 11, and then to discriminate the fluid that fills the reservoir as in Figure 13.

The results obtained for the reservoir zone have a P-Impedance value of 6000-9000 ((m/s)(g/cc)) which is in the range of P-impedance values of non-reservoir zones so that the P-impedance parameter in this case is less sensitive. While the Vp/Vs ratio of the reservoir zone is 1.1-1.5 which shows a smaller value than the non-reservoir zone.

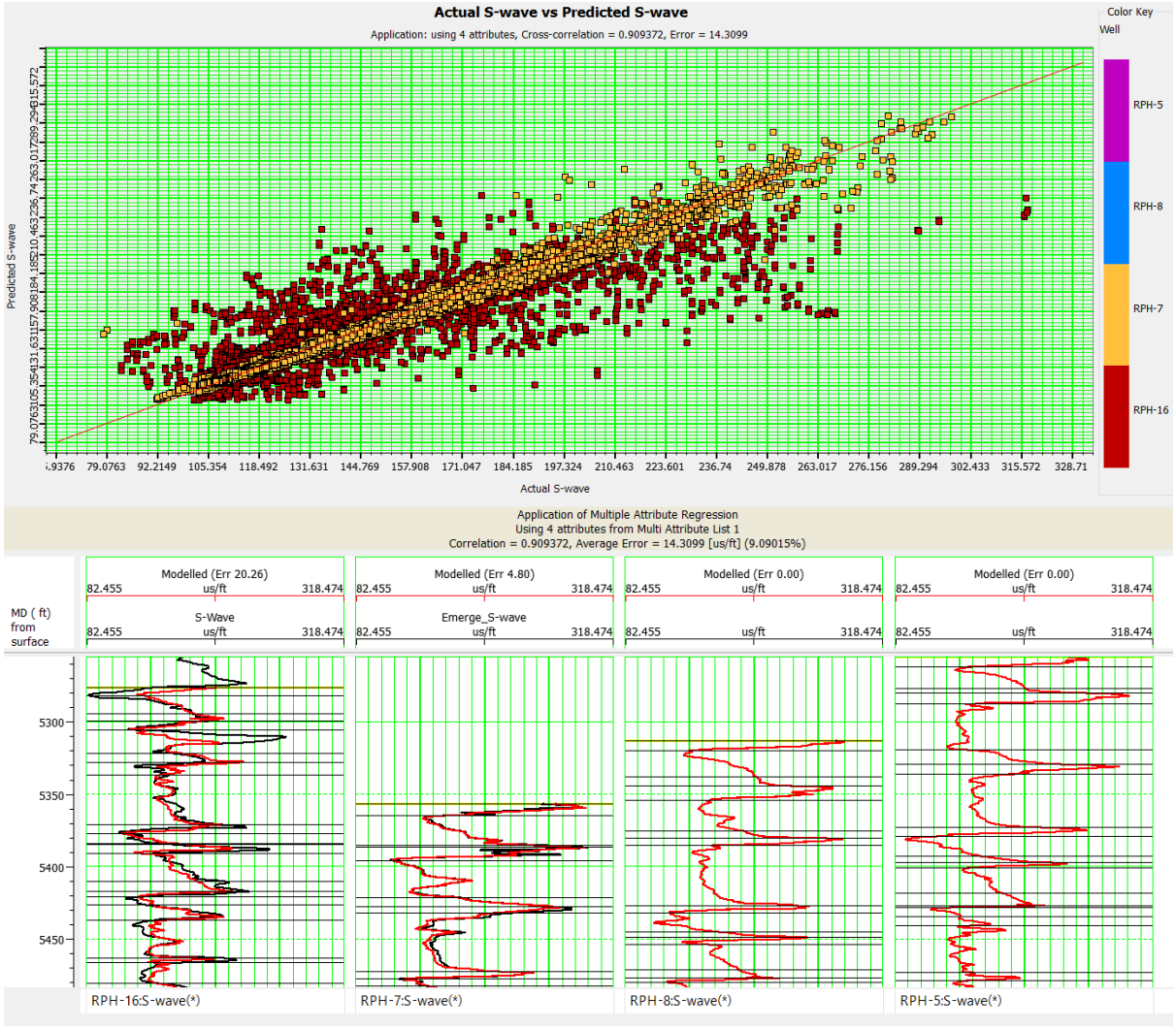

Figure 9. (top) Results showing correlation values and (bottom) comparison between original log S-wave (black) and predicted s-wave (red).

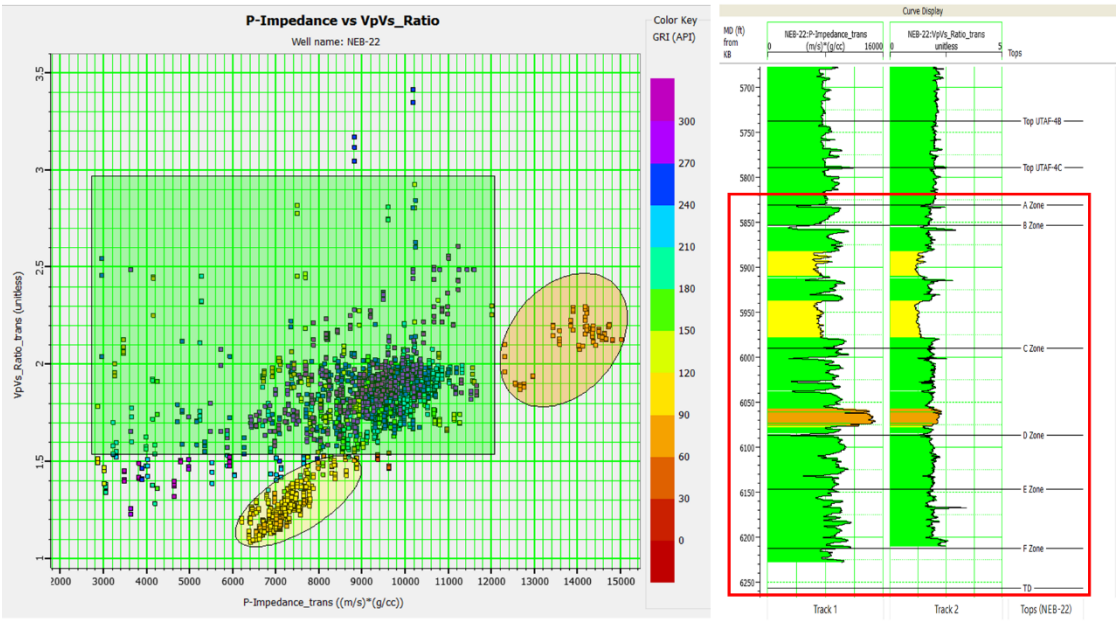

Figure 10. Sensitivity analysis to distinguish reservoir (yellow circle) and non-reservoir (green square).

In Figure 10, color-key gamma ray shows the difference in radioactive values contained in rocks so that rocks that are potentially reservoirs indicate lower gamma ray values because they have less radioactive content, this is shown in the yellow circle with a range of 60-100 (API). Non reservoir zones are indicated by higher gamma ray values marked with a green square.

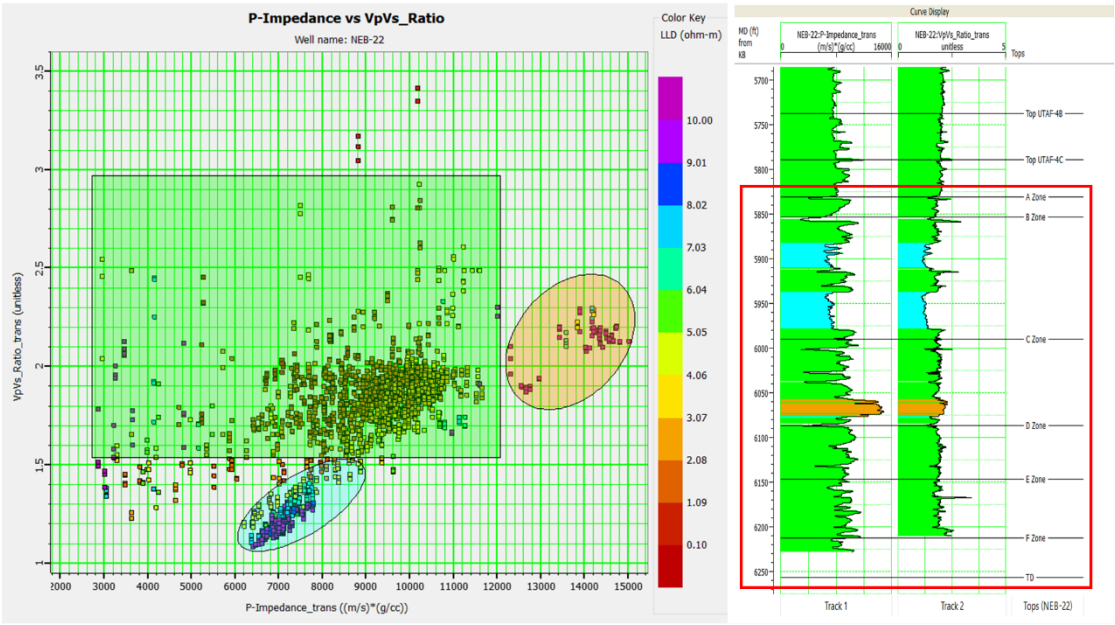

Figure 11. Sensitivity analysis to reservoir zones distinguishes fluid-filled (light blue circle) and non-reservoir.

In Figure 11, color-key resistivity indicates a permeable zone when it has a high resistivity value. When the reservoir is filled with hydrocarbons, the resistivity shows a higher value than when filled with water, this is shown in the light blue zone when filled with hydrocarbons, the resistivity is shown in red color with a value of 8-10 Ωm.

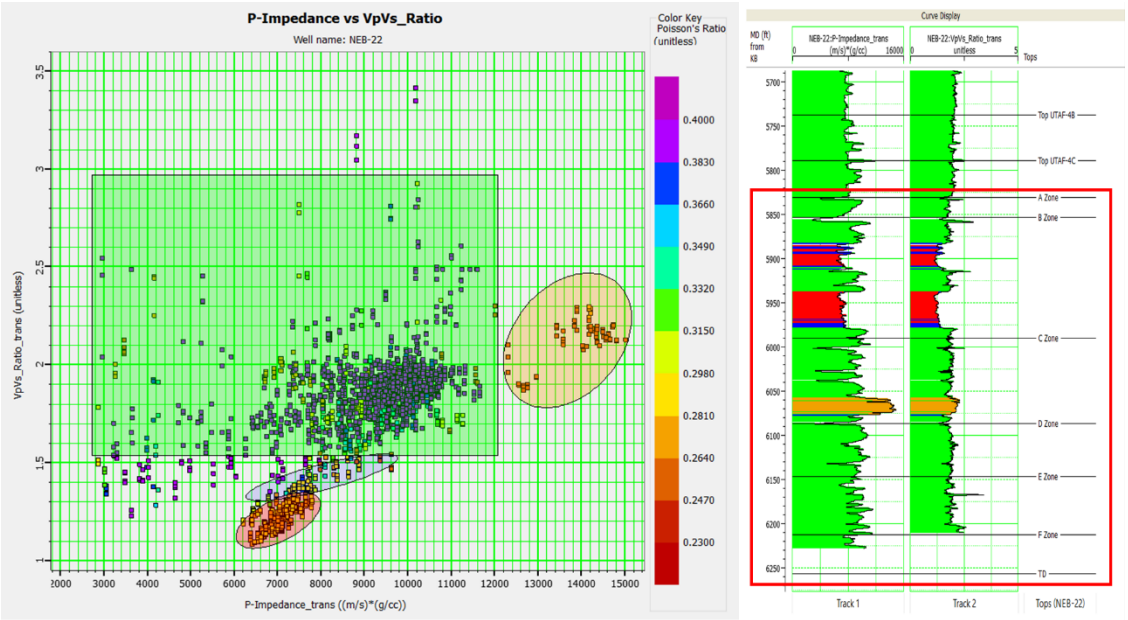

Figure 12. Sensitivity analysis to distinguish the type of fluid filling the reservoir (gas, oil, or water), but this figure shows the reservoir is only filled with gas (red circle) and water (blue circle).

In Figure 12, color-key Poisson's ratio indicates the type of fluid that fills the reservoir so that when filled by gas it will show a value of 0.1-0.25 marked with a red zone in curve display and when filled by water it will show a Poisson's ratio of 0.3 marked with a blue zone and non-reservoirs show a value > 0.3.

Seismic Attribute Analysis

Seismic attributes were applied to see the distribution of faults and reservoirs in area 'X'. Attribute values close to 1 are interpreted as the presence of faults, so the main faults in area 'X' are oriented north-south, northwest-southeast, and northeast-southwest (Figure 13). The higher fault intensity is in the eastern field area. While the lower fault intensity is in the western field area.

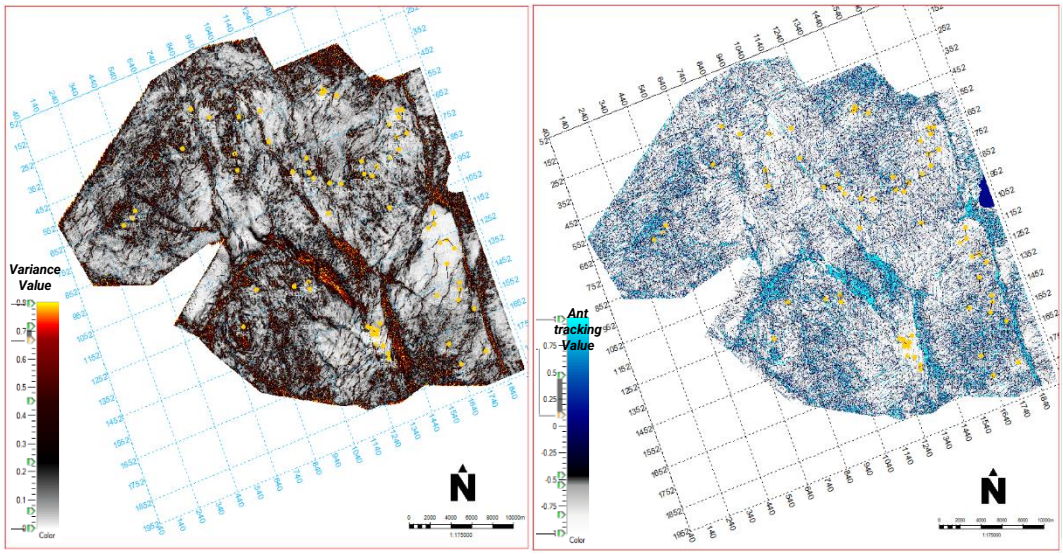

Figure 13. Visualization of intensity and distribution of faults in the LTAF Formation (right) Variance attribute, (left) Ant Tracking attribute.

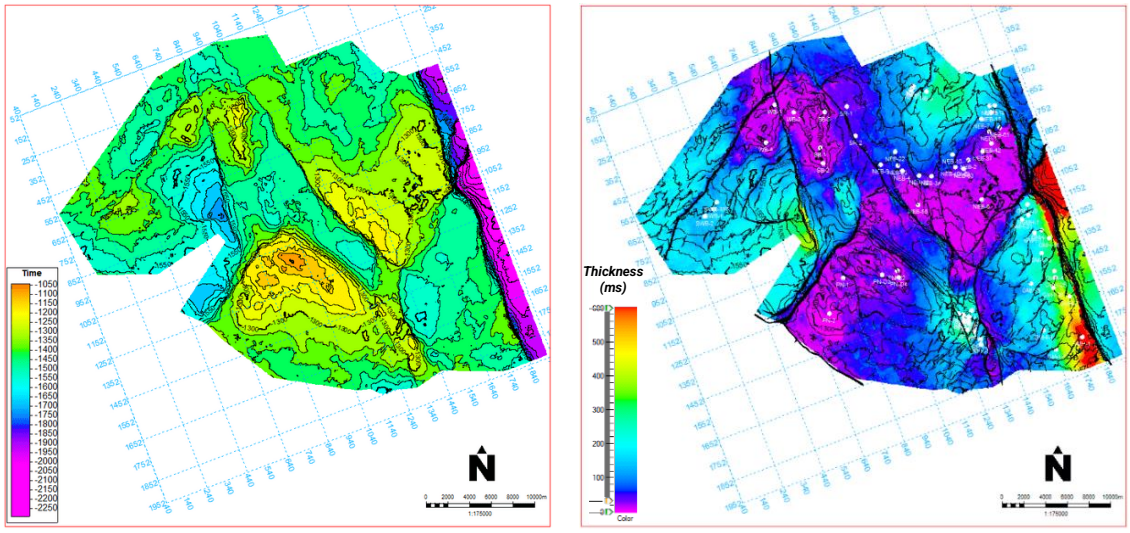

Figure 14. Relative thickness of reservoir (a) time structure map of LTAF Formation, (b) isochrone map of LTAF-Basement interval.

The relative thickness of the reservoir can be seen Figure 14. There is a time difference in the time structure indicating that shallower areas are shown with faster times, and vice versa. As for the relative thickness of reservoirs, it is indicated by dark blue-purple color with values <100 ms spreading in the center of area 'X', and thicker reservoirs are indicated by values >100 ms.

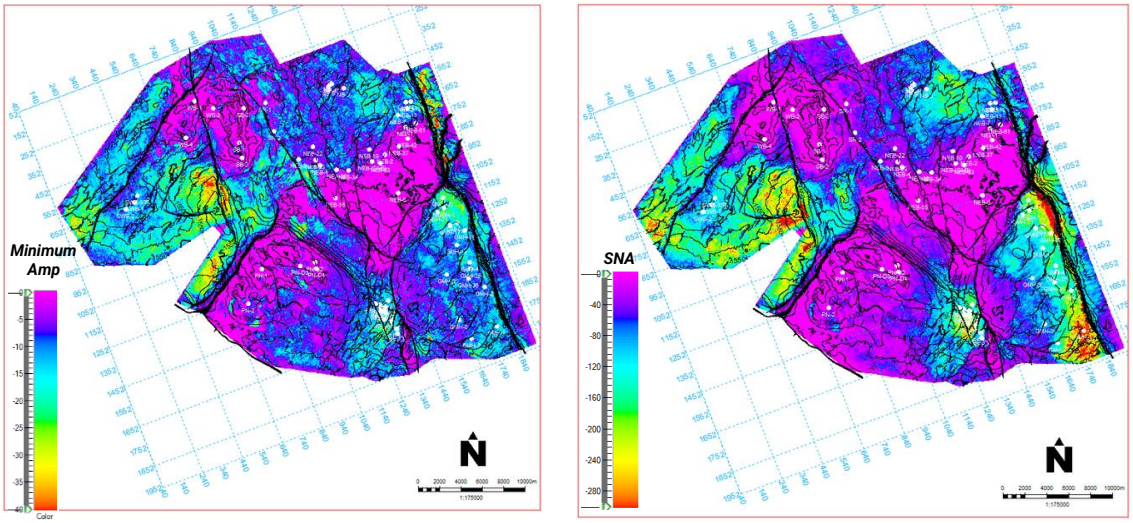

Figure 15. Reservoir distribution (a) Relative Acoustic Impedance-Minimum Amplitude attributes, (b) Sum of Negative Amplitude attributes.

Reservoir distribution is done by applying relative seismic data, namely Acoustic Impedance at the minimum amplitude attribute and conventional seismic at the Sum Negative Amplitude attribute.

So that the results obtained look consistent in describing the distribution of reservoirs shown in Figure 15. Attributes with low values are shown in purple, interpreted as areas that have higher porosity that spread in the middle of the area. Otherwise, research areas with relatively thick reservoirs are interpreted as having low porosity that spreads to the north, south, west, and southeast shown in light blue to red.

Distribution of CO_2 Impurities

The percentage of natural CO_2 distribution was obtained from well test data. The data shows the CO_2 content contained in the hydrocarbons in each well, which is then mapped to the natural CO_2 saturation distribution. Yellow to red colors indicate high saturation of impurities with a percentage of >50%, while purple indicates low saturation with a percentage of <50%. The distribution of high CO_2 saturation spreads in the eastern part. While the distribution of low CO_2 saturation spreads in the western part of the 'X' area. The areas with high and low impurity saturation are separated by a large northwest-southeast trending fault. Towards the west, the CO_2 saturation spreads with a low percentage. The high CO_2 impurity originates from the Betara Deep area associated with the pre-tertiary basement and the high intensity of faults and fractures in the area that affect the hydrocarbon distribution.

Integration of the LTAF and Isochron structure maps (Figure 16) with the seismic result map of the sum of negative amplitude and relative impedance attributes to identify the gross distribution of sandstone reservoirs in the LTAF interval regionally shows the same trend. The trend of reservoir distribution shows N-S and NE-SW directions, which correspond to the regional trend distribution map of LTAF sedimentation described in Figure 1. In general, the sandstone reservoirs in this LTAF interval have low-impedance elastic parameters (Alamsyah, 2010) and thus show negative valuations in seismic amplitude (Alamsyah et al., 2023). Qualitatively, integrating these maps is a good validation to describe the gross distribution of sandstone reservoirs for the LTAF interval in this X area.

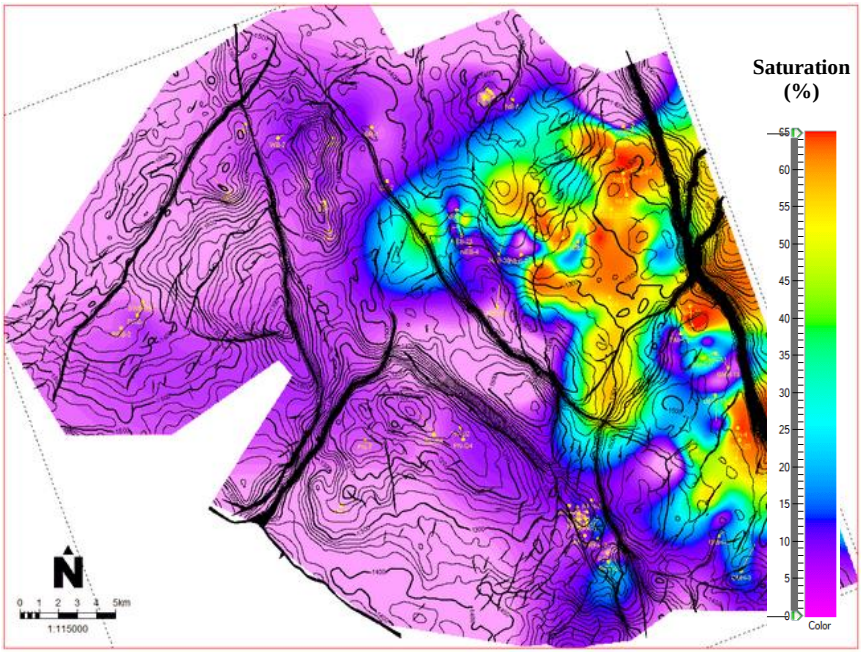

Figure 16. Saturation distribution map of natural CO_2 impurities (well based) in the LTAF-Basement interval which shows high in the eastern area.

From the attribute model, the consistency is shown by the significant intensity in the area adjacent to the main fault zone, which is oriented N-S and NE-SW. This significant intensity may result from the reactivation of the main faults during the inversion process so that it can be an alternative migration path for hydrocarbons to fill the reservoir in the LTAF interval. The integration results show the correspondence between the distribution of CO_2 saturation and the intensity of fractures and faults, where the high CO_2 saturation comes from the east with a reasonably high CO_2 saturation, and the further west, the CO_2 saturation decreases. There is consistency in the distribution of sandstone reservoirs based on the resulting seismic attributes, and the intensity of fractures and faults also affects the CO_2 migration path.

The results of this study provide information and validation for the western region of Area X, which has the potential for field development with thick reservoir zones and low CO_2 impurities content. This potential area must be followed up with reservoir engineering studies and its subsurface and non-subsurface economics.

Conclusion

The study concludes that sandstone and hydrocarbon reservoirs in the LTAF interval of area X are primarily sensitive to elastic P-Impedance and Vp/Vs ratio. In contrast, sandstone reservoirs are characterized by low impedance and gas hydrocarbons by a low Vp/Vs ratio. In Area X, the fault distribution trends north-south, northwest-southeast, and northeast-southwest, with a higher intensity in the eastern section, while relatively thick reservoirs are distributed across the north, south, west, and southeast. The distribution of CO_2 impurity saturation gets lower towards the west. With the consistency of the distribution of CO_2 impurity saturation to reservoirs and the intensity of faults and fractures obtained from seismic attribute analysis, it is possible to identify areas with thick reservoirs and low CO_2 zones that have the potential for further development.

Acknowledgements

The authors would like to thank PT PetroChina International Jabung Ltd. for providing secondary data that supports this research.

Author Contribution

Authors 1 and 3 discuss, interpret and write the script, authors 2 4 and 5 discuss and assist in proofreading the script.

Conflict of Interest

The authors declare no conflict of interest.

References

Abdel-Fattah, M. I., Pigott, J. D., & El-Sadek, M. S. (2020). Integrated Seismic Attributes and Stochastic Inversion for Reservoir Characterization: Insights from Wadi Field (NE AbuGharadig Basin, Egypt). *Journal of African Earth Sciences*, 161, 103661. https://doi.org/10.1016/j.jafrearsci.2019.103661

Alamsyah, M. N., Fitrianto, T., Sukmono, S., & Winardhi, S. (2023). A Preliminary Analysis of Natural CO_2-Saturated Gas Sands Distribution in the Gemah Field-Jabung Block, South Sumatra Basin, Indonesia, by using Simple Seismic Attributes. *The Leading Edge*, 42(11), 726-788. https://doi.org/10.1190/tle42110748.1

Alamsyah, M. N., & Muhtar, L. K. (2017). AVA Characteristics on Alluvial Facies Reservoir - Case Study : NEB Field, Jabung Block, South Sumatera Basin. *Conference paper* https://www.researchgate.net/publication/346974001

Allo, O. J., Bako, M. E., & Esan, D. (2022). Seismic Attribute Analysis for Prospect Delineation in 'TMB' Field, Niger Delta Basin, Nigerial. *Journal of Applied Sciences and Environmental Management*, 26(3), 487–494. https://doi.org/10.4314/jasem.v26i3.17

Ambarsari, D. S., Winardhi, I. S., Prakoso, S., & Sukmono, S. (2020). Reservoir quality determination by using critical porosity and volume of clay: A case study in the Talang Akar Formation in the NW Java Basin, Indonesia. *First Break*, 38(5), 63–70. https://doi.org/10.3997/1365-2397.fb2020035

Côrte, G., Dramsch, J., Amini, H., & MacBeth, C. (2020). Deep Neural Network Application for 4D Seismic Inversion to Changes in Pressure and Saturation: Optimizing the use of Synthetic Training datasets. *Geophysical Prospecting*, 68(7), 2164–2185. https://doi.org/10.1111/1365-2478.12982

Didi, C. N., Obiadi, I. I., Okeke, S. E., Anakor, S. N., & Ikomi, M. K. (2022). Lithostratigraphic Interpretation and The Analysis of The Depositional Environment of Nigeria Chad Basin using Well Log Data and Seismic Data. *Meridian Journal of Physical Sciences*, 2(1), 70–112. https://www.theinterscholar.org/journals/index.php/mjps/article/view/164

Emujakporue, G. O., & Enyenihi, E. E. (2020). Identification of Seismic Attributes for Hydrocarbon Prospecting of Akos Field, Niger Delta, Nigeria. *SN Applied Sciences*, 2(5), 910. https://doi.org/10.1007/s42452-020-2570-1

Franklin, E. C., Ndubuisi, E. G., & Udoka, C. I. (2023). Reservoir identification in Bornu Basin, Northeastern Nigeria using seismic attribute analysis. *International Journal of Scientific Research in Multidisciplinary Studies*, 9(2), 01–08. https://www.isroset.org/journal/IJS

RMS/full_paper_view.php?paper_id=3064

Ginger, D., & Fielding, K. (2005). The Petroleum Systems and Future Potential of The South Sumatra Basin. *Proc. Indon Petrol. Assoc., 30th Ann. Conv.* Thirtieth Annual Convention. https://doi.org/10.29118/IPA.2226.05.G.039

Haris, A., Riyanto, A., & Mardiyati, S. (2018). Statistical Tuning Chart for Mapping Porosity Thickness: A Case Study of Channel Sand Bodies in the Kutei Basin Reservoir. *TELKOMNIKA(Telecommunication Computing Electronics and Control)*, 16(6), 2676–2682. https://doi.org/10.12928/telkomnika.v16i6.9660

Hesham, A., Fattah, N. A., & Dahroug. A. (2023). Integrating Seismic Attributes and Rock Physics for Delineating Pliocene Reservoir in Disouq Field, Nile Delta, Egypt. *Contributions to Geophysics and Geodesy*, 53(1), 65–84. https://doi.org/10.31577/congeo.2023.53.1.4

Hidayat, M., Hartanto, D. T., Azis, M. M., & Sutijan, S. (2020). Studi Penambahan Etilena Glikol dalam Menghambat Pembentukan Metana Hidrat pada Proses Pemurnian Gas Alam. *Jurnal Rekayasa Proses*, 14(2), 198–212. https://doi.org/10.22146/jsrekpros.59871

Hijria, T. V., & Danusaputro, H. (2016). Analisis Persebaran Zona Reservoir Lapangan DT-1 Menggunakan Metode Inversi Impedansi Akustik dan Atribut Variansi. *Youngster Physics Journal*, 5, 1–12. https://ejournal3.undip.ac.id/index.php/bfd/article/view/10627

Lohitanon, P. (2021). Reservoir imaging using seismic attributes, Pattani Basin, Thailand. *Bulletin of Earth Sciences of Thailand*, 10(2), 142–152. https://ph01.tci-thaijo.org/index.php/bestjournal/article/view/246753

Ngeri, A. P., Tamurnobereton-ari, I., & Amakiri, A. (2015). Ant-tracker attributes: An Effective Approach to Enhancing Fault Identification and Interpretation. *IOSR Journal of VLSI and Signal Processing*, 5(6), 67–73. https://www.iosrjournals.org/iosr-jvlsi/papers/vol5-issue6/Version-2/J05626773.pdf

Okeke, S., Didi, C., Ngene, T., & Oyekola, P. (2021). Evaluation of Prospective Hydrocarbon Zones in Soedinc Field, Offshore Norway. *11th Annual International Conference on Industrial Engineering and Operations Management*, IEOM Society International. http://dx.doi.org/10.46254/AN11.20211076

Ali, A., Othman, A., Mohamed, A. A. M., & Mohamed, F. M. (2016). Improving Fault Tracing Detection Applying 3D Ant Tracking Seismic Attribute. *IOSR Journal of Applied Geology and Geophysics*, 4(3), 18–25. https://www.iosrjournals.org/iosr-jagg/papers/vol4-issue3/Version-1/D0403011825.pdf

Pratama, E., Mulyatno, B. S., & Zaenudin, A. (2019). Analisis Reservoar Migas (Sandstone) Menggunakan Multiatribut Seismik pada Lapangan TG12, Cekungan Barito, Kalimantan Selatan. *Jurnal Geofisika Eksplorasi*, 5(1), 3–14. https://doi.org/10.23960/jge.v5i1.19

Russell, B. (2015). Visualizing Inversion Results with Rock Physics Templates. *CREWES Research Report, Volume 27*.

Russell, Hampson. (2017). *CGG GeoSoftware Log Transform Theory*. HRS.

Sanjaya, A. S., & Nofendy, A. (2018). Prediksi Pembentukan Hidrat Gas dengan Pengaruh Joule-Thomson Effect yang Diakibatkan oleh Choke Performance. *Jurnal Chemurgy*, 1(1), 1–8. https://doi.org/10.30872/cmg.v1i1.1132

Sembiring, S., Panjaitan, R. L., Susianto, S., & Altway, A. (2019). Pemanfaatan Gas Alam sebagai LPG (*Liquified Petroleum Gas*). Jurnal Teknik ITS, 8(2), F206–F211. https://doi.org/10.12962/j23373539.v8i2.47079

ISSN: 2579-5821 (Print)
ISSN: 2579-5546 (Online)
URL address: http://journal.unhas.ac.id/index.php/geocelebes
DOI: 10.70561/geocelebes.v9i1.43409

Jurnal Geocelebes Vol. 9 No. 1, April 2025, 59 – 77

Impact of El Niño - Southern Oscillation (ENSO) and Indian Ocean Dipole (IOD) on Air Temperature in Bengkulu City

Mardho Tillah Edkayasa, Elfi Yuliza, Lizalidiawati*

Department of Physics, Faculty of Mathematics and Natural Sciences, University of Bengkulu, Bengkulu 38371, Indonesia

*Corresponding author. Email: lizalidiawati@unib.ac.id

Manuscript received: 5 March 2025; Received in revised form: 17 April 2025; Accepted: 29 April 2025

Abstract

Bengkulu City has experienced rising air temperatures due to climate variability events, particularly ENSO and IOD. This study analyzes the relationship between ENSO, IOD, and air temperature in Bengkulu over the past 20 years (2004-2023) using data from Meteorological and Climatology stations, as well as ONI and DMI indices from NOAA. Pearson and multiple correlation analyses show a temperature increase of 0.08-0.1°C per year. ENSO has a stronger influence than IOD, especially on maximum temperature (r = 0.28-0.38). To strengthen the analysis, multiple linear regression was applied, revealing that ONI had a statistically significant positive effect on average air temperature, while DMI showed a weaker and insignificant influence (R^2 = 0.10-0.11). A phase-based composite analysis revealed that average temperatures peaked during El Niño combined with Positive IOD phases, highlighting their synergistic warming effect, with maximum temperature reaching 35.9°C (February 2019), and the lowest minimum temperature recorded at 18°C (September 2019). The temperature increase during El Niño poses risks such as prolonged dry seasons, increased drought, and disruption of coastal ecosystems. Therefore, adaptation measures such as early warning systems and water resource management must be integrated into regional planning, particularly in agriculture and health sectors in Bengkulu.

Keywords: Air temperature; Bengkulu City; Climate Variability; ENSO; IOD.

Citation: Edkayasa, M. T., Yuliza, E., & Lizalidiawati, L. (2025). Impact of El Niño-Southern Oscillation (ENSO) and Indian Ocean Dipole (IOD) on Air Temperature in Bengkulu City. *Jurnal Geocelebes*, 9(1):59–77, doi: 10.70561/geocelebes.v9i1.43409

Introduction

As a tropical coastal region, Bengkulu experiences temperature fluctuations influenced by global climate phenomena, particularly the El Niño-Southern Oscillation (ENSO) and the Indian Ocean Dipole (IOD) (Wardani et al., 2023; Ismail et al., 2020). ENSO is a major climate phenomenon that alters Pacific Sea surface temperatures and subsequently affects global and regional weather patterns, including in Indonesia (Millenia et al., 2023). Meanwhile, IOD is an ocean-atmosphere interaction phenomenon in the Indian Ocean that causes differences in sea surface temperatures between the western and eastern parts of the ocean (Pillai et al., 2024; Kaboth-Bahr et al., 2024). Both phenomena significantly impact Indonesia's climate and air temperature, including in coastal regions like Bengkulu.

ENSO and IOD significantly influence global climate patterns through their individual and interactive effects. ENSO, characterized by variations in sea surface temperatures in the Pacific Ocean, drives extreme weather events such as droughts and floods worldwide (Yu et al., 2017). Meanwhile, the IOD, involving anomalous fluctuations in sea surface temperatures in the Indian Ocean, can modulate ENSO effects, particularly in the Southern

Hemisphere (Andrian et al., 2024). During El Niño, air temperatures tend to rise, especially in urban areas, with surface temperature increases reaching up to 2.5°C higher than regions with different land cover (Eboy & Kemarau, 2023). This increase occurs due to reduced rainfall, which dries out the land and causes it to absorb more heat. Additionally, decreased cloud cover allows more solar radiation to reach the Earth's surface, while lower humidity levels make temperatures feel even hotter (Loeb et al., 2024; Liu et al., 2024; Wardani et al., 2023). Conversely, during La Niña, increased rainfall contributes to cooling effects through latent heat release from precipitation and enhanced cloud cover, which limits incoming solar radiation (McPhaden et al., 2023; Zhong et al., 2024). Previous studies by Stuivenvolt-Allen et al. (2024) and Xia et al. (2017) shown that ENSO intensity and frequency have shifted due to global warming, impacting temperature patterns in tropical regions. Moreover, a variant of ENSO known as ENSO Modoki has become more frequent in recent decades, exhibiting different impacts on temperature and precipitation compared to classical ENSO, particularly in western Indonesia (Zaini et al., 2024; Marathe & Karumuri, 2021).

Besides ENSO, IOD also plays a crucial role in influencing air temperatures in Eastern Sumatra. The positive IOD phase, when coinciding with El Niño, exacerbates temperature increases and reduces rainfall, intensifying drought conditions in Eastern Sumatra (Akhsan et al., 2023). El Niño combined with positive IOD leads to extreme temperature increases, which can impact various sectors such as agriculture and public health (Mishra et al., 2022). Since 1965, the frequency of simultaneous El Niño and positive IOD events has increased, indicating a potential shift in climate patterns that could affect the maritime continent's temperature in the long term (Xiao et al., 2022). In contrast, the negative IOD phase tends to increase rainfall, often leading to lower air temperatures due to atmospheric cooling effects (Zheng et al., 2024; Nasution et al., 2023).

Although this study primarily focuses on ENSO and IOD's impact on air temperatures in Bengkulu, other factors such as urbanization and land use changes must also be considered. Rapid urbanization can enhance the urban heat island effect, contributing to higher temperatures in city areas (Kong, 2025; Purohit, 2024). The conversion of green areas into built-up zones worsens this effect by reducing soil moisture and increasing surface albedo, which directly influences air temperature rises (Abudukade et al., 2023).

On a regional scale, several studies have examined the impact of ENSO and IOD on air temperatures across Indonesia. According to Ariska et al. (2022), a study conducted in Palembang indicated that during El Niño, air temperatures increased while rainfall decreased, whereas La Niña produced the opposite effect. Research in coastal Sumatra also found that during strong El Niño events, average air temperatures increased by 0.26-0.29°C per decade compared to normal conditions (Akhsan et al., 2023; Yuniasih et al., 2022). However, research specifically investigating the relationship between ENSO, IOD, and air temperatures in Bengkulu remains limited. Most of Previous studies have focused on rainfall rather than air temperature and have mostly been conducted outside Sumatra Island (Novianti et al., 2023).

Therefore, this study aims to fill this research gap by analyzing the relationship between ENSO, IOD, and air temperature variability (minimum, maximum, and average) in Bengkulu from 2004 to 2023. The findings are expected to provide scientific insights into the impact of global

climate variability on air temperatures in coastal Sumatra and serve as a reference for climate change adaptation planning, particularly for sectors reliant on weather conditions, such as agriculture, fisheries, and public health.

Materials and Methods

This study was conducted in Bengkulu City using air temperature data from Indonesian Agency for Meteorological, Climatological and Geophysics (BMKG) Fatmawati Soekarno Meteorological Station and Bengkulu Climatology Station for the period of 2004-2023. NOAA provided the data for the Oceanic Nino Index (ONI) and Dipole Mode Index (DMI).

Before conducting the analysis, all datasets underwent a quality control process. For the temperature data from Fatmawati Soekarno Meteorological Station and Bengkulu Climatology Station, outlier detection was performed using the Interquartile Range (IQR) method, and missing values were cross-checked with neighboring stations. The time series plots were visually inspected to ensure continuity and eliminate abrupt anomalies. Duplicate entries and inconsistencies were corrected manually. Validation was conducted for ONI and DMI indices to match the temporal resolution with the monthly climate data used in this study. No seasonal adjustment was applied to preserve the original variability linked to ENSO and IOD events.

Air temperature data were converted into monthly averages prior to analysis and subsequently processed using statistical and temporal analysis tools. The relationship between ENSO, IOD, and air temperature was analyzed using multiple methods, including Pearson Correlation to obtain the linear relationship between ONI, DMI, and air temperature (minimum, maximum, and average), formulated in Equation 1 (Turney, 2024):

$$r = \frac{\sum_{i=1}^{n}(x_i - \bar{x})(y_i - \bar{y})}{\sqrt{\sum_{i=1}^{n}(x_i - \bar{x})^2}\,\sqrt{\sum_{i=1}^{n}(y_i - \bar{y})^2}} \quad (1)$$

Where r is the correlation coefficient, x_i and y_i are variable values, index i represents each data point in the dataset, running for 1 to n, where n is the total number of observations, $\bar{x}$ and $\bar{y}$ are the averages of each variable (Turney, 2024). Next, Multiple Correlation was used to assess the strength of the relationship between air temperature (Y) and ENSO (X_1) and IOD (X_2) simultaneously, calculated using Equation 2 (Najarzadeh, 2020):

$$R = \frac{\sqrt{r_{y1}^2 + r_{y2}^2 2 r_{y1} r_{y2} r_{12}}}{1 - r_{12}^2} \quad (2)$$

where R is the multiple correlation coefficient between the dependent variable Y (air temperature) and the two independent variables X_1 (ONI) and X_2 (DMI); r_{y1} and r_{y2} are the Pearson correlation coefficients between Y and each independent variable; r_{12} is the Pearson correlation between ONI and DMI (Najarzadeh, 2020).

Multiple linear regression was applied to strengthen the statistical analysis and determine the combined influence of ONI and DMI on maximum air temperature. The regression model is expressed as follows in Equation 3:

$$T_{\text{avg}} = \beta_0 + \beta_1(\text{ONI}) + \beta_2(\text{DMI}) \quad (3)$$

where T_{avg} is the monthly average air temperature, β_0 is the intercept, and β_1 and β_2 are the regression coefficients representing the influence of ONI and DMI, respectively. The model's statistical performance was evaluated using the coefficient of determination (R^2), F-statistic, and *p*-values of each predictor to determine the strength and significance of the relationship.

Furthermore, a phase-based composite analysis was conducted by categorizing each month into ONI and DMI phase combinations to assess how different ENSO and IOD conditions interact to influence air temperature. ONI values were classified into El Niño (ONI ≥ +0.5), La Niña (ONI ≤ -0.5), and Neutral (-0.5 < ONI < +0.5), while DMI values were classified into Positive IOD (DMI ≥ +0.4), Negative IOD (DMI ≤ -0.4), and Neutral (-0.4 < DMI < +0.4). Monthly air temperature data were grouped accordingly and averaged for each combination. This approach does not involve anomaly-based climatological composites but allows a direct comparison of temperature responses across specific ENSO-IOD phase combinations.

The results of this analysis provide insights into how ENSO and IOD influence air temperature variability in Bengkulu over the long term.

Results and Discussion

Average Air Temperature Fluctuations

The average air temperature in Bengkulu City has shown an increasing trend over the period of 2004-2023 (Figures 1 and 2). Seasonal fluctuations appear consistent, following an annual cycle with several significant temperature peaks. This consistent upward trend aligns with global warming patterns and reflects long-term climatic shifts, as depicted by the trend line.

Based on Figure 1, the dark blue line represents fluctuations in the average air temperature, while the red line indicates the trend of the average air temperature. The average air temperature at Fatmawati Soekarno Meteorological Station in Bengkulu has shown an increasing trend from 2004 to 2023. Seasonal fluctuations remain consistent with the annual cycle, and the trend line in the graph indicates a gradual rise in temperature. The highest recorded temperature occurred in May 2023, reaching 28.3°C, possibly influenced by a moderate El Niño event (ONI = 0.5).

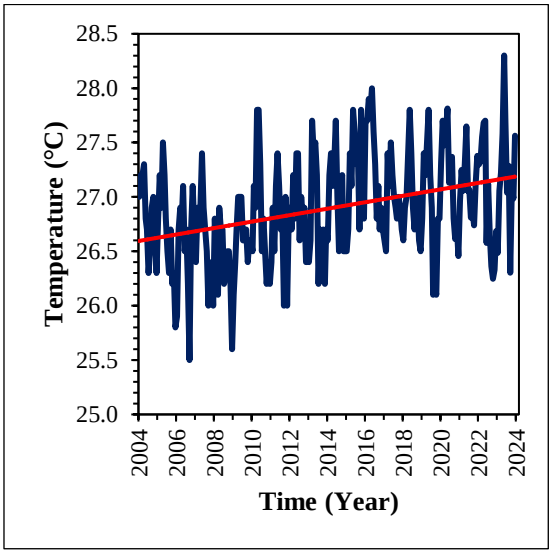

Figure 1. Average Air Temperature Trend at Fatmawati Soekarno Meteorological Station, Bengkulu (2004-2023).

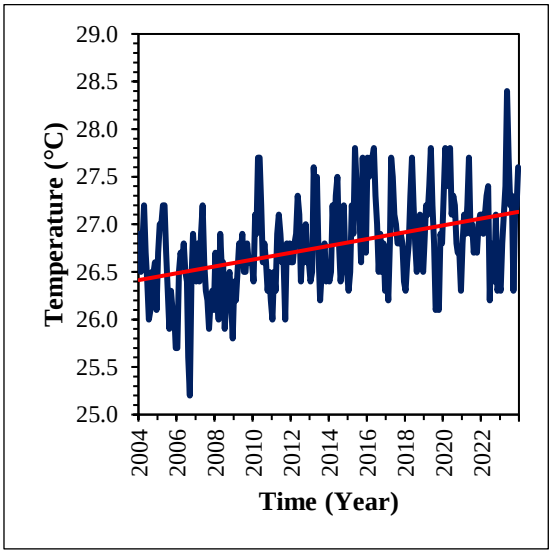

Figure 2. Average Air Temperature Trend at Bengkulu Climatology Station (2004-2023).

Jiang et al. (2025) confirmed that 2023 recorded the highest-ever global mean surface temperature (GMST), with El Niño warming and rising sea surface temperature (SST) as the primary contributing factors. Their study highlights how El Niño-induced warming and SST anomalies significantly contributed to the record GMST in 2023. This supports the finding that the temperature rise in Bengkulu in May 2023 is likely part of a broader global warming trend. Additionally, the

accelerated warming trend observed in their study suggests that increasing temperatures and extreme climate variability may persist, emphasizing the need for further research on regional climate impacts.

Meanwhile, Figure 2 illustrates the average air temperature pattern at Bengkulu Climatology Station, which also exhibits a similar increasing trend. The highest recorded temperature was 28.4°C in May 2023. Although there are slight differences between the two stations, the nearly identical upward trend suggests that local air temperature variability in Bengkulu City is closely correlated with global climate change.

Impact of ENSO and IOD on Average Air Temperature Trends

Based on Figure 3, the average air temperature trend from 2004 to 2023 shows an overall increase.

The trendline equation at Fatmawati Soekarno Meteorological Station indicates an increase of 0.00008°C per month (approximately 0.0096°C per decade), while at Bengkulu Climatology Station, the rise reaches 0.0001°C per month (or 0.012°C per decade). Although this increase is relatively small, it suggests a consistent long-term temperature change. Previous studies, such as Hansen et al. (2017) and Tan (2024), indicate that even minor but continuous warming trends can contribute to shifts in climate patterns, increased frequency of extreme weather events, and changes in local atmospheric dynamics. The IPCC (2021) estimates a global warming trend of approximately 0.2°C per decade, making these observed trends appear small but still relevant in a regional context.

ENSO and IOD influence air temperature, as seen in May 2023 when temperatures peaked (28.3°C at the Meteorological Station and 28.4°C at the Climatology Station) under moderate El Niño (ONI = 0.5) and neutral IOD (DMI = 0.02). El Niño increases air temperature, with impacts varying by intensity and duration. On the other hand, the warming trend is also influenced by global climate variability. During La Niña periods, the average air temperature tends to be lower than during El Niño, although the long-term trend remains upward. This suggests that temperature changes in Bengkulu are more strongly influenced by ENSO than by IOD, which has a weaker impact on average air temperature fluctuations.

A study by Jiang et al. (2025) highlights that El Niño has a significant influence on global mean surface temperature (GMST), with 2023 exemplifying this effect. While the Indian Ocean Dipole (IOD) plays a less dominant role, the warming trend persists, emphasizing ENSO's primary influence on temperature fluctuations. Their findings reinforce the notion that the temperature variations in Bengkulu are part of a broader global warming pattern, where ENSO-driven changes outweigh the effects of other climate phenomena. This further supports the observed trend that temperature increases during El Niño events are more pronounced, whereas the cooling effect of La Niña is insufficient to counteract the long-term warming trajectory.

Maximum Air Temperature Fluctuations

Based on Table 1, the maximum temperature at Fatmawati Soekarno Meteorological Station and Bengkulu Climatology Station exhibited significant fluctuations from 2004 to 2023. The peak temperatures were recorded in February 2019 (35.9°C) and May 2018 (36°C), coinciding with a Moderate El Niño (ONI = 0.7) and a Neutral to Slightly Negative IOD (DMI = -0.06). The trendline indicates a gradual increase at a rate of 0.0001°C per month at the Meteorological Station, with a slightly higher rate at the Climatology Station. Although small, this trend suggests an increase in extreme temperatures due to

global warming and regional climate variability.

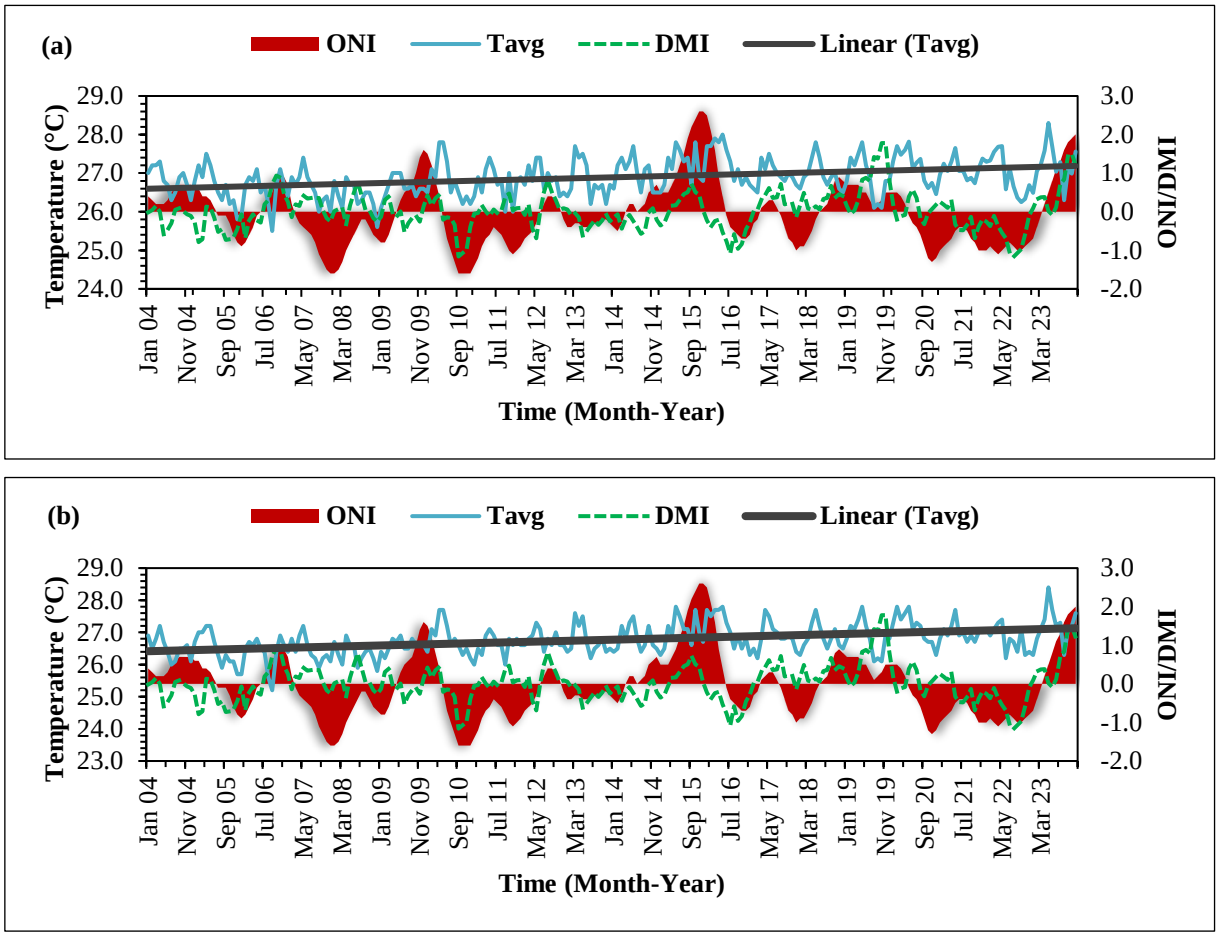

Figure 3. Time Series Graph of ENSO and IOD Events on Average Air Temperature at (a) Fatmawati Soekarno Meteorological Station, Bengkulu and (b) Bengkulu Climatology Station (2004-2023).

Table 1. Maximum temperature data for the 2004-2023 period.

Observation Station	*T*max		Index	
	Value	Time	ONI	DMI
Meteorological	35.9	Feb-19	0.7	-0.06
Climatology	36	May-18	-0.2	0.14

Maximum temperatures tend to be higher during El Niño due to reduced rainfall and humidity, whereas during La Niña, temperatures are lower due to increased precipitation. The data in Table 1 confirms that ENSO has a more dominant influence on maximum temperature compared to IOD. A study by Ferreira & Badinger (2023) also found that El Niño significantly increases average temperatures, particularly in December, across various cities in Brazil. Their analysis of historical climate trends indicates that this phenomenon is accompanied by decreased rainfall, exacerbating hot conditions. Thus, the stronger relationship between ENSO and maximum temperature observed in Bengkulu aligns with the patterns identified in their study, although regional factors may also influence the intensity of its impact.

Impact of ENSO and IOD on Maximum Air Temperature Trends

Based on Figure 4, the trend of maximum air temperature from 2004 to 2023 shows a stable increase. The trendline equation indicates a rise in maximum temperature of 0.0001°C per month at the Meteorological Station, with a slightly higher rate at the Climatology Station. Although small, this

trend reflects long-term warming due to global climate variability.

ENSO significantly influences fluctuations in maximum temperature. For example, in February 2019, the Meteorological Station recorded a maximum temperature of 35.9°C during a moderate El Niño event (ONI = 0.7) and a Neutral to Slightly Negative IOD (DMI = -0.06). Similarly, in May 2018, the maximum temperature at the Climatology Station reached 36°C despite being in a Weak La Niña phase (-0.2) and a Weak Positive IOD (DMI = 0.14). This indicates that El Niño tends to increase maximum temperatures, especially when rainfall decreases and humidity is lower. On the other hand, La Niña does not always significantly reduce maximum temperatures, as other factors such as solar radiation and regional atmospheric conditions also play a role. Meanwhile, the influence of IOD on maximum temperature in Bengkulu is relatively weak and does not always align with observed trends.

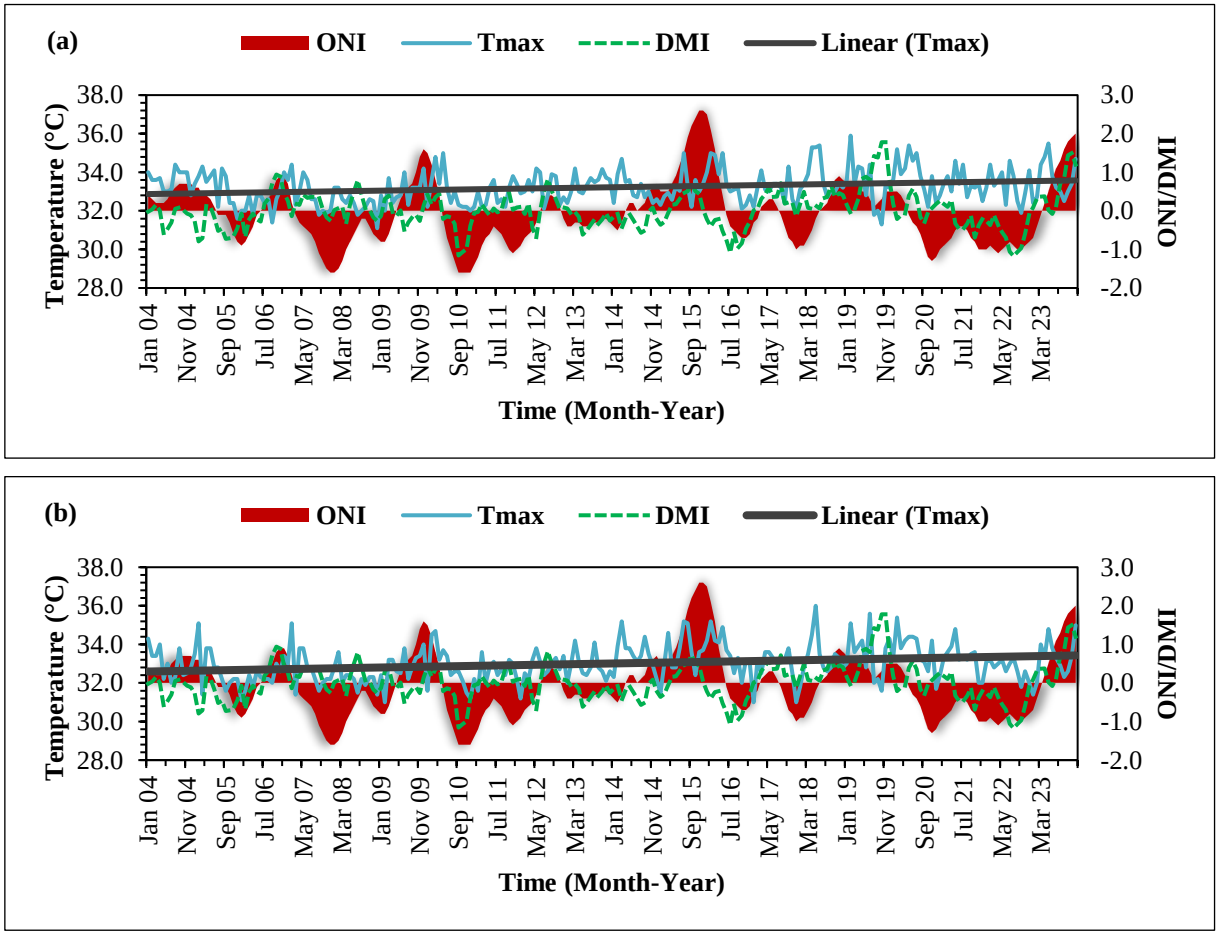

Figure 4. Time Series Graph of ENSO and IOD Events on Maximum Air Temperature at (a) Fatmawati Soekarno Meteorological Station, Bengkulu and (b) Bengkulu Climatology Station 2004-2023.

Minimum Air Temperature Fluctuations

Based on Table 2, the minimum air temperature showed significant fluctuations from 2004 to 2023. The lowest recorded temperature occurred in September 2019, reaching 18°C at the Meteorological Station and 19°C at the Climatology Station, when the ONI was at 0.2 (Neutral tending towards Weak El Niño) and the DMI reached 1.38 (Strong Positive IOD). This indicates that minimum temperature is more influenced by local atmospheric factors and regional circulation rather than ENSO. The trendline shows a gradual increase, at a rate of 0.00008°C per month at the Meteorological

Station and 0.0001°C per month at the Climatology Station, indicating long-term temperature changes due to global warming and shifts in regional climate patterns.

Table 2. Minimum temperature data for the 2004-2023 period.

Observation Station	Tmin		Index	
	Value	Time	ONI	DMI
Meteorological	18	Sep-19	0.2	1.38
Climatology	19	Sep-06	0.5	0.71
	19	Dec-10	-1.6	-0.39
	19	Jan-15	0.5	-0.36
	19	Sep-19	0.2	1.38

The fluctuation pattern of minimum temperature is more complex compared to maximum temperature. El Niño does not always significantly increase minimum temperature, while during La Niña, minimum temperature tends to be more stable. IOD also does not show a consistent relationship pattern, indicating that minimum temperature variability is more influenced by local factors such as humidity, cloud cover, and coastal atmospheric dynamics in Bengkulu.

The Influence of ENSO and IOD on Minimum Air Temperature Trends

Figure 5 indicates a gradual upward trend in minimum air temperature in Bengkulu from 2004 to 2023, with estimated increases of 0.00008°C/month at the Meteorological Station and 0.0001°C/month at the Climatology Station. However, the influence of ENSO and IOD phases on minimum temperature appears limited and inconsistent, suggesting a more substantial contribution from local atmospheric factors. For instance, the lowest temperature (18°C) occurred in September 2019 during a weak El Niño and strong positive IOD (ONI = 0.2, DMI = 1.38), yet similar extremes were not observed in other ENSO/IOD phases. These suggest that local atmospheric conditions-such as humidity, cloud cover, and coastal circulation have a stronger role in shaping minimum temperature trends than global climate indices. Overall, minimum temperature variations in Bengkulu are more complex than those of maximum or average temperature.

Composite Analysis of ENSO and IOD Phases on Air Temperature

A simplified phase-based composite analysis was conducted by grouping monthly temperature data according to ONI and DMI classifications to understand better the combined influence of ENSO dan IOD on air temperature variability. Each month from 2004 to 2023 was assigned to a specific ENSO-IOD phase based on ONI and DMI thresholds, resulting in five main combinations: ONI+ DMI+, ONI− DMI−, ONI+ DMI−, ONI− DMI+, and Neutral (ONI & DMI both within neutral range).

This approach does not calculate climatological anomalies, but instead averages observed temperature values within each phase group. The classification reflects the typical phase interactions of ENSO and IOD over three-month intervals, following climatological conventions. By using this grouped composite method, the study aims to highlight the general temperature response associated with different ENSO-IOD combinations. This form of phase-based composite classification is widely used in climate research to isolate the effects of concurrent climate drivers.

The average temperature values under each category are presented in Tables 3 and 4, revealing clear differences in Bengkulu's temperature response depending on the specific ENSO-IOD phase interaction.

The Table 3 also includes predicted average temperatures (T_{p-avg}) calculated using a multiple linear regression model based on ONI and DMI values (see Equation 4). These predicted values are intended to estimate the statistical contribution of climate drivers on air temperature and are not expected to perfectly match observed values due to the influence of local

atmospheric factors not captured in the model.

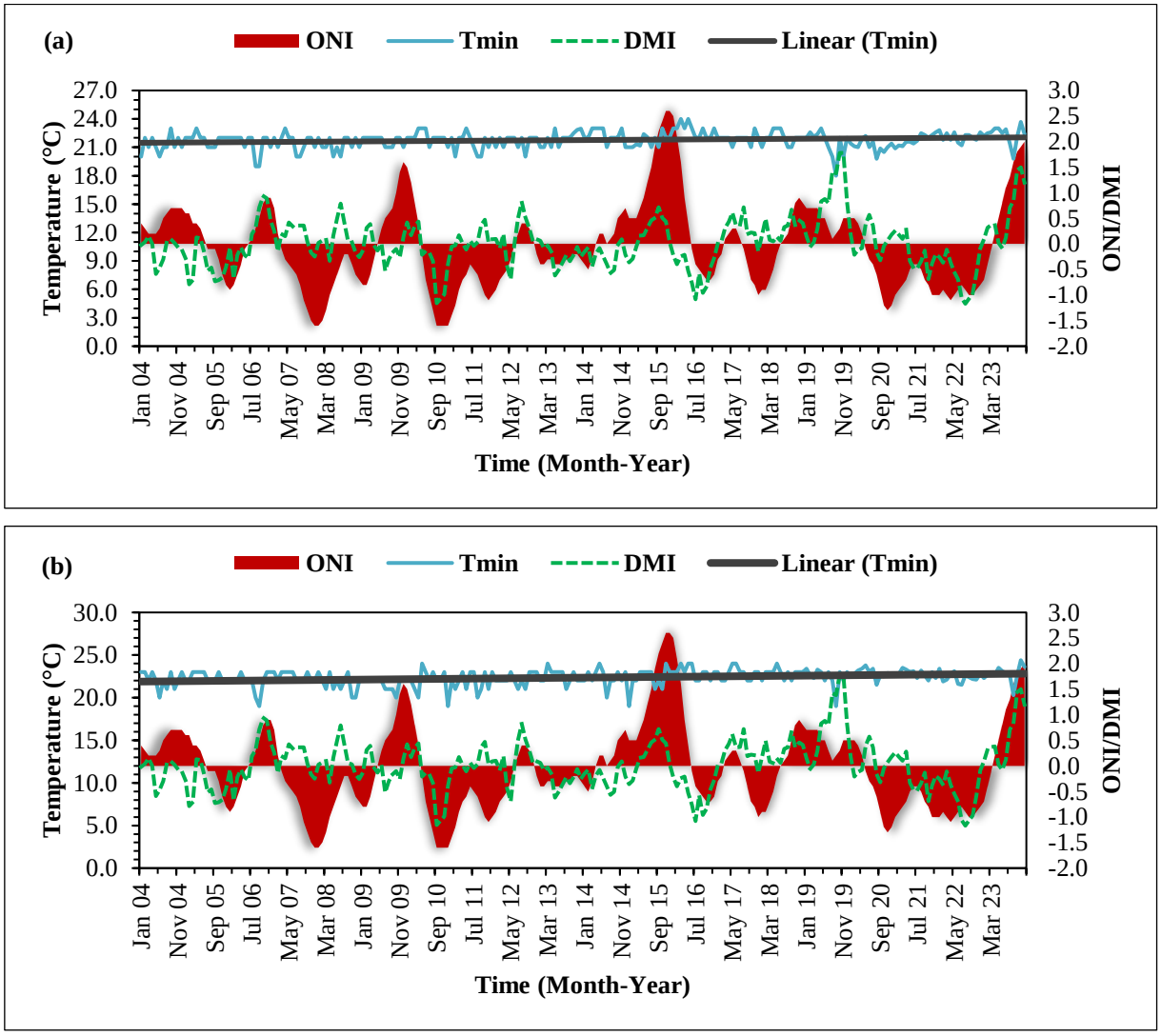

Figure 5. Time Series Graph of ENSO and IOD Events on Minimum Air Temperature at (a) Fatmawati Soekarno Meteorological Station, Bengkulu and (b) Bengkulu Climatology Station 2004-2023

Table 3. Classification of ENSO (ONI) and IOD (DMI) Phases and Corresponding Monthly Air Temperatures (Minimum, Average, and Maximum) at Fatmawati Soekarno Meteorological Station, Bengkulu (2004-2023).

Classification	Time	*T*			Index	
		*T*avg	*T*p – avg	*T*max	ONI	DMI
El Niño and Positive IOD	Sep-15	26.7	27.2	32.2	2.2	0.72
	Oct-15	27.8	27.3	33.6	2.4	0.51
	Nov-15	26.9	27.4	33.0	2.6	0.44
La Niña and Negative IOD	Sep-10	26.5	26.7	32.3	-1.6	-1.16
	Oct-10	26.2	26.7	32.2	-1.6	-1.07
	Nov-10	26.4	26.7	32.2	-1.6	-0.99
Normal	Apr-05	27.5	27.0	33.5	0.4	0.13
	May-05	27.2	27.0	33.8	0.3	0.11
	Jun-05	26.8	26.9	34.1	0.1	-0.16

Based on data from the Fatmawati Soekarno Meteorological Station in Bengkulu, the ONI+ DMI+ category, representing the combination of El Niño and Positive IOD, occurred from September to November 2015. During this

period, air temperature experienced a significant increase. In September 2015, the minimum temperature was recorded at 21.0°C, the average temperature at 26.7°C, and the maximum temperature at 32.2°C. By October 2015, the minimum temperature rose to 23.0°C, the average temperature reached 27.8°C, and the maximum temperature peaked at 33.6°C, supported by an ONI index of 2.4 and a DMI of 0.51. The peak of El Niño occurred in November 2015, marked by a slight decrease in maximum temperature to 33.0°C, while the average temperature remained high at 26.9°C. The ONI value increased to 2.6, indicating that this period was strongly influenced by the intensity of El Niño. The impact of this combination is illustrated in Figure 6a, which shows the trend of rising air temperatures during this period.

The ONI- DMI- category, representing the influence of La Niña and Negative IOD, occurred from September to November 2010. Data from the Fatmawati Soekarno Meteorological Station in Bengkulu indicate that air temperatures were lower compared to El Niño periods. In September 2010, the minimum temperature was recorded at 22.0°C, the average temperature at 26.5°C, and the maximum temperature at 32.3°C, with an ONI index of -1.6 and a DMI of -1.16. Similar conditions continued in October, with the average temperature slightly decreasing to 26.2°C while the maximum temperature remained around 32,2°C. By November 2010, the average temperature rose again to 26.4°C, while the ONI value remained at -1.6 and the DMI increased to -0.99, indicating that the influence of La Niña persisted but had begun to weaken. The graph in Figure 6b illustrates the air temperature patterns during this period, showing that temperatures were relatively lower compared to El Niño periods.

Meanwhile, the period from April to June 2005 was categorized as Normal, with no significant influence from ONI or DMI. During this time, air temperatures remained relatively stable, with minimum temperatures ranging between 22.0°C and 23.0°C and maximum temperatures between 33.5°C and 34.1°C. The ONI and DMI indices values were close to zero, indicating no significant ENSO or IOD anomalies affecting air temperatures drastically. This stability is also reflected in Figure 6c, which shows a more consistent temperature pattern compared to El Niño or La Niña periods.

Table 4. Classification of ENSO (ONI) and IOD (DMI) Phases and Corresponding Monthly Air Temperatures (Minimum, Average, and Maximum) at Bengkulu Climatology Station (2004-2023).

Classification	Time	*T*			Index	
		***T*avg**	***T*p − avg**	***T*max**	**ONI**	**DMI**
El Niño and Positive IOD	Sep-23	26.3	27.0	32.3	1.6	0.84
	Oct-23	27.1	27.0	32.6	1.8	1.44
	Nov-23	27.2	27.0	33.4	1.9	1.50
La Niña and Negative IOD	Sep-16	26.9	26.8	33.3	-0.6	-0.96
	Oct-16	26.5	26.7	32.0	-0.7	-0.84
	Nov-16	26.8	26.7	33.2	-0.7	-0.46
Normal	Jun-18	27.2	26.8	33.5	0.0	0.06
	Jul-18	26.8	26.8	32.8	0.1	0.33
	Aug-18	26.5	26.8	32.6	0.2	-0.36

The same analysis was conducted on data from the Bengkulu Climatology Station, as shown in Table 4, revealing a similar pattern. The period from September to November 2023 fell under the ONI+ DMI+ category, indicating a temperature increase due to El Niño combined with a Positive IOD. In September 2023, the minimum temperature was recorded at 20.3°C, with an average temperature of 26.3°C and a

maximum temperature of 32.3°C. The warming trend continued into October and November, with the maximum temperature reaching 33.4°C in the final month. The graph in Figure 7a illustrates that this temperature increase pattern is like that of 2015, reinforcing the conclusion that the El Niño combined with a Positive IOD contributes to significant warming in Bengkulu.

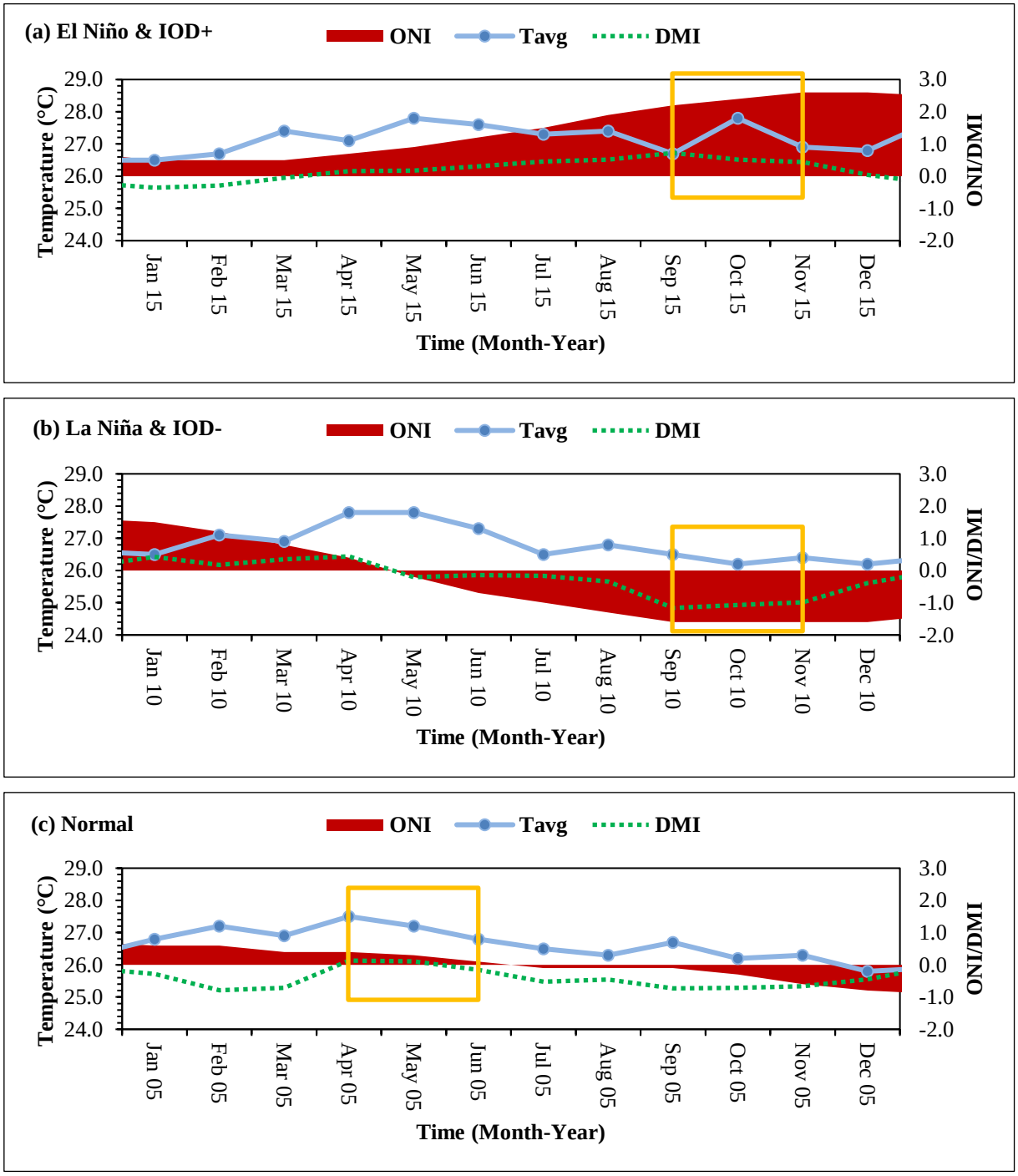

Figure 6. Average Air Temperature Trends During (a) El Niño and Positive IOD (Sep-Nov 2015), (b) La Niña and Negative IOD (Sep-Nov 2010), and (c) Normal Conditions (Apr-Jun 2005) at Fatmawati Soekarno Meteorological Station, Bengkulu.

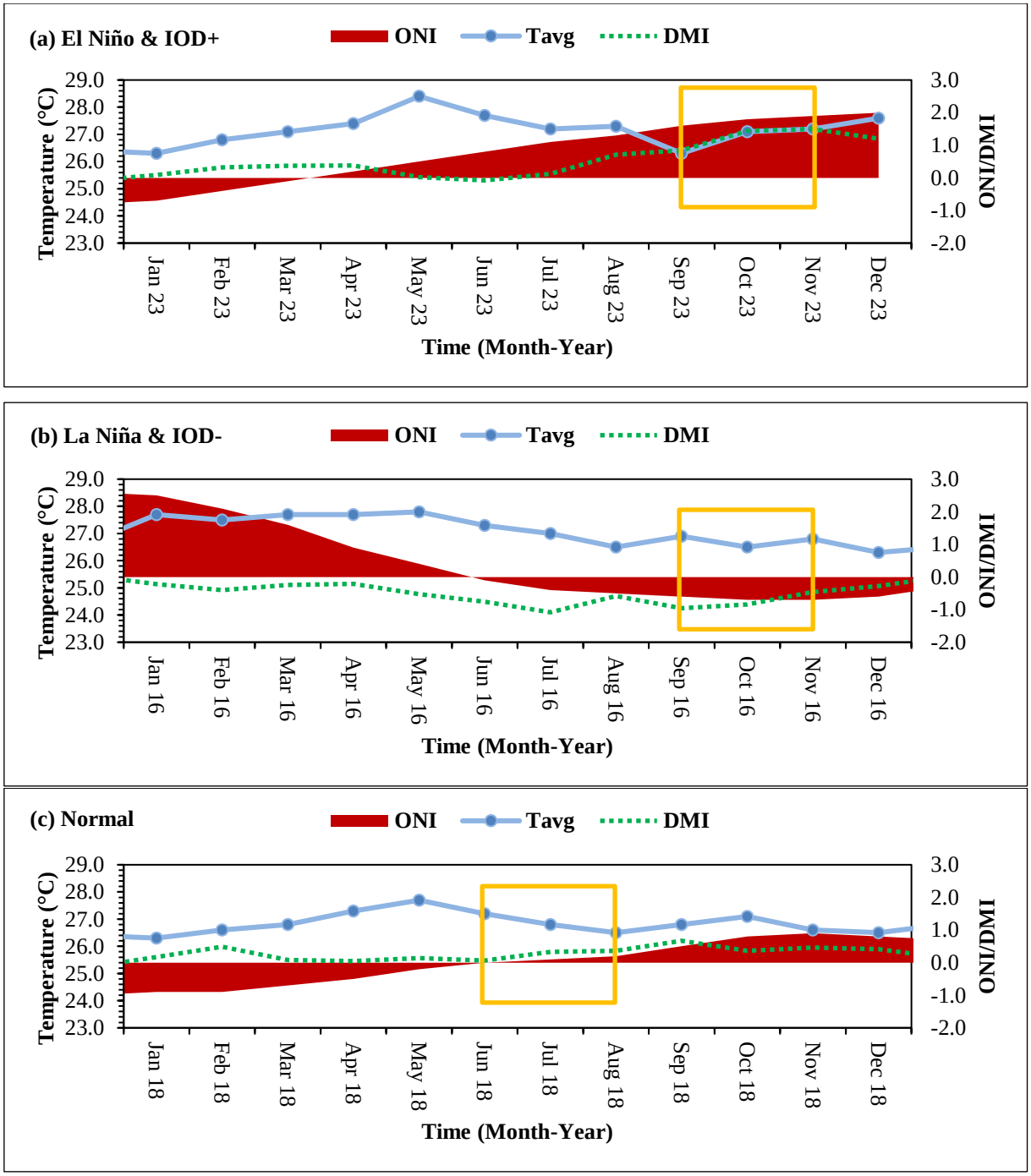

Figure 7. Average Air Temperature Trends During (a) El Niño and Positive IOD (Sep-Nov 2023), (b) La Niña and Negative IOD (Sep-Nov 2016), and (c) Normal Conditions (Jun-Aug 2018) at Bengkulu Climatology Station

In Table 4, predicted average temperatures (T_{p-avg}) were calculated based on a multiple linear regression model using ONI and DMI as predictors (Equation 5). These estimates help illustrate how large-scale ocean-atmospheric interactions influence temperature, while acknowledging that regional and local processes also affect actual observations.

Conversely, the ONI- DMI- category occurred from September to November 2016, during which air temperatures were lower compared to normal conditions. In September, the average temperature was recorded at 26.9°C, slightly higher than in October, which saw a decrease to 26.5°C. By November, the average temperature rose again to 26.8°C, indicating that the effects of La Niña were still dominant but

began to weaken toward the end of the year. The graph in Figure 7b illustrates a more stable temperature trend compared to the El Niño period, though it remained lower than normal conditions.

The Normal category, which occurred from June to August 2018, exhibited more stable temperatures without the influence of El Niño or La Niña. The average temperature ranged from 26.5°C to 27.2°C, with a maximum temperature reaching 33.5°C in June. The absence of extreme temperature increases or decreases during this period indicates that atmospheric and oceanic conditions were in equilibrium. Figure 7c illustrates a more consistent temperature pattern compared to other extreme conditions.

From this classification, it can be concluded that ONI+ DMI+ has the greatest warming impact on air temperature in Bengkulu, while ONI- DMI- tends to lower temperatures. Meanwhile, the Normal category represents more stable conditions without significant temperature changes.

Correlation of Air Temperature with ONI land DMI

Correlation analysis using Equation (1) for Pearson correlation shows that ONI has a positive relationship with the average air temperature in Bengkulu, although it falls within the weak to moderate category (r = 0.29-0.32), while DMI exhibits a weaker correlation (r = 0.01-0.04). Multiple correlation using Equation (2) slightly enhances this relationship, with values of 0.31 at the Meteorological Station and 0.36 at the Climatology Station.

Minimum temperature exhibits a weaker correlation, with ONI ranging between 0.07–0.11, while DMI shows a negative association at Meteorological (-0.20) and near zero at Climatology (0.01). Multiple correlations using Equation (2) for minimum temperature remain low (0.28 in Meteorological and 0.10 in Climatology), indicating that local factors play a more dominant role. Conversely, maximum temperature has a stronger correlation with ONI (0.28 in Meteorological and 0.38 in Climatology), while its relationship with DMI remains weak (-0.03 to 0.07). The multiple correlation using Equation (2) for maximum temperature increases to 0.32 in Meteorological and 0.42 in Climatology, suggesting that the combination of ONI and DMI has a greater impact on maximum temperature.

To strengthen the statistical interpretation of the correlation analysis, a multiple linear regression was conducted using ONI and DMI as independent variables, with average air temperature as the dependent variable. Based on Equation (3), the regression model aims to identify the extent to which ENSO and IOD jointly contribute to variations in air temperature in Bengkulu.

At the Meteorological Station, the regression equation obtained is shown in Equation (4):

$$T_{\text{avg}} = 26.91 + 0.19(\text{ONI}) - 0.11(\text{DMI}) \quad (4)$$

The model yielded an R^2 value of 0.0965, indicating that approximately 9.7% of the variation in average air temperature can be explained by ONI and DMI. The coefficient for ONI was statistically significant (p < 0.001), showing a positive association with higher temperatures. In contrast, DMI showed a weaker negative influence (p = 0.077), suggesting that its contribution to temperature variation is less dominant and not statistically conclusive.

At Climatology Station, the regression result is presented in Equation (5):

$$T_{\text{avg}} = 26.79 + 0.20(\text{ONI}) - 0.10(\text{DMI}) \quad (5)$$

This model produced a slightly higher R^2 value of 0.1092. Again, ONI was found to have a significant positive effect (p <

0.001), whereas DMI remained statistically insignificant (p = 0.127). These results are consistent with the previous correlation findings, confirming that ENSO-particularly El Niño events-has a stronger influence on air temperature in Bengkulu compared to IOD. A summary of the regression statistics is presented in Table 5.

Although the regression model demonstrates a statistically significant relationship between ONI, DMI, and average air temperature, the differences between observed values (T_{avg}) and predicted values ($T_{\mathrm{p-avg}}$) are expected. This is because the model only includes large-scale ocean-atmospheric indices and does not account for local and regional climatic influences, such as humidity, cloud cover, local wind patterns, and land surface characteristics. Consequently, the predicted values are not intended for precise forecasting, but rather to illustrate the statistical contribution of ENSO and IOD in explaining air temperature variability in Bengkulu.

Overall, ONI has a greater influence on Bengkulu's air temperature compared to DMI, which tends to have a minor or statistically insignificant effect. This pattern is consistently observed in both the correlation and regression analyses. The regression results provide stronger statistical evidence: ONI was shown to have a significant positive influence on temperature, while DMI's effect was weaker and not significant at the 95% confidence level. Although the R^2 values in both regression models were relatively low-suggesting that other atmospheric factors, such as monsoonal wind patterns, likely play a more decisive role-the results confirm that ENSO, especially during El Niño events, remains a dominant driver of warming in Bengkulu. These correlation results are summarized in Table 6.

Table 5. Multiple linear regression summary for average air temperature with ONI and DMI.

Observation Station	Variable	Coefficient (β)	Std. Error	*t*-value	*p*-value
Meteorological	Intercept	26.91	0.07	384.4	<0.001
	ONI	0.19	0.05	4.12	<0.001
	DMI	-0.11	0.06	-1.78	0.077
	R^2	0.0965			
Climatology	Intercept	26.79	0.08	334.9	<0.001
	ONI	0.20	0.04	4.46	<0.001
	DMI	-0.10	0.06	-1.53	0.127
	R^2	0.1092			

Table 6. Pearson and Multiple correlation coefficients of ONI and DMI with air temperature.

Observation Station	*T*	Pearson Correlation		Multiple Correlation
		r ONI	*r* DMI	
Meteorological	*T*min	0.11	-0.20	0.28
	*T*avg	0.29	0.01	0.31
	*T*max	0.28	-0.03	0.32
Climatology	*T*min	0.07	0.01	0.10
	*T*avg	0.32	0.04	0.36
	*T*max	0.38	0.07	0.42

Table 7. Comparison of ENSO and IOD influence on air temperature in various regions.

Study	Location	Influence		Other Influencing Factors
		ENSO	IOD	
This Study	Bengkulu City	Dominant ($r = 0.28 - 0.38$)	Weak/Not Significant ($r = -0.03 - 0.07$)	Monsoon wind patterns, geographical factors.
Prasetyo et al. (2021)	Java Island	Not Significant ($r \approx 0$)	Moderate - Strong ($r = 0.42 - 0.77$)	Asian Monsoon, Indian Ocean influence.

This finding contrasts with the results of Prasetyo et al. (2021), who reported that IOD had a stronger correlation with air temperature fluctuations in Java, while ENSO showed no significant relationship. The discrepancy may be attributed to differences in regional atmospheric circulation; Java is more influenced by Indian Ocean dynamics and the Asian Monsoon, whereas Bengkulu-situated on Sumatra's western coast-is more directly affected by the Walker Circulation, particularly during El Niño phases. Therefore, the influence of climate variability on air temperature is inherently regional, shaped by both atmospheric conditions and geographical location. A broader comparison of this study with another research is presented in Table 7.

Conclusion

Over the past 20 years, Bengkulu City has experienced a steady increase in air temperature, with an annual warming trend of approximately 0.08-0.1°C. ENSO was found to have a stronger influence than IOD, particularly during El Niño phases that correlate with elevated maximum temperatures (r = 0.28-0.38). In contrast, minimum temperatures showed weaker correlations, suggesting that local atmospheric dynamics may play a more substantial role in nighttime cooling.

These findings are supported by multiple linear regression results, which showed that ONI has a statistically significant positive effect on average air temperature. At the same time, DMI's influence was weaker and not significant. Although the explained variance is modest (R^2 = 0.0965-0.1092), the regression model confirms ENSO-especially El Niño-as a dominant driver of temperature variability in Bengkulu.

The phase-based composite analysis further revealed that the highest average temperatures occurred during ONI+ DMI+ conditions, while the lowest were observed under ONI− DMI− phases. These findings underscore the synergistic impact of ENSO and IOD in modulating regional temperature variability, particularly during extreme climate phases.

The convergence of results across trend analysis, correlation, regression, and composite classification highlights the importance of incorporating real-time ENSO and IOD monitoring into local early warning systems. Adaptive measures-such as water resource management, rainwater harvesting, and reservoir optimization-are crucial to mitigate the prolonged dry seasons associated with El Niño. Future research should explore how regional warming affects agriculture, public health, and coastal ecosystems in Bengkulu. Developing predictive models that integrate ENSO and IOD indicators may significantly improve regional climate resilience and preparedness.

Acknowledgments

The authors would like to express their sincere gratitude to the Meteorology, Climatology, and Geophysics Agency (BMKG), especially the Fatmawati Soekarno Meteorological Station and Bengkulu Climatology Station, for providing air temperature data from 2004 to 2023. Appreciation is also extended to the National Oceanic and Atmospheric Administration (NOAA) for supplying the ONI and DMI data used in this study.

The authors sincerely thank the editor, reviewers, and proofreaders for their constructive feedback, which significantly contributed to improving this manuscript.

Special thanks are also given to the research team, technical staff, and colleagues at the Department of Physics, Faculty of Mathematics and Natural Sciences, University of Bengkulu, for their valuable support in equipment preparation, data

collection, and analysis throughout this research.

Author Contribution

Mardho Tillah Edkayasa: Developed the research concept and objectives, designed the methodology, and collected climate data from reliable sources. Conducted data processing and statistical analysis of temperature trends, including the impacts of ENSO and IOD, using Microsoft Excel. Performed Pearson correlation, multiple linear regression, and composite analysis to evaluate relationships between variables and identify anomalies in climate variability. Drafted the manuscript by integrating research findings with relevant literature and formulating the overall discussion.

Elfi Yuliza: Guided the journal writing process and the structure of academic writing, and critically reviewed and revised the manuscript to ensure its quality for publication.

Lizalidiawati: As the primary supervisor, provided intensive guidance throughout the research process, assisted in climatological analysis, and offered in-depth insights for interpreting the results.

Conflict of Interest

The authors declare no conflict of interest. The content of this manuscript has been reviewed and approved by all authors. They affirm that the material is original, has not been published previously, and is not under consideration for publication elsewhere.

References

Abudukade, S., Yang, F., Liu, Y., Mamtimin, A., Gao, J., Ma, M., Wang, W., Cui, Z., Wang, Y., Zhang, K., Song, M., & Zhang, J. (2023). Effects of Artificial Green Land on Land-Atmosphere Interactions in the Taklamakan Desert. *Land*, 12(8), 1541. https://doi.org/10.3390/land12081541

Akhsan, H., Irfan, M., & Iskandar, I. (2023). El Niño Southern Oscillation (ENSO), Indian Ocean Dipole (IOD), and the Rise of Extreme Temperatures in Eastern Sumatra: Exploring Climate Change Dynamics. *Jurnal Penelitian Pendidikan IPA*, 9(2), 600–608. https://doi.org/10.29303/jppipa.v9i2.3084

Andrian, L. G., Osman, M., & Vera, C. S. (2024). The role of the Indian Ocean Dipole in modulating the austral spring ENSO teleconnection to the Southern Hemisphere. *Weather and Climate Dynamics*, 5(4), 1505–1522. https://doi.org/10.5194/wcd-5-1505-2024

Ariska, M., Akhsan, H., Muslim, M., Romadoni, M., & Putriyani, F. S. (2022) 'Prediksi Perubahan Iklim Ekstrem di Kota Palembang dan Kaitannya dengan Fenomena El Niño-Southern Oscillation (ENSO) Berbasis Machine Learning', *JIPFRI (Jurnal Inovasi Pendidikan Fisika dan Riset Ilmiah)*, 6(2), 79–86. https://doi.org/10.30599/jipfri.v6i2.1611

Eboy, O. V., & Kemarau, R. A. (2023). Study Variability of the Land Surface Temperature of Land Cover during El Niño Southern Oscillation (ENSO) in a Tropical City. *Sustainability*, 15(11), 8886. https://doi.org/10.3390/su15118886

Ferreira, D. H. L., & Badinger, A. (2023). Study Over El Niño and La Niña Influence on Mean Temperature Trends and Precipitation in Brazilian Regions. *Revista Geointerações*, 7(1), 1–14. https://doi.org/10.59776/2526-3889.2023.4890

Hansen, J., Sato, M., Kharecha, P., von Schuckmann, K., Beerling, D. J., Cao, J., Marcott, S., Masson-

Delmotte, V., Prather, M. J., Rohling, E. J., Shakun, J., Smith, P., Lacis, A., Russell, G., & Ruedy, R. (2017). Young people's burden: Requirement of negative CO_2 emissions. *Earth System Dynamics*, 8(4), 577–616. https://doi.org/10.5194/esd-8-577-2017

IPCC (Intergovernmental Panel on Climate Change). (2021). *Global warming of 1.5°C*. https://www.ipcc.ch/site/assets/uploads/sites/2/2019/06/SR15_Full_Report_Low_Res.pdf

Ismail, M. R., A. Zakaria., & Susilo, G. E. (2020). Analisis pengaruh anomali iklim terhadap curah hujan di Provinsi Bengkulu. Rekayasa: Jurnal Ilmiah Fakultas Teknik Universitas Lampung, 24(1), 10–14. https://doi.org/10.23960/REKRJITS.V24I1.11.

Jiang, N., Zhu, C., Hu, Z-Z., McPhaden, M. J., Lian, T., Zhou, C., Qian, W., & Chen, D. (2025). El Niño and Sea Surface Temperature Pattern Effects Lead to Historically High Global Mean Surface Temperatures in 2023. *Geophysical Research Letters*, 52(2), e2024GL113733. https://doi.org/10.1029/2024gl113733

Kaboth-Bahr, S., Kern, O. A., & Bahr, A. (2024). Developing a 3.5-million-year benchmark record of Indian Ocean Dipole variability. *EGU General Assembly 2024*, Vienna, Austria, 14–19 Apr 2024, EGU24-12377. https://doi.org/10.5194/egusphere-egu24-12377

Kong, Y. S. (2025). The Relationship Between Urban Morphology and the Urban Heat Island Effect: A Study of Cooling Strategies in Urbanized Areas. *Applied and Computational Engineering*, 122(1), 77–82. https://doi.org/10.54254/2755-2721/2025.19604

Liu, G., Guo, Y., Xia, H., Liu, X., Song, H., Yang, J., & Zhang, Y. (2024). Increase Asymmetric Warming Rates Between Daytime and Nighttime Temperatures Over Global Land During Recent Decades. *Geophysical Research Letters*, 51(24), e2024GL112832. https://doi.org/10.1029/2024gl112832

Loeb, N. G., Ham, S-H., Allan, R. P., Thorsen, T. J., Meyssignac, B., Kato, S., Johnson, G. C., & Lyman, J. M. (2024). Observational Assessment of Changes in Earth's Energy Imbalance Since 2000. *Surveys in Geophysics*, 45, 1757–1783. https://doi.org/10.1007/s10712-024-09838-8

McPhaden, M. J., Hasan, N., & Chikamoto, Y. (2023). Causes and Consequences of the Prolonged 2020-2023 La Niña. *EGU General Assembly 2023*, Vienna, Austria, 24–28 Apr 2023, EGU23-10801, https://doi.org/10.5194/egusphere-egu23-10801

Marathe, S., & Karumuri, A. (2021). Chapter 4 – The El Niño Modoki. In S. K. Behera, *Tropical and Extratropical Air-Sea Interactions; Modes of Climate Variations* (pp. 93–114). Elsevier. https://doi.org/10.1016/B978-0-12-818156-0.00009-5

Millenia, Y. W., Helmi, M., & Maslukah, L. (2023). Analisis Mekanisme Pengaruh IOD, ENSO dan Monsun terhadap Suhu Permukaan Laut dan Curah Hujan di Perairan Kepulauan Mentawai, Sumatera Barat. *Indonesian Journal of Oceanography*, 4(4), 87–98. https://doi.org/10.14710/ijoce.v4i4.14414

Mishra, V., Tiwari, A. D., & Kumar, R. (2022). Warming climate and ENSO variability enhance the risk of sequential extremes in India. *One Earth*, 5(11), 1250–1259.

https://doi.org/10.1016/j.oneear.2022.10.013

Najarzadeh, D. (2020). Conservative confidence intervals on multiple correlation coefficient for high-dimensional elliptical data using random projection methodology. *Journal of Applied Statistics*, 49(1), 64–85. https://doi.org/10.1080/02664763.2020.1796937

Nasution, C. N., Fajary, F. R., Abdillah, M. R., & Kartadikaria, A. R. (2023). Significant Precipitation Anomalies over Indonesia in the Aftermath of Iod Events. *IOP Conference Series: Earth and Environmental Science*, 1245, 012032. https://doi.org/10.1088/1755-1315/1245/1/012032

Novianti, L., Safrina, S., Satya, O. C., Hadi, H., Affandi, A. K., Virgo, F., & Irwan, M. (2023). Dampak Enso Dan IOD Terhadap Dinamika Kelembaban Udara dan Temperatur di Kota Palembang Pada Tahun 2017-2021. *Jurnal Penelitian Sains*, 25(1), 67–72. https://doi.org/10.56064/jps.v25i1.783

Pillai, P. A., Kiran, V. G., & Suneeth, K. V. (2024). The strengthened role of new predictors of Indian Ocean Dipole (IOD) during the recent decades of weakened ENSO-IOD relationship. *Dynamics of Atmospheres and Oceans*, 106, 101432. https://doi.org/10.1016/j.dynatmoce.2023.101432

Prasetyo, S., Hidayat, U., Haryanto, Y. D., & Riama, N. F. (2021). Karakteristik Suhu Udara di Pulau Jawa Kaitannya dengan Kelembapan Udara, Curah Hujan, SOI, dan DMI. *Jurnal Geografi, Edukasi dan Lingkungan*, 5(1), 15–26. https://doi.org/10.22236/jgel.v5i1.5971

Purohit, S. (2024). The Role of Urban Green Spaces in Mitigating Urban Heat Island Effect Amidst Climate Change. *Research Journal of Chemistry and Environment*, 29(1), 75–84. https://doi.org/10.25303/291rjce075084

Stuivenvolt-Allen, J., Fedorov, A. V., Fu, M., & Heede, U. (2024). Widening of wind-stress anomalies amplifies ENSO in a warming climate. *Journal of Climate*, 38, 497–512. https://doi.org/10.1175/JCLI-D-24-0126.1

Tan, S. (2024). The Effects of Climate Change on the Global Meteorological System and Trend Analysis. *Interdisciplinary Humanities and Communication Studies*, 1(7), 1–6. https://doi.org/10.61173/7b26qs93

Turney, S. (2024). *Pearson correlation coefficient (r): Guide & examples*. https://www.scribbr.com/statistics/pearson-correlation-coefficient/

Wardani, A., Akbar, A. J., Handayani, L., & Lubis, A. M. (2023). Correlation Among Rainfall, Humidity, and The El Niño-Southern Oscillation (ENSO) Phenomena in Bengkulu City During the Period from 1985-2020. *Jurnal Penelitian Pendidikan IPA*, 9(4), 1664–1671. https://doi.org/10.29303/jppipa.v9i4.2971

Xia, Y., Sun, X-G., Yan, Y., Feng, W-Y., Huang, F., & Yang, X-Q. (2017). Change of ENSO characteristics in response to global warming. *Chinese Science Bulletin*, 62(16), 1738–1751. https://doi.org/10.1360/N972016-01225

Xiao, H.-M., Lo, M.-H., & Yu, J-Y. (2022). The increased frequency of combined El Niño and positive IOD events since 1965s and its impacts on maritime continent hydroclimates. *Science Reports*, 12(1), 7532. https://doi.org/10.1038/s41598-022-11663-1

Yu, J.-Y., Wang, X., Yang, S., Paek, H., & Chen, M. (2017). The Changing El

Niño–Southern Oscillation and Associated Climate Extremes. In S.-Y. S. Wang, J-H. Yoon, C. C. Funk, R. R. Gillies. *Climate Extremes: Patterns and Mechanisms* (pp. 1–38). American Geophysical Union (AGU). https://doi.org/10.1002/9781119068020.CH1

Yuniasih, B., Harahap, W. N., & Wardana, D. A. S. (2022). Anomali Iklim El Nino dan La Nina di Indonesia pada 2013-2022. *Agroista Jurnal Agroteknologi*, 6(2), 136–143. https://doi.org/10.55180/agi.v6i2.332

Zaini, A. Z. A., Vonnisa, M., & Marzuki, M. (2024). Impact of different ENSO positions and Indian Ocean Dipole events on Indonesian rainfall. *Vietnam Journal of Earth Sciences*, 46(1), 100–119. https://doi.org/10.15625/2615-9783/19926

Zheng, Y., Tam, C-Y., & Collins, M. (2024). Reduced Indian Ocean Dipole Asymmetry and Increased Extreme Negative Events under Future Greenhouse Warming. *Journal of Climate*, 37, 5507–5523. https://doi.org/10.1175/JCLI-D-24-0107.1

Zhong, S., Zhang, Y., & Jiang, L. (2024). Impact of different types of La Niña development on the precipitation in the Maritime Continent. *Atmosphere-Ocean* 62(3), 254–267. https://doi.org/10.1080/07055900.2024.2326611

ISSN: 2579-5821 (Print)
ISSN: 2579-5546 (Online)
URL address: http://journal.unhas.ac.id/index.php/geocelebes
DOI: 10.70561/geocelebes.v9i1.43451

Jurnal Geocelebes Vol. 9 No. 1, April 2025, 78 – 86

Application of 2D Seismic Modeling in Gas Hydrate Reservoir Characterization

Welayaturromadhona[1]*, How-Wei Chen[2]

[1]Petroleum Engineering, Universitas Jember, Jember 68121, Indonesia
[2]College of Earth Sciences, National Central University, Zhongli, 320317, Taiwan

*Corresponding author. Email: wela@unej.ac.id

Manuscript received: 18 March 2025; Received in revised form: 25 April 2025; Accepted: 30 April 2025

Abstract

Gas hydrate reservoirs represent a significant unconventional energy resource with considerable potential for future energy supply and climate-related studies. However, their complex subsurface occurrence requires advanced geophysical methods for accurate detection and characterization. This study presents the application of two-dimensional (2D) seismic modeling to evaluate the seismic response of gas hydrate-bearing sediments and underlying free gas zones. The objective is to assess the reflection coefficients and amplitude variation with offset (AVO) to enhance the interpretation of subsurface features. The synthetic model is constructed using multichannel seismic data and velocity profiles derived from previous studies. Seismic wave propagation is simulated to observe the impedance contrasts across various subsurface layers. Results reveal that the Bottom Simulating Reflector (BSR), a key seismic indicator of gas hydrate presence, exhibits strong negative reflection amplitudes due to the presence of underlying free gas, which significantly reduces seismic velocity. Furthermore, AVO analysis shows that amplitude variations are highly sensitive to the acoustic impedance contrast at the hydrate-gas interface. These findings demonstrate the effectiveness of seismic modeling in improving gas hydrate reservoir characterization and provide a foundation for more accurate exploration strategies. The study contributes to both energy development and environmental monitoring efforts involving gas hydrates.

Keywords: AVO analysis; BSR; gas hydrate; geophysical exploration; seismic modeling.

Citation: Welayaturromadhona, W., & Chen, H-W. (2025). Application of 2D Seismic Modeling in Gas Hydrate Reservoir Characterization. *Jurnal Geocelebes*, 9(1): 78–86, doi: 10.70561/geocelebes.v9i1.43451

Introduction

Under high pressure and low temperature, gas molecules, mostly methane, are encased in a water lattice to form crystalline solids known as gas hydrates (Ruppel & Waite, 2020; Jin et al., 2022). They are usually found in areas with permafrost and marine deposits, where the climate keeps them stable (Ruppel & Kessler, 2017; Zhao, 2020). These hydrates have garnered interest because of their potential to contribute to climate change as a source of energy. Their study is essential for energy security and environmental monitoring since they are large methane reservoirs whose destabilization could result in large greenhouse gas emissions (Yu et al, 2021).

In geophysical terms, seismic techniques are frequently used to detect gas hydrates, and one important indicator is the Bottom Simulating Reflector (BSR). According to Neves et al. (2022) and Zhang et al. (2020), the BSR is a characteristic seismic reflection that happens at the border between hydrate-laden sediments and underlying free gas zones. There is a significant impedance contrast when gas hydrates are present because they change the subsurface elastic characteristics, raising seismic wave velocities, while the free gas zones below lower these speeds

(Wang et al., 2021; Waite et al., 2009). The inability of conventional seismic interpretation methods to distinguish hydrate accumulations from other geological formations, however, can result in reservoir calculation errors (Liu et al., 2021; Xing et al., 2018; Zhang et al., 2020).

To address these challenges, advanced seismic modeling techniques, such as two-dimensional (2D) seismic modeling, have been employed to enhance gas hydrate reservoir characterization. These methods simulate wave propagation through hydrate-bearing sediments and assess key seismic attributes like reflection coefficients and Amplitude Versus Offset (AVO) responses (Ecker et al., 1998; Liang, et al., 2020; Qian, et al., 2022). This approach offers a more detailed understanding of hydrate distribution and their effect on seismic wave behavior, aiding in more accurate reservoir characterization.

This study investigates the application of 2D seismic modeling in characterizing gas hydrate reservoirs, focusing on analyzing reflection amplitude variations and AVO attributes to improve the reliability of seismic interpretation. The findings aim to enhance current gas hydrate exploration techniques and contribute to the development of geophysical methodologies for assessing unconventional resources.

Although research on gas hydrate detection using seismic methods is increasing, there is still a gap in integrating detailed two-dimensional (2D) seismic modeling with amplitude variation with offset (AVO) analysis. Previous studies have often used simplified models or focused only on either seismic modeling or AVO analysis, without fully combining both techniques in a controlled synthetic setting. This study addresses this gap by developing a detailed 2D seismic model of a gas hydrate reservoir and simulating seismic responses to study AVO characteristics, aiming to improve the understanding of gas hydrate indicators such as bottom simulating reflectors (BSRs) and their elastic property contrasts.

The results of this research are crucial for improving gas hydrate detection, which can directly impact future exploration and drilling safety by providing more accurate assessments of reservoir properties and reducing risks associated with gas hydrate-related hazards

Materials and Methods

The wave equation, which comes from Hooke's law of elasticity and Newton's second law of motion, is used to model the propagation of seismic waves. A two-dimensional (2D) seismic model was created for this study to examine the seismic response of sediments that contain gas hydrate. To mimic wave behavior in various subsurface layers, the model includes important elastic parameters such as density (ρ), S-wave velocity (Vs), and P-wave velocity (Vp).

Mathematically, the propagation of seismic waves can be described by solving the wave equation, which is based on two fundamental laws of physics: Newton’s second law of motion ($F = m.a$) and Hooke’s law of elasticity (related to stress and deformation). Properties of an isotropic elastic medium are described by three spatial-varying parameters: compression-wave velocity $Vp(x_1,x_3)$, shear-wave velocity $Vs(x_1,x_3)$ and density $\rho(x_1,x_3)$. These parameters are functions of the elastic constants and determine the propagation behavior of P-waves and S-waves in the subsurface.

Aki – Richards' approximation explains how seismic amplitudes change with rock qualities and incidence angles, was used to estimate the reflection coefficient. Furthermore, amplitude fluctuations as a function of offset were evaluated using AVO analysis, which shed light on the

existence of free gas zones and gas hydrates. Figure 1 shows the layer model, while Table 1 shows the parameters used in the numerical simulation.

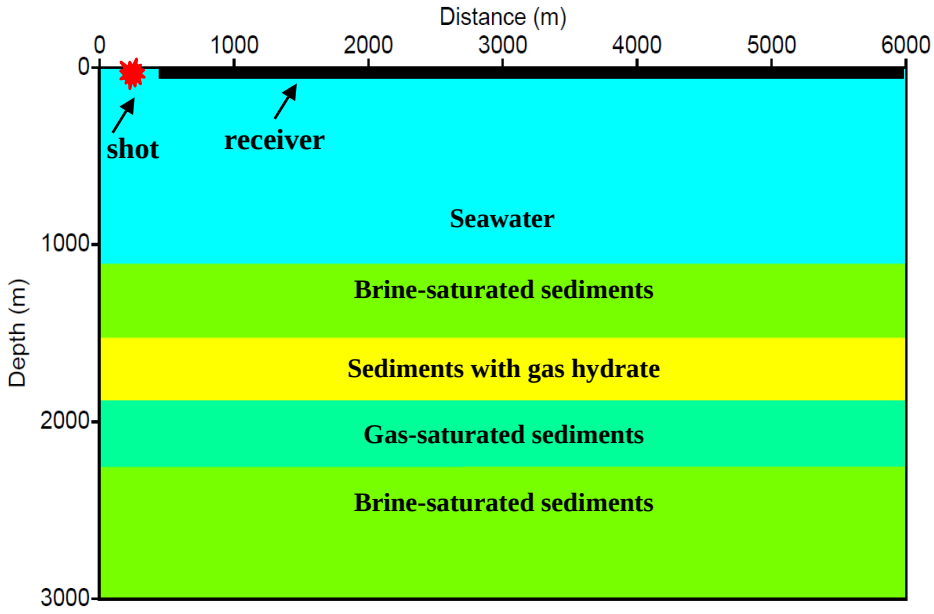

Figure 1: Layer model.

Table 1. The model parameters.

Model parameter	P-wave Vp (km/s)	S-wave Vs (km/s)	Density ρ (g/cm^3)	Poisson's ratio σ
Seawater	1.50	0.00	1.00	0.5
Brine-saturated sediments	2.37	1.10	2.17	0.36
Sediments with gas hydrate	2.70	1.11	2.11	0.39
Gas-saturated sediments	1.74	1.13	2.05	0.13
Brine-saturated sediments	2.37	1.10	2.17	0.36

We modelled the seafloor reflection to provide precise reference calibration. Assuming a seabed velocity of 1.5 km/s, the Poisson's ratio for deep-sea sediments was calculated to be 0.5 using Hamilton's (1979) work and Castagna et al.'s (1985) empirical correlation between Poisson's ratio and P-wave velocity (Vp). While gas-saturated sediments have a velocity of 1.74 km/s, the chosen velocity for sediments carrying gas hydrates is roughly 2.7 km/s. The synthetic seismogram produced for a 6 km receiver streamer with 468 channels separated by 12.5 m is shown in Figure 2. The depths of the source and receiver are 8 and 9 meters, respectively. The overall recorded wave duration is 4 seconds with a sample interval of 2 ms, using a Ricker wavelet with a dominant frequency of 20 Hz.

We analyzed the changes in reflection coefficients by varying Vp and Vs values to determine how gas saturation influences seismic amplitude. This approach provides a quantitative method to characterize gas hydrate reservoirs and distinguish them from surrounding sediments.

Results and Discussion

The border of the hydrate-bearing sediment generates a high-amplitude reflection because changes in elastic impedance (the

product of velocity and density) determine the strength of the reflected signal. The BSR is a special kind of seismic reflector that lies parallel to the seafloor and has the opposite polarity from the seafloor reflection.

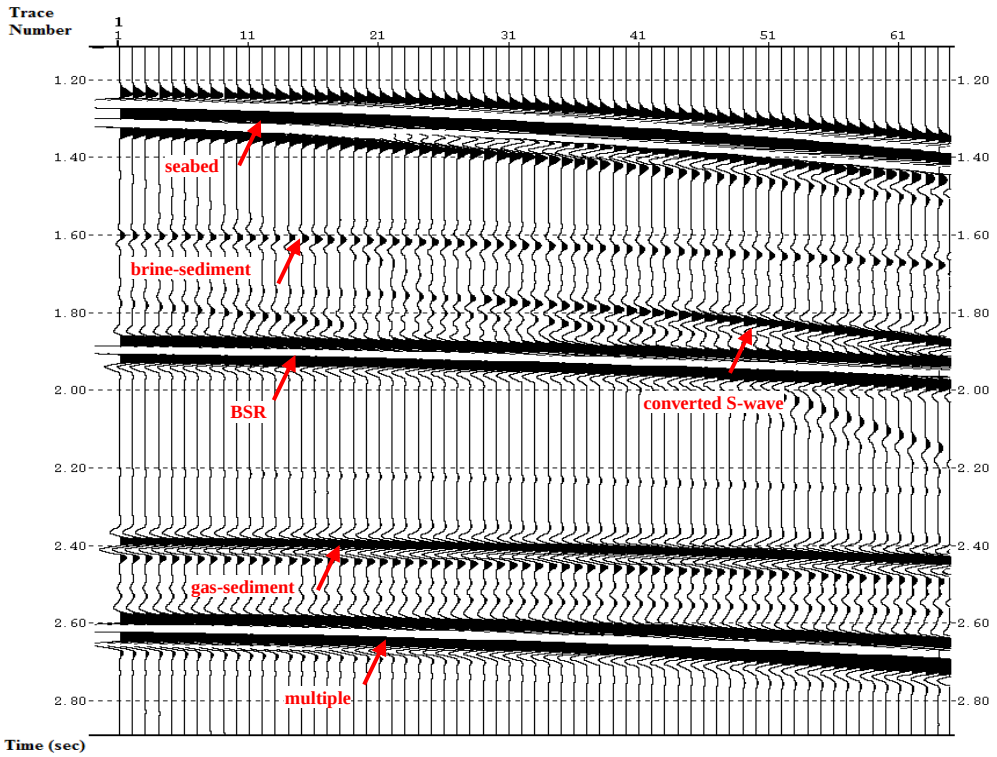

Figure 2. Synthetic seismograms for models with free gas and gas hydrates.

The BSR represents an interface where elastic impedance decreases. A higher P-wave velocity above the BSR and an abnormally low S-wave velocity in comparison to the underlying layer are the causes of this phenomena (Xing et al., 2018; Hakimi et al., 2016, Zhang et al 2015). A substantial velocity contrast is suggested by the large reflection amplitude just under the hydrate layer, which could point to the existence of a free gas layer.

Elastic isotropic circumstances were used to measure and assess the BSR's reflection coefficient to better understand this behavior. For comparison, we also used the Aki and Richards approximation to determine the reflection coefficient, and Figure 3 shows the AVO response for gas-bearing sediments. The findings show that there is an increasing amplitude in the absolute values of the gas-saturated sediment curve. Important markers of free gas at an interface can be found in variations in reflection amplitude with offset or incidence angle (Kim et al., 2020; Ryu & Riedel, 2017).

Reflection amplitudes grow more negative as the incidence angle or offset increases when hydrate-bearing sediments with a normal Poisson's ratio give way to an underlying gas-bearing sediment with a reduced Poisson's ratio (Minshull & White, 1989). Shear velocity (Vs), compressional velocity (Vp), and density distribution all affect the amplitude of BSR reflections as a function of source-receiver offset, but Poisson's ratio contrast is the main determinant of AVO behavior.

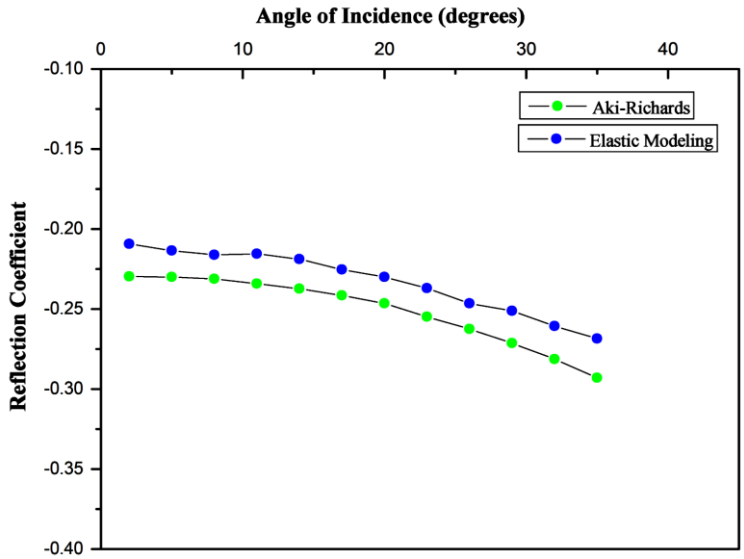

Figure 3. The BSR's reflection coefficients (RC). As the incidence angle rises, the RC shows a downward trend. According to Aki-Richard's theory, the layer-over-half-space model's predicted RC seems to be understated. A 0.02 scaling factor is used.

According to the established model, the P-wave velocity (Vp) of gas-saturated sediment is approximately 1.74 km/s, whereas the Vp of hydrate-bearing sediment is around 2.7 km/s. Above the hydrate layer and below the gas-saturated sediment, the surrounding lithology is composed of brine-saturated sediments with a Vp of approximately 2.37 km/s (Ecker et al., 1998). To examine how velocity variations affect the reflection coefficient, Vp and shear-wave velocity (Vs) were adjusted independently. Initially, Vp was altered by increasing or decreasing it by 5%, 25%, and 65%, and the reflection coefficient was computed using Aki and Richards' approximation. The findings indicate that a rise in Vp results in a lower reflection coefficient, while a reduction in Vp leads to a higher (more negative) reflection coefficient as shown in Figure 4. A comparable pattern emerges when both Vp and Vs are simultaneously adjusted (Figure 5). Increasing Vp and Vs leads to a decrease in the reflection coefficient, whereas decreasing them causes the coefficient to rise (becoming more negative). This analysis helps to understand how variations in Vp and Vs influence reflection coefficients, providing valuable insights for interpreting seismic data related to gas hydrates.

By showing amplitude fluctuations with increasing offset, AVO study provides additional evidence for the identification of gas hydrates and underlying free gas. The hydrate-bearing sediments produce a moderate increase in reflection amplitude, whereas the free gas zone exhibits a strong AVO response, characterized by an increasing amplitude trend with offset. These results are consistent with established AVO classification models for gas-saturated sediments. The strong AVO response confirms that gas hydrate reservoirs can be effectively distinguished using amplitude-based seismic attributes. The observed amplitude variation provides valuable insights into subsurface fluid distribution, supporting the interpretation that free gas accumulations exist beneath the hydrate layer.

These findings highlight the effectiveness of 2D seismic modeling in characterizing gas hydrate reservoirs. The identification of strong BSR reflections and AVO anomalies confirms that seismic attributes serve as reliable indicators for gas hydrate deposits. This is particularly relevant for exploration

strategies aimed at assessing gas hydrate potential as an alternative energy resource. Furthermore, distinguishing hydrate-bearing sediments from free gas zones is crucial for risk assessment in offshore drilling operations, as understanding the seismic response of gas hydrates helps mitigate potential hazards associated with gas release and sediment destabilization.

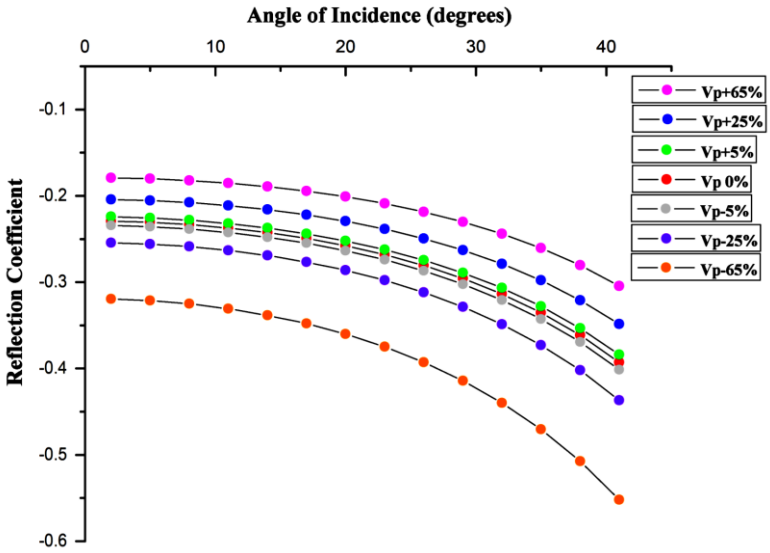

Figure 4. Reflection coefficient values fluctuate in response to variations in P-wave velocity (Vp). The Vp is adjusted by -65%, -25%, -5%, 0%, +5%, +25%, and +65%. An increase in Vp results in a lower reflection coefficient, whereas a decrease in Vp leads to a higher (more negative) reflection coefficient.

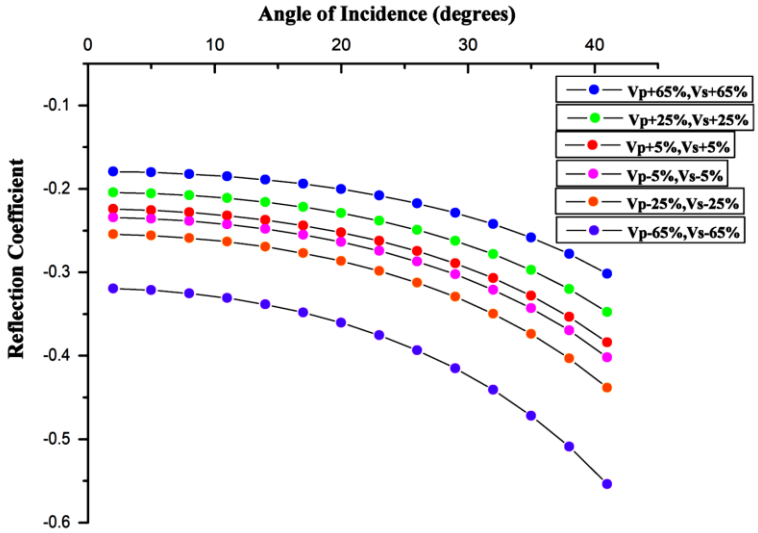

Figure 5. Reflection coefficient values in response to changes in both Vp and Vs. An increase in Vp and Vs results in a lower reflection coefficient, while a decrease in these parameters leads to a higher (more negative) reflection coefficient.

Despite the promising results, some limitations should be acknowledged. The models used in this study assume an idealized layer structure and do not account for heterogeneities in hydrate distribution. Future research should incorporate 3D seismic analysis and field validation using well-log data to improve accuracy. Expanding these methodologies will enhance the reliability of gas hydrate exploration and contribute to a deeper understanding of its potential as an energy resource.

Conclusion

The usefulness of 2D seismic modelling in describing gas hydrate reservoirs and differentiating them from underlying free gas zones is demonstrated in this work. The findings demonstrate that the Bottom Simulating Reflector (BSR), which shows a clear negative amplitude anomaly because of the impedance differential between hydrate-bearing sediments and free gas zones, is a powerful seismic indication of the existence of gas hydrate.

The reflection coefficient analysis shows that increasing P-wave velocity (Vp) reduces the reflection coefficient, while decreasing Vp increases it, making free gas zones more prominent in seismic sections. A similar trend is observed when Vp and S-wave velocity (Vs) are modified together, reinforcing the importance of velocity contrasts in hydrate identification. Additionally, Amplitude Versus Offset (AVO) analysis reveals that hydrate-bearing sediments exhibit moderate amplitude variations, whereas free gas zones produce a strong AVO response, confirming the applicability of AVO attributes in gas hydrate exploration.

These findings highlight the importance of seismic attributes in improving the reliability of gas hydrate detection and reservoir characterization. The ability to differentiate hydrate-bearing sediments from gas-saturated layers is particularly crucial for energy resource assessment and risk mitigation in offshore drilling operations.

Despite the promising results, this study has some limitations. The seismic model assumes an idealized layered structure, which does not fully account for natural heterogeneities in gas hydrate distribution

Acknowledgments

The authors would like to thank all colleagues and collaborators who provided valuable input and encouragement throughout this study. We express our gratitude to the Computational Seismology Research Group, National Central University Taiwan, for providing essential field data that significantly improved the accuracy and reliability of the seismic modeling. We also appreciate the continuous guidance and constructive feedback from our academic supervisor, which played a crucial role in the preparation of this manuscript.

Author Contribution

The first author conducted the research, including conceptualization, seismic modeling, data analysis, and manuscript preparation. Field data provided by the second author, made a significant contribution to the interpretation of the results. The authors also received valuable guidance and feedback from supervisors, which helped to improve the study. All aspects of the research and writing were completed independently by the authors.

Conflict of Interest

Regarding this research, the author states that there are no conflicts of interest. The results, analysis, and conclusions of this study have not been impacted by any financial or personal ties to any organizations or people.

References

Castagna, J. P., Batzle, M. L., & Eastwood, R. L. (1985). Relationship between compressional-wave and shear-wave velocities in clastic silicate rocks. *Geophysics*, 50(4), 571–581. https://doi.org/10.1190/1.1441933

Ecker, C., Dvorkin, J., & Nur, A. (1998). Sediments with gas hydrates: Internal structure from seismic AVO.

Geophysics, 63(5), 1659–1669. https://doi.org/10.1190/1.1444462

Hakimi, M. H., Abdullah, W. H., Mohialdeen, I. M. J., Makeen, M. Y., & Mustapha, K. A. (2016). Petroleum generation characteristics of heterogeneous source rock from Chia Gara formation in the Kurdistan region, northern Iraq as inferred by bulk and quantitative pyrolysis techniques. Marine and Petroleum Geology, 71, 260–270. https://doi.org/10.1016/j.marpetgeo.2016.01.003

Hamilton, E. L. (1979). Sound velocity gradients in marine sediments. *Journal of the Acoustical Society of America*, 65(4), 909–922. https://doi.org/10.1121/1.382594

Jin, J., Wang, X., Zhang, Z., He, M., Magee, C., Li, J., Li, Y., Li, S., Luan, Z., Zhang, G., & Sun, L. (2022). Shallow gas and gas hydrate accumulations influenced by magmatic complexes in the Pearl River Mouth Basin, South China Sea. *Marine Geology*, 453, 106928. https://doi.org/10.1016/j.margeo.2022.106928

Kim, Y-J., Cheong, S., Chun, J-H., Cukur, D, Kim, S-P., Kim, J-K., & Kim, B-Y. (2020). Identification of shallow gas by seismic data and AVO processing: Example from the southwestern continental shelf of the Ulleung Basin, East Sea, Korea. *Marine and Petroleum Geology*, 117, 104346. https://doi.org/10.1016/j.marpetgeo.2020.104346

Liang, J-Q., Deng, W., Lu, J-A., Kuang, Z-G., He, Y-L., Zhang, W., Gong, Y-H, Liang, J., & Meng, M-M. (2020). A fast identification method based on the typical geophysical differences between submarine shallow carbonates and hydrate bearing sediments in the northern South China Sea. China Geology, 3(1), 16–27. https://doi.org/10.31035/cg2020021

Liu, L., Zhang, X., & Wang, X. (2021). Wave propagation characteristics in gas hydrate-bearing sediments and estimation of hydrate saturation. *Energies*, 14(4), 804. https://doi.org/10.3390/en14040804

Neves, E. H. P., Silva, C. G., Matsumoto, R., & Freire, A. F. M. (2022). Analysis of seismic attributes to enhance a Bottom Simulating Reflector (BSR) in the gas hydrate area of Umitaka Spur, eastern margin of Japan Sea. *Brazilian Journal of Geophysics*, 40(3), 1–17. http://dx.doi.org/10.22564/brjg.v40i3.2179

Qian, J., Kang, D., Jin, J., Lin, L., Guo, Y., Meng, M., Wang, Z., & Wang, X. (2022). Quantitative seismic characterization for gas hydrate-and free gas-bearing sediments in the Shenhu area, South China sea. *Marine and Petroleum Geology*, 139, 105606. https://doi.org/10.1016/j.marpetgeo.2022.105606

Ruppel, C. D., & Kessler, J. D. (2017). The interaction of climate change and methane hydrates. *Reviews of Geophysics*, 55(1), 126–168. https://doi.org/10.1002/2016RG000534

Ruppel, C. D., & Waite, W. F. (2020). Timescales and processes of methane hydrate formation and breakdown, with application to geologic systems. *Journal of Geophysical Research: Solid Earth*, 125(8), e2018JB016459. https://doi.org/10.1029/2018JB016459

Ryu, B-J., & Riedel, M. (2017) Gas hydrates in the Ulleung Basin, East Sea of Korea. *Terrestrial, Atmospheric and Oceanic Science*, 28, 943–963. https://doi.org/10.3319/TAO.2017.10.21.01

Waite, W. F., Santamarina, J. C., Cortes, D. D., Dugan, B., Espinoza, D. N., Germaine, J., Jang, J., Jung, J. W., Kneafsey, T. J., Shin, H., Soga, K., Winters, W. J., & Yun, T-S. (2009). Physical properties of hydrate-bearing sediments. *Reviews of Geophysics*,

47(4), RG4003. https://doi.org/10.1029/2008RG000279

Wang, W., Ba, J., Carcione, J. M., Liu, X., & Zhang, L. (2021). Wave properties of gas-hydrate bearing sediments based on effective medium theory. *Frontiers in Earth Science*, 9, 640424. https://doi.org/10.3389/feart.2021.640424

Xing, L., Liu, X., Zhang, J., Liu, H., Zhang, J., Li, Z., & Wang, J. (2018). Sensitivity analysis of P-waves and S-waves to gas hydrate in the Shenhu area using OBS. *Journal of Ocean University of China*, 17(1), 139–146. https://doi.org/10.1007/s11802-018-3587-6

Yu, Y. S., Zhang, X., Liu, J. W., Lee, Y., & Li, X. S. (2021). Natural gas hydrate resources and hydrate technologies: a review and analysis of the associated energy and global warming challenges. *Energy & Environmental Science*, 14(11), 5611–5668. https://doi.org/10.1039/D1EE02093E

Zhang, G., Liang, J., Lu, J. A., Yang, S., Zhang, M., Holland, M., Schultheiss, P., Su, X., Sha, Z., Xu, H., Gong, Y., Fu, S., Wang, L., & Kuang, Z. (2015). Geological features, controlling factors and potential prospects of the gas hydrate occurrence in the east part of the Pearl River Mouth Basin, South China Sea. *Marine and Petroleum Geology*, 67, 356-367. https://doi.org/10.1016/j.marpetgeo.2015.05.021

Zhang, W., Liang, J., Wei, J., Lu, J. A., Su, P., Lin, L., Huang, W., Guo, Y., Deng, W., Yang, X., & Wan, Z. (2020). Geological and geophysical features of and controls on occurrence and accumulation of gas hydrates in the first offshore gas-hydrate production test region in the Shenhu area, Northern South China Sea. *Marine and Petroleum Geology*, 114, 104191. https://doi.org/10.1016/j.marpetgeo.2019.104191

Zhao, J., Zheng, J. N., Ma, S., Song, Y., & Yang, M. (2020). Formation and production characteristics of methane hydrates from marine sediments in a core holder. *Applied Energy*, 275, 115393. https://doi.org/10.1016/j.apenergy.2020.115393

ISSN: 2579-5821 (Print)
ISSN: 2579-5546 (Online)
URL address: http://journal.unhas.ac.id/index.php/geocelebes
DOI: 10.70561/geocelebes.v9i1.43566

Jurnal Geocelebes Vol. 9 No. 1, April 2025, 87 – 99

Source Rock Evaluation in the "Idea" Field, Bintuni Basin, West Papua: A Geochemical Approach

Dea Ananda[1]*, Jamaluddin[2], Warto Utomo[3], Joko Wiyono[1], Baiq Maulinda Ulfah[1], Amiruddin[1], Nijusiho Manik[1], Abdi Suprayitno[2]

[1]Petroleum Engineering Study Program, Sekolah Tinggi Teknologi Migas Balikpapan, km. 8 Karang Joang, Balikpapan, 76127, Indonesia
[2]Geological Engineering Study Program, Sekolah Tinggi Teknologi Migas Balikpapan, km. 8 Karang Joang, Balikpapan, 76127, Indonesia
[3]Petroleum Engineering Study Program, Institut Teknologi Petroleum Balongan, Jl. Soekarno Hatta Pekandangan, Indramayu, 45216, Indonesia

*Corresponding author. Email: deaanandagau@gmail.com

Manuscript received: 21 March 2025; Received in revised form: 29 April 2025; Accepted: 30 April 2025

Abstract

The Bintuni Basin is one of the largest hydrocarbon-bearing basins in Eastern Indonesia, although only a limited number of oil and gas fields are currently. Consequently, further investigation into its petroleum system, particularly the potential of its source rocks. In hydrocarbon exploration, characterizing source rock is critical to evaluating the presence of organic-rich strata capable of generating hydrocarbons. Geochemical analysis is a widely used method for assessing source rock potential, utilizing total organic carbon (TOC), rock-eval pyrolysis, and vitrinite reflectance data. In this study, geochemical data were obtained from one well and two outcrop samples to evaluate the quantity, quality, and thermal maturity of organic matter. The geochemical assessment of rock samples from four stratigraphic formations indicates that the Permian Ainim Formation exhibits the highest source rock potential. TOC values range from 1% to 80% with hydrogen index (HI) values range between 13 and 431 mg HC/g TOC classifying the formation as a good to excellent potential. The dominant organic matter consists of kerogen type II/III suggesting the potential for both oil and gas generation. Thermal maturity analysis indicates that the Ainim formation has reached the oil and gas generation window at depths of 8,075–8,420 feet. These findings demonstrate that the Ainim Formation represents a significant source rock within the Bintuni Basin, contributing valuable insights into the region's petroleum system and hydrocarbon prospectivity.

Keywords: Bintuni Basin; Maturity; Quality; Quantity; Source rock.

Citation: Ananda, D., Jamaluddin, J., Utomo, W., Wiyono, J., Ulfah, B. M., Amiruddin, A., Manik, N., & Suprayitno, A. (2025). Source Rock Evaluation in the "Idea" Field, Bintuni Basin, West Papua: A Geochemical Approach. *Jurnal Geocelebes*, 9(1): 87–99, doi: 10.70561/geocelebes.v9i1.43566

Introduction

The Bintuni Basin located in West Papua Province, Indonesia is one of the most significant sedimentary basins in the region and has been proven to contribute substantially to the country's oil and gas production (Utomo et al., 2022). This basin has attracted considerable interest due to its complex geological history and its potential for hydrocarbon generation. Among the various stratigraphic units present, Permian-aged sediments particularly the Ainim Formation are believed to be the primary source rocks responsible for hydrocarbon generation in the basin.

Understanding the source rock characteristics is fundamental in petroleum system analysis as it provides critical insights into the quantity, quality, and thermal maturity of organic material—key factors determining the potential of hydrocarbon generation (Haris et al., 2017,

Jamaluddin et al., 2018; 2023; 2024a,b). Despite its proven petroleum potential, the Bintuni Basin has been the subject of limited comprehensive geochemical studies. This gap is particularly notable in source rock characterization. Therefore, this study aims to evaluate the source rock potential in the "Idea" Field by employing geochemical analysis, which includes total organic carbon (TOC) measurement, rock-eval pyrolysis, and vitrinite reflectance. These techniques provide a detailed assessment of the organic richness, kerogen type, and thermal maturity of the studied formations, particularly the Ainim Formation which has been identified as a promising source rock potential. While its petroleum potential has long been recognized, detailed studies focusing on geochemical characterization of source rocks are still relatively scarce.

Previous research on source rock characterization in the Bintuni Basin began with early works such as Alam & Setiadi (2019), highlighting the significance of Permian sedimentary sequences in hydrocarbon generation. Subsequent investigations have confirmed the basin's petroleum potential, particularly within pre-Tertiary and Tertiary formations. Recent technological advances have significantly improved the evaluation of source rock potential in complex basins like Bintuni.

Recent advancements in organic geochemistry and basin modeling have provided more sophisticated methods for evaluating source rock potential (Jamaluddin & Sea, 2018). Studies utilizing Rock-Eval Pyrolysis, TOC analysis, and Vitrinite Reflectance have proven effective in assessing the hydrocarbon-generating capability of sedimentary formations (Jamaluddin et al., 2018; 2025). Furthermore, advancements in petroleum geochemistry and thermal maturation studies have enhanced the ability to predict hydrocarbon expulsion and migration pathways (Hamzah et al., 2018; Indriyani et al., 2020; Syarifah et., 2021).

This research aims to bridge the gap in knowledge by applying geochemical analysis techniques to assess the Ainim Formation's source rock potential. By integrating geochemical data with regional geological insights, this study contributes to a better understanding of the petroleum system in the Bintuni Basin and provides valuable information for future exploration and resource assessment. The findings of this study are expected to support more efficient exploration strategies and enhance the basin modeling framework for the region.

Regional Geology

The Bintuni Basin, located in West Papua, Indonesia, is a prominent foreland basin renowned for its complex geology and significant hydrocarbon resources. Geologically, the basin sits at the northern margin of the Australian continental plate, adjacent to the Bird's Head (Vogelkop) region, and has been shaped by the dynamic interactions between the Australian, Pacific, and Eurasian tectonic plates (Harahap, 2012; Handyarso & Padmawidjaja, 2017; Alam & Setiadi, 2019). The basin's structural framework is characterized by major strike-slip and thrust faults, which have influenced its evolution through two main tectonic phases: an extensional phase from the Permian to the Late Oligocene, marked by rifting and subsidence, and a compressional phase from the Late Oligocene to the present, associated with uplift and the formation of structural traps, especially during the Miocene–Pliocene due to the activity of the Lengguru Fold and Thrust Belt (Sapiie et al., 2012; Haris et al., 2017).

The stratigraphy of the Bintuni Basin reflects a prolonged depositional history, beginning with the Kemum Formation (Silurian–Devonian), which forms the

metamorphic basement complex (Harahap, 2012) (Figure 1). This unit comprises dark slate, phyllite, metamorphic greywacke, quartzite, and conglomerate, interpreted as marine turbiditic deposits associated with a pre-Tethys rift system. Intruded by Devonian granites and affected by Hercynian orogeny during the Carboniferous–Permian, the Kemum Formation represents the basin's pre-rift tectonic phase (Nuarihidayah et al., 2022; Lelono et al., 2023).

Overlying the Kemum Formation is the Tipuma Formation (Triassic–Early Jurassic), a siliciclastic succession deposited in fluvial-deltaic environments. Composed of quartz-rich sandstones and carbonate-rich shales, this formation marks a transition to non-marine sedimentation following Permian–Triassic tectonic uplift and erosion. While the Tipuma Formation itself is primarily non-marine, its deposition preceded the Middle Jurassic shift to marine conditions in the region, which became pronounced in the overlying Lower Kembelangan Formation (Middle–Late Jurassic) (Nopiyanti et al., 2020; Nuarihidayah et al., 2022).

The transition to marine sedimentation accelerated during the Late Jurassic–Cretaceous, with deep-marine shales (e.g., Jass Formation) developing as regional caprocks (Nuarihidayah et al., 2022; Utomo et al., 2022). This stratigraphic progression-from metamorphic basement (Kemum Fm.) to fluvial clastics (Tipuma Fm.) and later marine deposits-highlights the basin's evolution through extensional rifting, subsidence, and subsequent compressional phases linked to the Lengguru Fold Belt (Sapiie et al., 2012).

During the Permian to Jurassic extensive carbonate platform development occurred, represented by the Ainim, Kembelangan, and Kopai Formations, which contain significant source and reservoir rocks (Sapiie et al., 2012). The basin was later influenced by Cretaceous to Paleogene tectonism, leading to subsidence and the deposition of deep marine sediments (Haris et al., 2017; Ustiawan et al., 2019). Subsequent Neogene compressional tectonics resulted in structural deformation, including folding and faulting, which played a crucial role in hydrocarbon trap formation (Winardi et al., 2014; Edmundo et al., 2021; Li et al., 2022).

The depositional environments in the basin range from fluvio-deltaic to carbonate platform settings, resulting in diverse reservoir and source rock facies. Structural traps, primarily related to folding and faulting from the Lengguru Belt, play a crucial role in hydrocarbon accumulation, while overlying shales and carbonates provide effective seals (Winardi et al., 2014; Edmundo et al., 2021). The combination of rich source rocks, excellent carbonate reservoirs, and well-developed traps and seals has made the Bintuni Basin one of Indonesia’s most important oil and gas provinces, with ongoing exploration and production activities targeting its prolific petroleum systems.

Materials and Methods

This study conducts a comprehensive geochemical evaluation of source rocks in the 'Idea' Field, Bintuni Basin, West Papua, using secondary data from PT Petroenergy Wiriagar KSO Pertamina EP Wiriagar (Figure 2). A total of 10 cutting samples and 36 outcrop samples were systematically collected and analyzed to evaluate their hydrocarbon generation potential. The sampling strategy was designed to ensure a representative distribution across different stratigraphic intervals and lithological units, including claystone, shale, and coal, thereby capturing the variability in organic richness, kerogen type, and thermal maturity (Hazra et al., 2019).

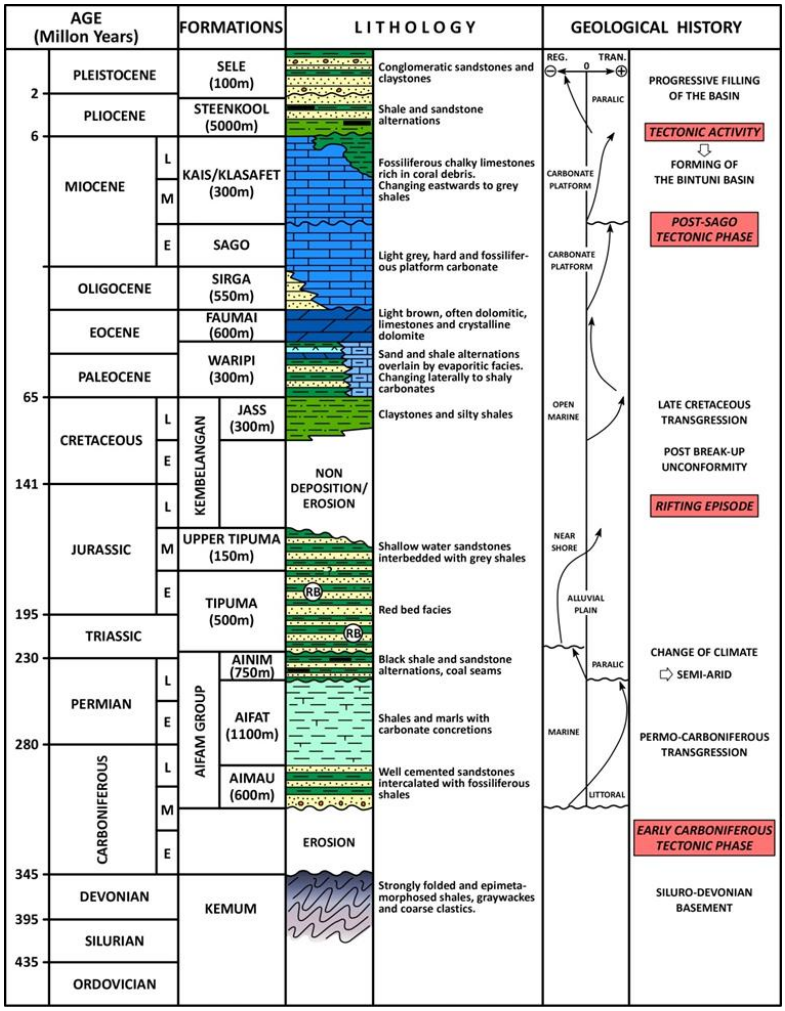

Figure 1. Stratigraphy of Bintuni Basin (Harahap, 2012).

The geochemical analysis commenced with Total Organic Carbon (TOC) determination to quantify the organic matter content within the samples. TOC is a fundamental parameter for evaluating source rock quality as it indicates the concentration of organic material that may generate hydrocarbons under suitable thermal conditions (Table 1). Following TOC analysis, rock-eval pyrolysis was conducted to obtain Hydrogen Index (HI) and T_{max} values. The HI provides insight into the type of organic matter present distinguishing between oil-prone, gas-prone, or inert kerogen, while T_{max}, the temperature at which the maximum release of hydrocarbons occurs during pyrolysis, serves as an indicator of the thermal maturity of the source rock.

Table 1. Geochemical Parameters Describing the Petroleum Potential (Quantity) of an Immature Source Rock (Jamaluddin et al., 2018).

Potential (Quality)	Organic Matter		
	TOC (wt.%)	Rock-Eval Pyrolysis	
		S_1	S_2
Poor	0 – 0.5	0 – 0.5	0 – 2.5
Fair	0.5 – 1	0.5 – 1	2.5 – 5
Good	1 – 4	1 – 2	5 – 10
Very Good	2 - 4	2 - 4	10 - 20
Excellent	> 4	> 4	> 20

Table 2. Geochemical Parameters Describing Level of Thermal Maturation (Jamaluddin & Sea, 2018)

Stage of thermal maturity	Maturation	
	Ro (%)	$T_{max.}$ (^{0}C)
Immature	0.2 – 0.6	< 435
Mature		
Early	0.6 – 0.65	435 – 445
Peak	0.65 – 0.9	445 – 450
Late	0.9 – 1.35	450 – 470
Postmature	> 1.35	> 470

To enhance the accuracy of thermal maturity assessments, petrographic analysis including vitrinite reflectance (VR) measurements was performed on selected samples (Table 2). Vitrinite reflectance is a widely accepted method for determining the level of organic matter maturation as it measures the percentage of light reflected from vitrinite particles in polished rock samples. This analysis provided additional confirmation of the thermal evolution of the source rocks complementing the T_{max} data from rock-eval pyrolysis.

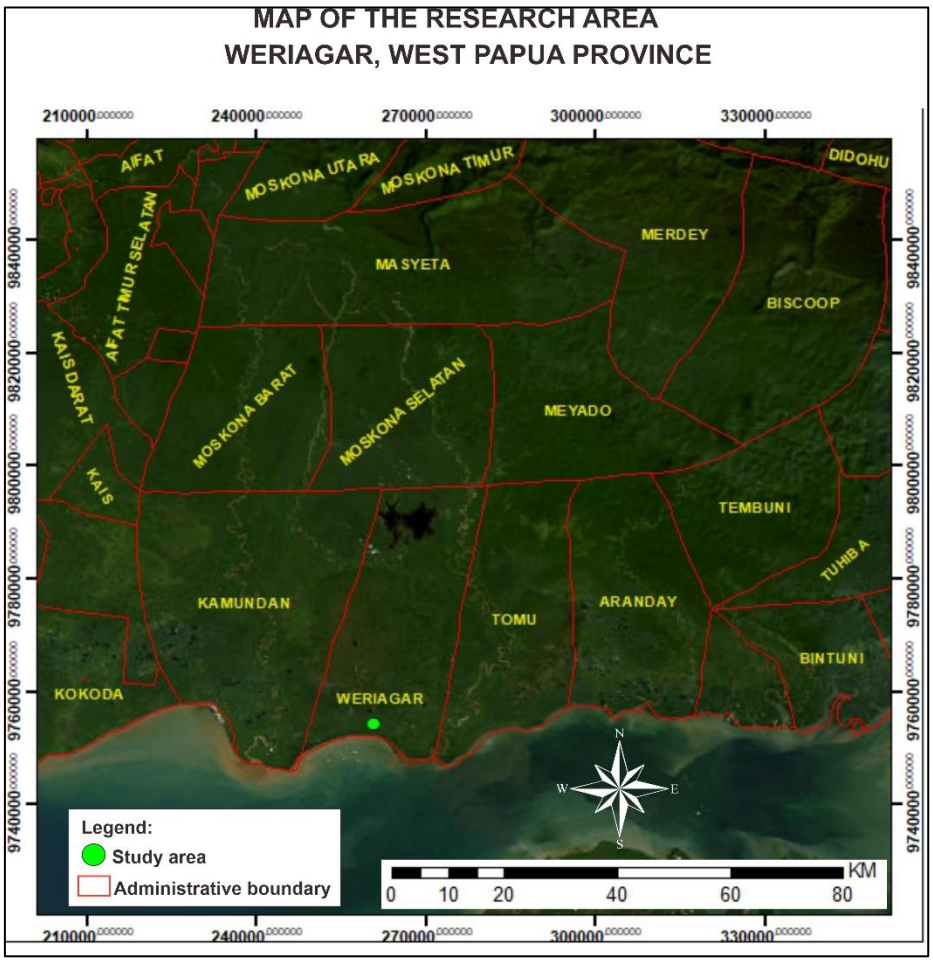

Figure 2. Location map of the research area in the Idea Field, Bintuni Basin, West Papua.

Results and Discussion

Organic matter richness and Petroleum generative potential

The geochemical evaluation of source rocks in the "Idea" Field, Bintuni Basin, West Papua, provides critical insights into the petroleum generation potential of the Ainim and Aifat Formations. The graph presents a relationship between TOC and Potential Yield (mg HC/g Rock), which are key parameters in assessing the quality of source rocks.

The TOC values indicate the richness of organic matter within the source rocks. In this study, coal samples exhibit the highest TOC values, ranging from 1.31 wt.% to 76.84 wt.% signifying excellent organic matter content. Shale samples have lower TOC values varying between 0.14 wt.% and 6.43 wt.%, while claystone shows the lowest TOC values, typically below 1.1 wt.% (Table 3). The presence of high TOC values in coal suggests a significant potential for hydrocarbon generation.

Table 3. Total Organic Carbon (TOC), Rock-Eval Pyrolysis, and Vitrinite Reflectance data for the analyzed samples

Samples	Lithology	TOC (wt.%)	Potential Yield (S_1+S_2)	$T_{max.}$ (°C)	Hydrogen Index (HI)	Vitrinite Reflectance (%Ro)	Formation
Cutting Samples	Coal	1.31	1.24	456	85	0.83	Ainim
	Coal	36.88	78.6	450	205	0.86	Ainim
	Coal	76.84	168.99	452	217	0.86	Ainim
	Claystone	1.22	0.41	455	25	0.86	Ainim
	Coal	53.66	161.23	453	294	0.86	Ainim
	Coal	60.19	156.89	452	256	0.86	Ainim
	Coal	65.84	161.03	450	239	0.89	Ainim
	Coal	65.53	145.6	456	218	0.87	Ainim
	Claystone	1.06	0.91	459	75	0.87	Ainim
	Claystone	1.03	0.48	461	38	0.87	Ainim
Outcrop Samples	Shale	0.05	0.07	0	-	-	Ainim
	Shale	0.4	0.15	37	-	-	Ainim
	Shale	1.18	0.58	48	446	-	Ainim
	Shale	1.21	0.39	31	441	0.59	Ainim
	Coal	34.04	132.28	382	440	0.56	Ainim
	Shale	0.83	0.36	42	443		Ainim
	Coal	23.33	101.71	431	437	0.57	Ainim
	Shale	3.76	1.89	48	443	-	Ainim
	Shale	1.5	1.06	66	447	-	Ainim
	Shale	0.14	0.15	78	459	-	Ainim
	Shale	2.82	4.12	123	455	0.6	Aifat
	Shale	0.55	0.23	38	487	1.5	Aifat
	Shale	0.56	0.17	25	476	-	Aifat
	Claystone	0.5	0.08	14	-	-	Ainim
	Coal	55.21	208.08	369	438	0.65	Ainim
	Shale	0.65	0.37	52	449	-	Ainim
	Shale	3.19	3.67	110	448	-	Ainim
	Shale	0.82	0.16	13	-	-	Ainim
	Coal	49.34	155.46	306	441	0.6	Ainim
	Coal	43.02	187.21	422	440	0.71	Ainim
	Shale	0.68	0.22	29	470	0.73	Ainim
	Claystone	0.1	0.03	16	-	-	Ainim
	Coal	54.73	167.87	298	442	-	Ainim
	Coal	7.15	15.54	212	447	-	Ainim
	Claystone	0.07	0.01	-	-	-	Ainim
	Shale	1.66	2.84	159	448	-	Ainim
	Shale	6.43	19.78	288	447	-	Ainim
	Coal	48.73	178.03	352	450	0.73	Ainim
	Coal	22.39	57.5	234	448	0.71	Ainim
	Shale	1.45	2.11	137	449	-	Ainim
	Coal	35.46	107.07	282	449	-	Ainim

Samples	Lithology	TOC (wt.%)	Potential Yield (S_1+S_2)	T_{max}. (°C)	Hydrogen Index (HI)	Vitrinite Reflectance (%Ro)	Formation
	Coal	25.98	69.74	259	449	-	Ainim
	Shale	0.8	0.69	70	447	0.78	Aifat
	Shale	0.47	0.06	12	-	-	Aifat
	Shale	0.53	0.22	33	475	-	Aifat
	Shale	0.69	0.25	30	462	0.93	Aifat

Potential yield (S_1+S_2) provides an estimate of the hydrocarbon generation capacity. The coal samples demonstrate high potential yields with values reaching up to 208.08 mg HC/g rock indicates a strong capability for hydrocarbon generation. Shale and claystone samples exhibit significantly lower potential yields suggesting their role as secondary or poor hydrocarbon sources.

The Ainim Formation generally exhibits better source rock characteristics compared to the Aifat Formation. Many Ainim samples, particularly the cutting samples, fall within the good to excellent categories indicating high TOC values and significant hydrocarbon-generating potential. In contrast, the Aifat Formation samples are mostly classified as poor to moderate source rocks (Figure 3). Their lower TOC values and potential yield suggest that these rocks contain less organic matter and have a reduced capacity for hydrocarbon generation. This may be due to differences in depositional environments, organic matter type or post-depositional alteration processes such as oxidation or thermal degradation.

The positive correlation between TOC and potential yield observed in the graph is consistent with general geochemical principles. Sediment with higher TOC typically generate more hydrocarbons if they contain thermally mature kerogen. The Ainim Formation, especially its cutting samples, exhibits this trend clearly suggesting that these samples may have been buried deeper and preserved under better conditions compared to the outcrop samples, which are more exposed to weathering and oxidation.

The excellent category which represents the highest-quality source rocks is dominated by Ainim Formation samples. These samples exhibit TOC values exceeding 10% and potential yields well above 10 mg HC/g rock suggesting that they are highly enriched in organic matter. Such high values are typically associated with anoxic depositional environments where organic material is well-preserved due to limited oxygen exposure.

On the other hand, the non-source rocks category includes samples with very low TOC (< 0.5%) and minimal potential yield indicating that these rocks lack sufficient organic content for petroleum generation. Many of the Aifat Formation samples along with some Ainim outcrop samples fall into this category. This suggests that either these rocks were deposited in oxygen-rich environments that prevented organic matter preservation or that they have undergone extensive degradation over time.

The variation in source rock quality between the Ainim and Aifat Formations can be attributed to several geological factors including differences in depositional settings, sedimentation rates, and organic matter input. The Ainim Formation likely represents a more favorable environment for organic matter accumulation and preservation, whereas the Aifat Formation may have experienced higher energy conditions that limited organic matter retention.

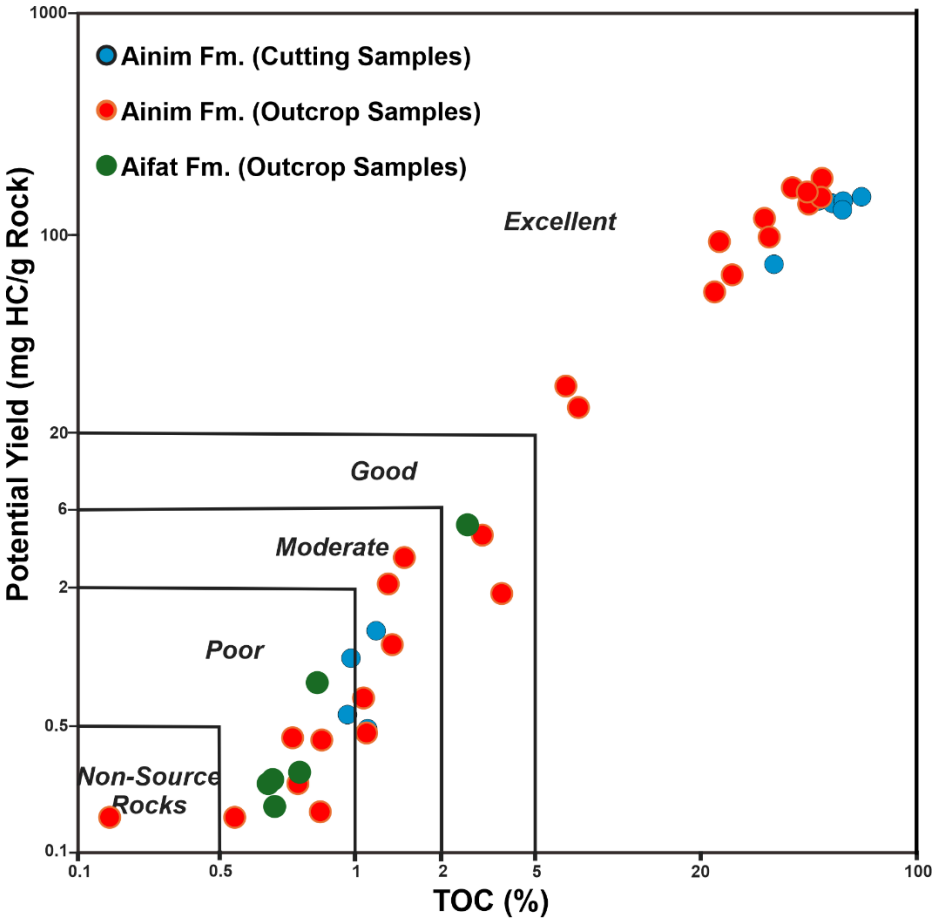

Figure 3. The positive correlation between TOC and potential yield suggests that organic richness significantly influences source rock potential.

Organic matter quality (kerogen type)

Hydrogen Index (HI) values further distinguish the type of organic matter present. Coal samples generally have higher HI values ranging from 85 to 438 mg HC/g TOC, which is indicative of type II and type III kerogens, favoring gas-prone and some oil-prone characteristics. Shale samples exhibit HI values that vary significantly, with lower values suggesting the presence of type III kerogen, which is primarily gas-prone. Hydrogen Index (HI) versus T_{max} plot commonly used in petroleum geochemistry to classify kerogen types and assess the thermal maturity of source rocks (Figure 4). Most of the samples from both the Ainim and Aifat Formations fall within the type III and type II kerogen with HI values ranging predominantly between 50 and 400 mg HC/g TOC. This suggests that most of the organic matter in these formations is gas-prone or mixed oil-and-gas prone. The scarcity of type I kerogen indicates that highly oil-prone source rocks are not dominant in the study area. Additionally, the T_{max} values of most samples range between 435°C and 470°C placing them within the mature oil window with some extending into the postmature zone.

The presence of type III kerogen in the Aifat Formation suggests that the organic matter is primarily of terrestrial origin likely derived from plant material and deposited in deltaic or fluvial environments. This interpretation is supported by the observed lower HI values observed in the Aifat Formation samples which are generally below 200 mg HC/g TOC. These findings indicate that the Aifat Formation is more gas-prone, with limited oil generation potential.

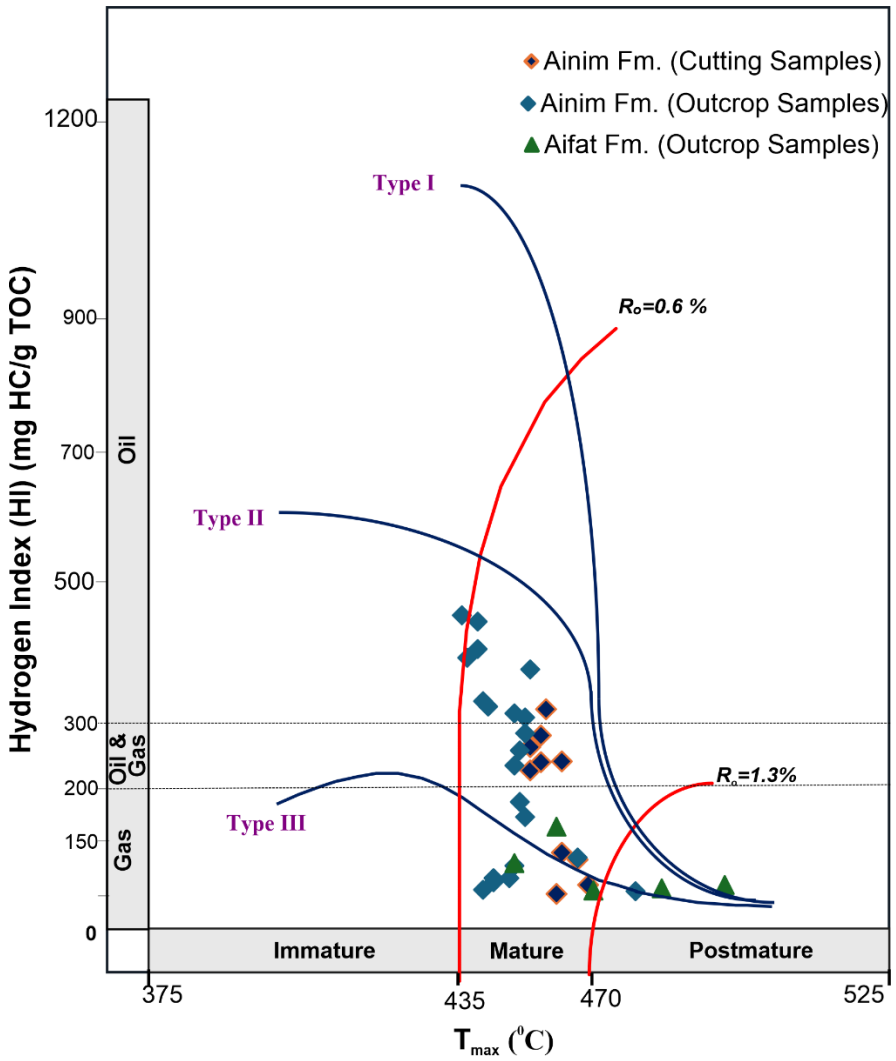

Figure 4. Hydrogen Index (HI) vs. Tmax plot for source rock evaluation of the Ainim and Aifat Formations in the "Idea" Field, Bintuni Basin, West Papua. The diagram classifies kerogen types into type I (oil-prone), type II (oil and gas-prone), and type III (gas-prone).

The Ainim Formation samples, especially the cutting samples exhibit a wider range of HI values with some falling into the type II kerogen category. This suggests that the Ainim Formation contains more hydrogen-rich organic matter potentially sourced from marine or lacustrine environments. The higher HI values in some Ainim samples indicate better oil-generation potential compared to the Aifat Formation. However, the fact that many Ainim samples still fall within the type III range suggests that a significant portion of the organic matter is gas-prone.

The Ainim Formation appears to be the more promising source rock, particularly where type II kerogen is present and thermal maturity is within the oil window. The Aifat Formation, with its dominance of type III kerogen is more likely to be a gas-prone source rock thus rendering it less favorable for liquid hydrocarbon exploration, while indicating potential for gas development. The Ainim Formation exhibits stronger oil potential due to the presence of type II kerogen and suitable thermal maturity, while the dominance of type III kerogen in the Aifat Formation underscores its primary prospect as a gas-prone source.

Thermal maturation of organic matter

The vitrinite reflectance (%Ro) versus T_{max} plot is an essential geochemical tool for

assessing the thermal maturity of source rocks (Figure 5). T_{max} is the temperature at which the maximum hydrocarbon generation occurs during pyrolysis. Typically, T_{max} values below 435°C indicate immature source rocks, while values between 435°C and 450°C correspond to the early oil window. T_{max} values in the range of 450°C to 470°C indicate peak maturity, and values above 470°C suggest postmaturity.

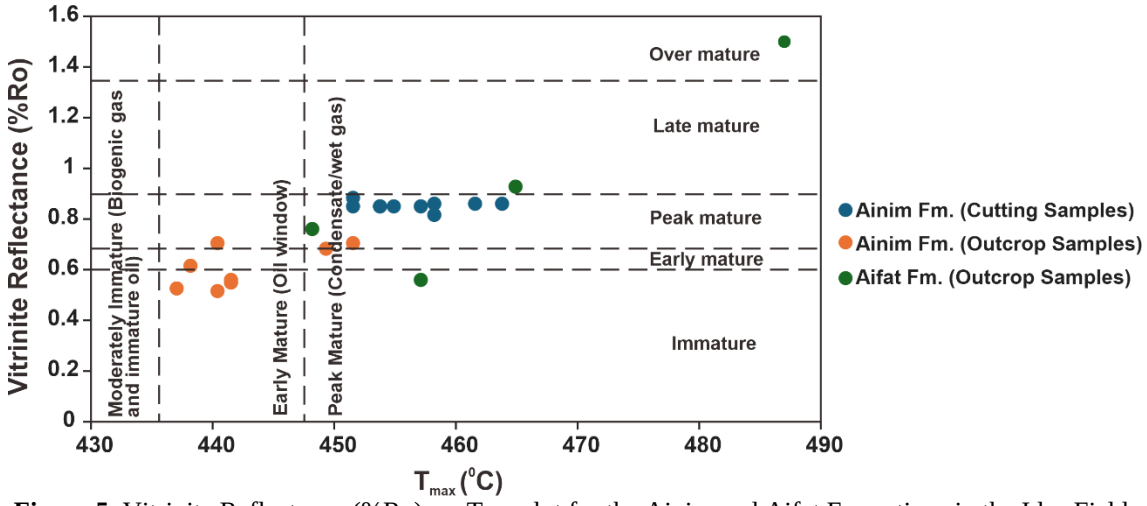

Figure 5. Vitrinite Reflectance (%Ro) vs. T_{max} plot for the Ainim and Aifat Formations in the Idea Field, Bintuni Basin, West Papua.

The coal samples present Ro% values between 0.56% and 0.87%, suggesting a maturity range from early to peak oil generation. Some shale samples show higher Ro% values reaching up to 1.5%, indicating potential dry gas generation. The claystone samples do not provide consistent Ro% data, which suggests they may not be significant contributors to hydrocarbon generation.

The Ainim Formation outcrop samples generally fall within the moderately immature to early mature stages with %Ro values ranging from approximately 0.5% to 0.7% indicates that these samples are at or near the onset of the oil window suggesting limited hydrocarbon generation potential in their current state. However, with continued burial and thermal exposure they could evolve into more effective source rocks.

The Ainim Formation cutting samples exhibit higher thermal maturity predominantly within the peak mature stage with %Ro values clustering between 0.7% and 1.0%. These samples suggest that deeper sections of the Ainim Formation have reached optimal conditions for oil and condensate generation. Their T_{max} values ranging between 450°C and 465°C further confirm that they are within the main oil window and approaching the wet gas generation zone.

The Aifat Formation outcrop samples show a wider range of thermal maturity with some samples falling within the peak mature stage while others extend into the late mature and over mature stages. One sample in particular exhibit a Ro value exceeding 1.3% indicating it has reached a highly mature state where oil generation has ceased, and secondary gas generation may be occurring. This suggests that certain sections of the Aifat Formation have undergone extensive thermal evolution, potentially making them more gas-prone.

The distribution of thermal maturity across the formations suggests that burial history and geothermal gradients have played a significant role in hydrocarbon generation

potential (Hazra et al., 2019). The Ainim Formation, especially in deeper subsurface areas as represented by cutting samples, has reached an optimal level of thermal maturity. the organic matter within the formation has been exposed to just the right combination of temperature and time to efficiently generate oil and gas, but not so much that the hydrocarbons are destroyed or converted entirely to gas (Syarifah et al., 2021; Li et el., 2022). In contrast, the Aifat Formation appears to have undergone a more complex burial and heating history. This complexity may be due to variations in sedimentation rates, episodes of uplift or erosion, or differences in geothermal gradients across the formation. As a result, some samples from the Aifat Formation show signs of overmaturity (Utomo et al., 2022; Syarifah et al., 2021).

Conclusion

The evaluation of source rocks in the Bintuni Basin shows that the Ainim Formation has stronger hydrocarbon potential compared to the Aifat Formation. The Ainim Formation contains claystone, shale, and coal with high TOC and a mix of type II and type III kerogen making it suitable for generating both oil and gas. Thermal maturity data from cutting samples show that it is mostly in the peak oil window, which is favorable for oil and condensate generation. However, outcrop samples are only in the early maturity stage and may need further burial to become productive. The Aifat Formation mainly consists of shale with lower TOC and is dominated by type III kerogen, indicating it is more suitable for gas generation. Its thermal maturity varies with some samples being overmature, which limits its potential for oil but supports gas generation. The Ainim Formation, especially in the subsurface areas like the "Idea" Field is the more promising target for oil and gas exploration due to its high organic content and mature thermal state.

Acknowledgements

We sincerely appreciate everyone who contributed to the successful completion of this study. I am especially grateful to the editors, reviewers, and proofreaders for their valuable insights and meticulous attention to detail. A special thanks goes to PT Petroenergy Wiriagar KSO Pertamina EP Wiriagar and Muhammad Thariq Almuqtadir from Pertamina EP Regional 4 for providing me with the opportunity to access the research data.

Author Contribution

Conceptualization, D.A and J.; methodology, D.A, W.U.; validation, J., W.U, A.M, and J.W; formal analysis, D.A and B.M.U; investigation, D.A. and J; data curation, D.A, W.U, A.M, and J.W; writing—original draft preparation, D.A and J.; writing—review and editing, W.U, A.M, B.M.U, N.M, A.S and J.W; visualization, D.A and J.; Supervision, W.U, A.M, and J.W. All authors have read and agreed to the published version of the manuscript

Conflict of Interest

The authors declare no conflict of interest.

References

Alam, S., & Setiadi, D. J. (2019). Tertiary Sequence Stratigraphy of Bird Head Area, Eastern Indonesia. *Indonesian Journal on Geoscience*, 6(3), 267–278. https://doi.org/10.17014/ijog.6.3.267-278

Edmundo. M. T., Utomo. W., & Almuqtadir. M. T. (2021). Analisis Petrofisika dan Perhitungan Volumetrik Hidrokarbon Pada Batugamping Formasi Kais Lapangan Wiriagar, Cekungan

Bintuni. *Proceeding Seminar Nasional Teknologi Energi dan Mineral*, 1, 1 – 15.

Hamzah, A., Saragih, R. Y., Gibran, A. K., Prawiranegara, D. A. R., & Irawan, D. (2018). Depositional History and Organic Geochemistry of the Klasafet Formation: Implications to Potential Source Rock in Bintuni Basin, West Papua. *Proceedings of the Indonesian Petroleum Association*, 42nd Annual Convention.

Handyarso, A., & Padmawidjaja, T. (2017). Struktur geologi bawah permukaan Cekungan Bintuni berdasarkan data gaya berat. *Jurnal Geologi dan Sumberdaya Mineral*, 18(2), 75–84. https://jgsm.geologi.esdm.go.id/index.php/JGSM/article/view/125

Harahap, B. H. (2012). Tectonostratigraphy of the Southern Part of Papua and Arafura Sea, Eastern Indonesia. *Indonesian Journal on Geoscience*, 7(3), 167–187. https://doi.org/10.17014/ijog.7.3.167-187

Haris, A., Siburian, I. B., & Riyanto, A. (2017). Facies modeling of Kais Formation Limestone: A case study of Kafor Field, West Papua, Indonesia. *International Journal of GEOMATE*, 13(40), 160–166. https://geomatejournal.com/geomate/article/view/1387

Hazra, B., Singh, A. K., Singh, P. K., Mani, D., Boral, P., & Das, M. (2019). Hydrocarbon-generation potential and thermal-maturity of few Indian coals: inferences from organo-petrography and Rock-Eval. *Energy Sources, Part A: Recovery, Utilization, and Environmental Effects*, 46(1), 4288–4297. https://doi.org/10.1080/15567036.2019.1695981.

Indriyani, P. D., Harja, A., & Nainggolan, T. B. (2020). Petrophysical analysis to determine reservoir and source rocks in Berau Basin, West Papua waters. *Bulletin of the Marine Geology*, 35(1), 1–12. https://doi.org/10.32693/bomg.35.1.2020.659

Jamaluddin, J., & Sea, J. G. (2018). Evaluasi Batuan Induk Berdasarkan Data Geokimia Hidrokarbon pada Sumur Prabumulih, Cekungan Sumatra Selatan. *Jurnal Geomine*, 6(3), 109–115. https://doi.org/10.33536/jg.v6i3.241

Jamaluddin, J., Nugraha, S. T., Maria, M., & Umar, E. P. (2018). Prediksi Total Organic Carbon (TOC) Menggunakan Regresi Multilinear dengan Pendekatan Data Well Log, *Jurnal Geocelebes*, 2(1), 1–5. https://doi.org/10.20956/geocelebes.v2i1.3568

Jamaluddin, J., Pratikno, F. A., Taslim, A. I., & Kaunang, I. (2025). Karakteristik maseral dan peringkat batubara daerah Balikpapan Selatan berdasarkan analisis petrografi organik. *Geosains Kutai Basin*, 8(1), 10–15. https://jurnal.fmipa.unmul.ac.id/index.php/geofis/article/view/1448

Jamaluddin, J., Rahmawati, D., & Maria, M. (2024a). Analisis Lingkungan Pengendapan dan Karakteristik Material Organik Daerah Air Putih, Kota Samarinda, Indonesia. *Jurnal Geosains dan Teknologi*, 6(3), 203–214. https://doi.org/10.14710/jgt.6.3.2023.203-214

Jamaluddin, J., Wagreich, M., Gier, S., Schöpfer, K., Battu, D. P. (2023). Sedimentary Environments and Paleoclimate Control of the Middle Miocene Balikpapan Group, Lower Kutai Basin (Indonesia): Implications for Evaluation of the Hydrocarbon Potential. *Minerals*, 13(10), 1259. https://doi.org/10.3390/min13101259

Jamaluddin, J., Wagreich. M., Schöpfer, K., Sachsenhofer, R. F., Maria, M., & Rahmawati. D.. (2024b). Hydrocarbon potential and depositional environment of the Middle Miocene Balikpapan Formation, lower Kutai Basin, Indonesia: Sedimentology, calcareous nannofossil, organic geochemistry, and organic petrography integrated approach, *International Journal of Coal Geology*, 293, 104591. https://doi.org/10.1016/j.coal.2024.104591

Lelono, E. B., Firdaus, M., & Tri Bambang, S. R. (2023). Palaeoenvironments of the Permian-Cretaceous sediments of the Bintuni Bay, Papua. *Scientific Contributions Oil and Gas*, 33(1), 1–12. https://doi.org/10.29017/SCOG.33.1.810

Li, S., Zheng, L-J, Guo, X. (2022). Thermal Evolution and Hydrocarbon Generation Capacity of Typical Palaeozoic Marine Source Rocks in the South China Craton: Constrains from Semiclosed Artificial Thermal Maturation Experiments. *Lithosphere*, Special 13, 9072890. https://doi.org/10.2113/2022/9072890

Nopiyanti, T., Nainggolan, T. B., Dewanto, O., & Haq, D. A. (2020). Well log analysis and geochemical data to identify source rock and hydrocarbon reservoir: Northeast Java Basin study case. *AIP Conference Proceedings*, 2245(1), 070017. https://doi.org/10.1063/5.0006978

Sapiie, B., Naryanto, W., Adyagharini, A. C., & Pamumpuni, A. (2012). Geology and Tectonic Evolution of Birds Head Region Papua, Indonesia: Implication for Hydrocarbon Exploration in Eastern Indonesia, *Search & Discovery Article*, 30260. https://www.searchanddiscovery.com/pdfz/documents/2012/30260sapiie/ndx_sapiie.pdf.html

Syarifah, I., Almutaqdir, M. T., Maryanto, S., & Utomo, W. (2021). Basin modeling based on geochemical analysis: Case study "Y" Field, Bintuni Basin, West Papua. *HAGI Proceedings*.

Ustiawan, A. B., Nainggolan, T. B., & Setyawan, R. (2019). Interpretasi Struktur Geologi Di Perairan Aru Selatan, Maluku Berdasarkan Data Seismik 2D Multi Channel. *Jurnal Geosains dan Teknologi*, 2(2), 53–60. https://doi.org/10.14710/jgt.2.2.2019.53-60

Utomo, W., Paparezzi, R. D., & Almutaqdir, M. T. (2022). Prediksi Tekanan Pori Pada Lapangan Wiriagar Cekungan Bintuni. *Lembaran Publikasi Minyak dan Gas Bumi*, 56(3), 159–171. https://doi.org/10.29017/LPMGB.56.3.1204

Winardi, S., Toha, B., Imron, M., & Amijaya, D. H. (2013). The Potential of Eocene Shale of Nanggulan Formation as a Hydrocarbon Source Rock. *Indonesian Journal on Geoscience*, 8(1), 13–23. https://doi.org/10.17014/ijog.8.1.13-23

Indexing and Abstracting

GEOFISIKA
UNIVERSITAS HASANUDDIN

ISSN 2579-5546